CHAPTER 1

INTRODUCTION

1.1 Overview

Temperature and water vapor are basic meteorological parameters for weather forecasting. They are also critical variables for the tropospheric chemistry researches. Since the first satellite SPUTNIK was launched in 1957, the determination of atmospheric parameters from space-based observations has been a topic of great interest to the meteorological community[Houghton (1961); Kaplan (1959); King (1956)]. Regardless the sophistication of the model or the power of the computer, a correct specification of the atmospheric state obtained by satellite observation is a necessary for initializing numerical models for accurate weather predictions. Oceans, which provide a gap of conventional balloon observation, is major part of our planet. The satellite global coverage fills those gaps, and provides a denser sounding coverage than balloon sondes for land observations. It was highly expected that the satellite sensing of the atmospheric state would appear to improve the accuracy of both short-term mesoscale forecasts for coastal regions and extended forecasts of global synoptic-scale weather.

Two pioneering sounding spectrometer sensors SIRS-A, which measured outgoing radiance in seven 5 cm^{-1} intervals of the 15 μm CO_2 band and one 5 cm^{-1} channel in the 11 μm "window" region and IRIS, which measured radiance with 5 cm^{-1} resolution within the 5-25 μm.) were launched on the Nimbus 3 satellite in April 1969 [Wark and Hilleary (1969); Wick (1971)]. Since those initial experiments, temperature and water vapor soundings have been now available from numerous earth

satellites for more than 40 years. Because of the relatively large number of satellite sounders in orbit at any time, with each satellite providing twice daily atmospheric profiles on a global scale, the satellite soundings have benefited the numerical weather prediction operation significantly. Given expanded computer resources and improved data assimilation methods, satellite data model initialization has improved the forecast accuracy dramatically[Koehler et al. (1983)]. The satellite radiance measurement during 60's and 70's were mainly in multi-spectral imaging and sounding capabilities, where the multi-spectral radiometers observe the radiance within a small number of spectral channels (e.g., 2-50) with a spectral resolution power ($\nu/\delta\nu$) of about 100. These previous broadband sensors, such as Advanced TIROS Operational Vertical Sounder (ATOVS) on NOAA's Polar Operational Environmental Satellite can only provide sounding with relatively low vertical resolution. This vertical resolution has limited utility of the satellite observations for weather forecasting, particularly for mesoscale severe weather predictions. The low vertical resolution satellite sounding would cause a huge temperature discrepancy ($\sim$ 10 °C) with conventional radiosonde data near the inversion levels such as the tropopause or at the top of the boundary layer[Broderick et al. (1981)]. In many circumstances, the low vertical resolution would reduce the horizontal variance and produce strong horizontal error correlation of the satellite soundings [Philips (1980)]. Another disadvantage of the multi-spectra radiometer observation is it's limited capability to monitor the atmospheric minor constituents consistently, which is main focus of the climate change community.

In order to overcome these limitation, it was necessary to develop new sensors and algorithms with improved vertical resolution and with an ability to handle partially cloudy scenes. Since mid-1970s, extensive retrieval algorithms, instrument design, and experimental field studies have been conducted to determine the feasibility and requirements of a future advanced sounder [Smith (1990)]. Thus, the satellite radiance measurement capability has evolved to hyper-spectral or ultra-spectral imaging which

provides a large number of spectral radiance channels (100-10000) with resolving power ranging within 1000-10000, respectively.

The ultra-spectral infrared radiances are generally measured by a Fourier Transform Spectrometer (FTS) mounted on an aircraft, a satellite, a vessel or ground station. The techniques for the inversion of the radiative transfer equation, can be used to infer the parameters of atmospheric state such as temperature, water vapor, and other chemical spices at relative high vertical resolution [Wark and Fleming (1966); Smith et al. (1979); McMillan et al. (1997)]. In mid-1980's, the flight of NASA ER-2 High-resolution Interferometer Sounders (HIS) [Smith et al. (1979, 1986); Revercomb et al. (1988)]successfully demonstrated this high vertical resolution sounding technique.

As the consequence of these pioneering works, progressively higher spectral and spatial resolution remote sensors are now being launched. These modern sensors, including experimental Tropospheric Emission Spectrometer (TES)[Beer et al. (2001); Beer (2006)] on the Aura spacecraft, the Atmospheric Infrared Sounder (AIRS)[Aumann et al. (2003)] on the Aqua satellite, and operational Infrared Atmospheric Sounding Interferometer (IASI)[Hébert et al. (2004)] on the Metop satellite, the Cross-Track Infrared Sounder (CrIS)[*Liu et al.*,2003] on the NPOESS Preparatory Project (NPP), and Geosynchronous Imaging Fourier Transform Spectrometer (GIFTS) which is designed to fly on geostationary satellites[Smith et al. (2001)], have thousands of spectral channels and provide a wealth of information on atmospheric and surface properties. Together the Metop and Suomi-NPP/JPSS will better satisfy the demands for global high vertical resolution sounding data as needed for improved extended range numerical weather prediction.

The success of using HIS on the ground looking upwards also motivated the idea of using ultra-spectral interferometer to monitor the downwelling infrared radiance continuously[Smith et al. (1990)]. The accuracy and very high vertical resolution

of profiling from these spectral measurement provide a great opportunity to study the properties of atmospheric boundary layer. Since the first dedicated ground-based infrared emission instrument was built in 1989, AERI systems have been installed in seven ARM boundary facilities during 1998-2003. Several variants of AERI, including M-AERI, P-AERI, and ASSIST, have been deployed for marine, polar and other observations, respectively.

1.2 Research Focus

The basic concept of atmospheric sounding using infrared radiance measured by spectrometer is: the brightness temperatures measured in the spectrum lines of CO_2 absorption bands is strongly correlated to the vertical profile of the atmospheric temperature. Indeed, the radiant energy measured by spectrometer is the sum of thermal emissions from the different absorbing layers of the atmosphere. By selecting wavelengths so that emittance (absorption) peaks in a given layer and decrease dramatically in the other layers, and assuming that emittance is known at this level (this is possible for uniformly mixed gases such as CO_2), we can de-convolute a set of measurements providing overlapping layer temperature measurements (i.e., one layer for each wavelength). Thus, the de-convolution of a complete set partially overlapping layer of measurements provides the temperature profile. Similarly, if the temperature profile is known, measurements from water vapor (or ozone) absorption bands allow us to derive the humidity profile (or ozone vertical distribution). As an example of previous broadband sensors, the NOAA/HIRS operational sounder which offers a spectral resolution of about 15 cm^{-1} currently provides an accuracy of approximately 2.5 Kelvin for temperature and 40% for humidity. The vertical resolution and accuracy of the profiles derived by the de-convolution numerical process is highly dependent on the signal to noise ratio and spectral resolution of the radiance measurements.

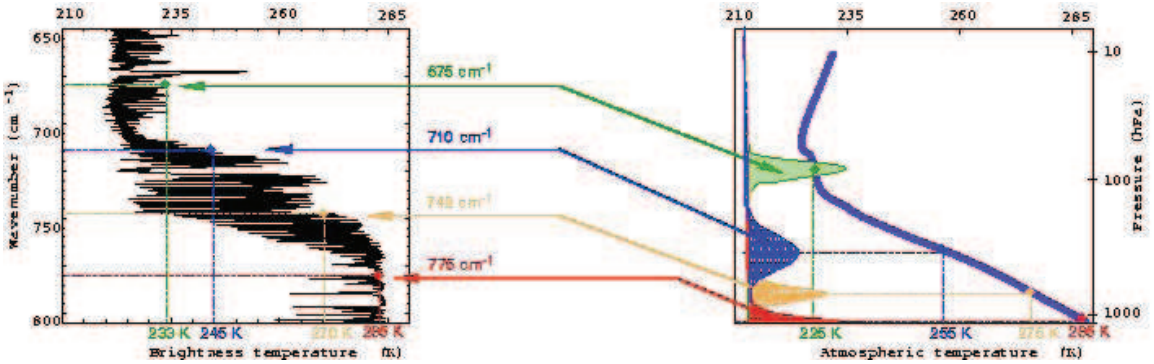

Figure 1.1 Correlation between CO_2 absorption spectrum and atmospheric temperature profile.

The ultra-spectral resolution concept involves measuring a large portion of the infrared spectrum of Atmospheric radiance emitted to space or to the ground in order to obtain a very large number of noise independent spectral channels of radiance for inferring atmospheric profiles of temperature, water vapor and other traces gases. Contrary to the tens of measurements of previous multi-spectral radiance data, the ultra-spectral radiance data provides thousands of spectral channels enabling an order of magnitude improvement in signal to noise. Thus, a much more precise inversion of the integral radiative transfer equation,(i.e., de-convolution of the overlapping layer temperature observation). Figure (1.2) shows the comparison of the weighting functions (i.e., vertical resolving power of individual spectral radiances) and the averaging kernels of retrieved temperature profiles (i.e., the vertical resolution functions) for both low spectral (15 cm^{-1}) and ultra spectral (0.5 cm^{-1}) resolution radiance observations. Although the vertical resolution of individual spectral channels is enhanced by just 25%, or less, the vertical sounding resolution is enhanced by a factor of two to three (i.e., 200 - 300%). Assuming the individual spectral channel noise levels is comparable to the multi-spectral resolution system, that huge increase of vertical sounding resolution results for the greatly increased system ratio of signal to noise of the ultra-spectral resolution measurement system.

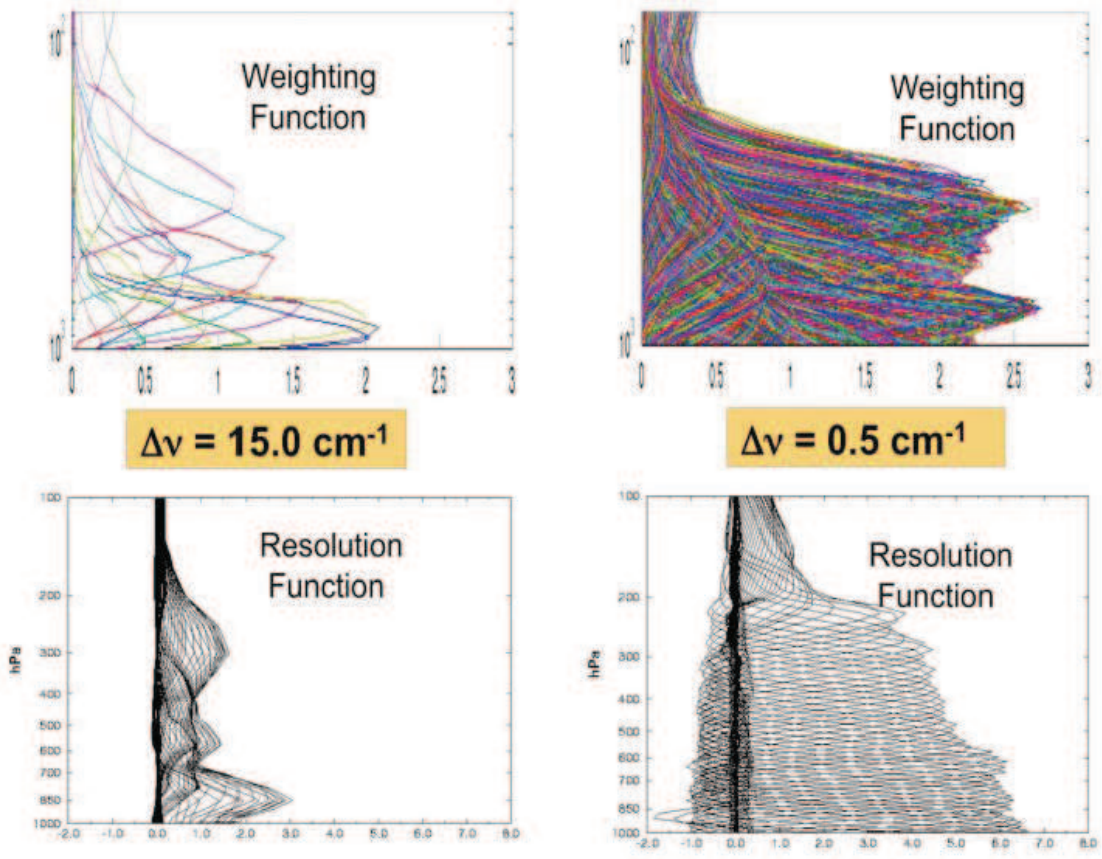

Figure 1.2 The temperature weighting functions and vertical profile resolution functions (i.e., averaging kernals) for two different instrument spectral resolutions.

Although the satellite-borne ultra spectrometer provides the global coverage of temperature, water vapor and other gases soundings with a relatively high vertical resolution ($\sim$ 2 km) for the troposphere, this vertical resolution is still too low for resolving the planetary boundary layer. Also, even within the window region, the spectral information from the low level atmosphere is mixed with contribution from higher levels of the atmosphere. Thus, the retrieval errors for the atmosphere near the ground level are exaggerated. On the other hand, the signal radiance observed by an uplooking ground based spectrometer is dominated by contributions from the boundary layer of the atmosphere. Thus, ground based spectrometers are mainly sensitive to the lowest 3 km of atmosphere.

Figure(1.3) shows the simultaneous satellite (IASI) and ground-based (ASSIST) radiance spectra. The characteristics of these two spectra reveal different sensitivities to the same atmospheric state. For the 620 - 720 cm^{-1} CO_2 emission region, the IASI spectrum varies as a result of abundant absorption lines and mainly reflects the upper and middle tropospheric temperature profiles. The ASSIST spectrum on the other hand reflects the temperature at the planetary boundary layer. For the window region of 800 - 1000 cm^{-1}, the IASI spectrum can be related the surface temperature or cloud temperature, while the ASSIST spectrum has absorption lines due to the water vapor against a cold space background.

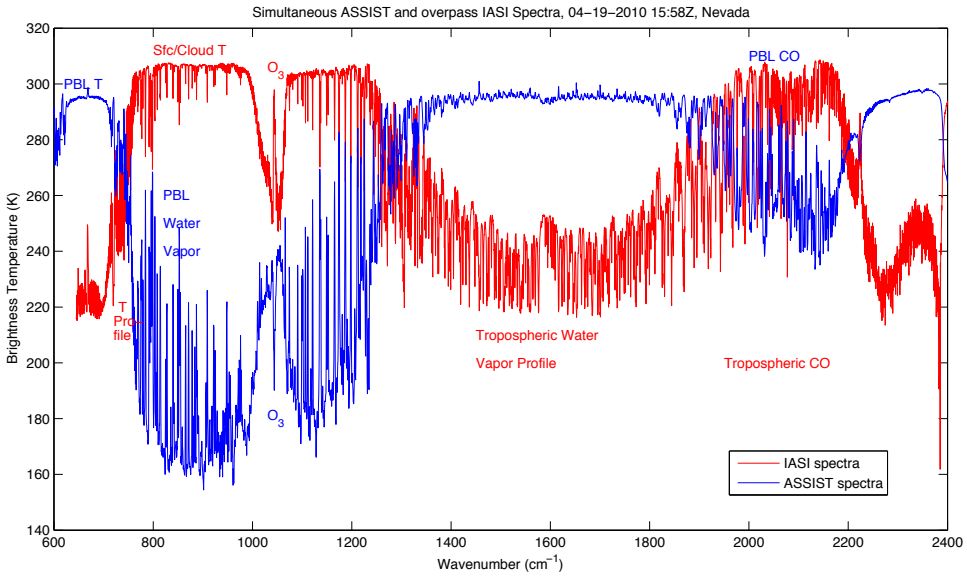

Figure 1.3 Simultaneous satellite (IASI) and ground-based (ASSIST) ultra spectra

Figure(1.4) shows the simulated weighting function (i.e., Jacobian) profiles of temperature ($\partial R/\partial T$) and water vapor ($\partial R/\partial Q$) for up/downwelling radiance at high spectral resolution. The Jacobian represents the contribution of the atmosphere on a certain layer to the radiance sensed by spectrometer's detector. The upper panels indicate that the vertical distribution of maximum of Jacobian for upwelling are relative homogeneous, while the lower panels indicate that value of most Jacobians decrease exponentially as the altitude increases, and the height maximum of Jaco-

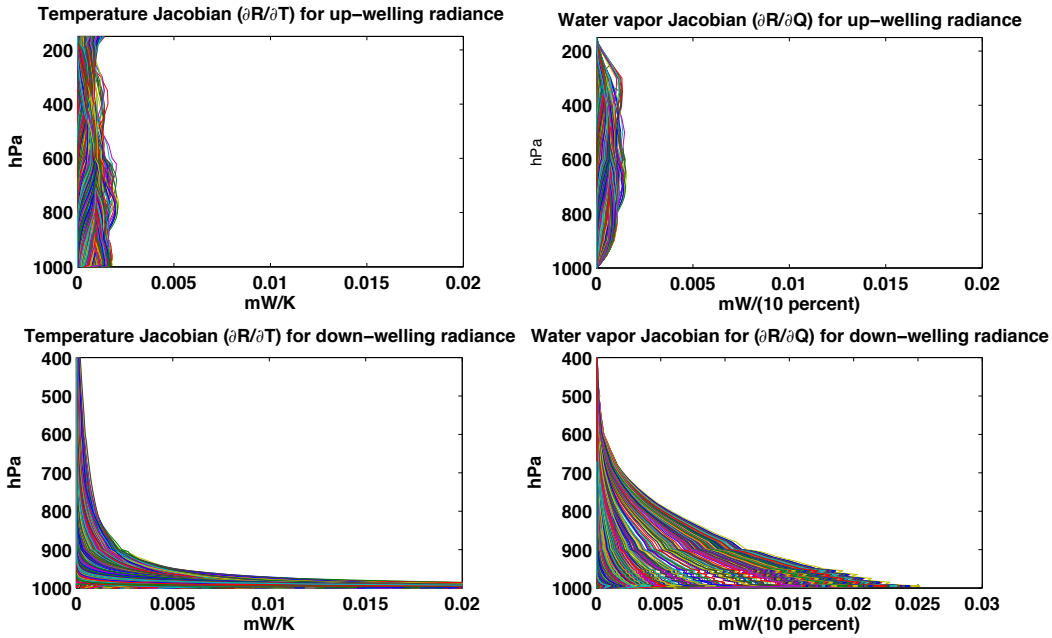

Figure 1.4 Temperature and water vapor jacobian for standard atmosphere

bian are generally lower than 900 hPa. Also, below 900 hPa the magnitudes of the maximum of jacobian for downwelling radiance are larger than that for upwelling radiance one, and two orders for temperature and water vapor, respectively. These two features prove that the sounding from downwelling radiance provides higher vertical resolution and higher accuracy for the low level atmosphere than does the sounding from upwelling radiance. It is noticeable that near the ground for me care where the surface skin temperature is equal to the surface air temperature, most water vapor Jacobians for upwelling radiance decrease dramatically as the altitude decreases. For this case, there is no maximum of Jacobian for layer below 900 hPa. This implies that the low level water vapor retrieval from upwelling radiance are less reliable than the temperature retrieval.

Considering the advantages and disadvantages of sounding from ground based and satellite-borne ultraspectal sensors, it is proposed to use both the the ultra-spectral radiance measured from satellite-borne and ground-base instruments to retrieve the

temperature and water vapor with very high resolution and high accuracy throughout planetary boundary layer as well as the free atmosphere. If the combined retrieval provides a significant improvement, it is possible apply this combined retrieval result to improve the retrieval from satellite-borne ultra-spectral radiance measurements at the ground-based a climate observation ground station (i.e.,the DOE ARM CART sites).

1.3 Outline of Research

This thesis is organized as follows: in chapter 2 the ultra-spectral instruments including ground based and satellite-borne interferometers used in this research are described. The main principles of radiative transfer models and inversion algorithms are discussed in chapter 3. In chapter 4, the details of combined retrieval procedure and the four observation data-sets in this research are described. The retrieval result for each observation case is presented in Chapter 5. The conclusion of this research is presented in Chapter 6.

CHAPTER 2

HIGH-RESOLUTION SPECTROMETER SOUNDER

The infrared window region between 800 and 1000 cm^{-1} is mostly transparent to infrared radiation, except for several weak water vapor lines. Broad band radiometers (HIRS, MODIS, GOES, MSG) do not resolve these absorbtion lines, however, the hyper spectrometer (HIS, AIRS, IASI, CrIS) can detect these lines and most important the radiance contribution from in between them. The radiance observed in the far wing of an absorption line has much higher vertical resolving power than the radiation observed near absorption line centers as a result of pressure broading. Thus, it is possible to retrieval water vapor profiles at high vertical resolution for low level atmosphere with those hyperspectral radiance, even some boundary layer features such as low level inversions. The concept of obtaining high vertical resolution atmospheric profiles from a high-frequency resonance portion of an interferogram, which is the basic measurement of a Michelson-type interferometer, was suggested in the late 70's [Kyle (1977); Alyea and Goldstein (1978); Smith et al. (1979)]

2.1 Michelson interferometer

The classical method of an infrared spectrometer is using a monochromator to scan through the radiation spectrum, thus a narrow band of wavelengths of radiation can be chosen for detection from a wider range of wavelengths available at the source. The disadvantage of this method is obvious: An ideal monochrmator is very hard to fabricate; It takes a long time for monochromator to scan the whole spectrum. Another measurement technique for collecting IR spectra is the Fourier Transform Infrared (FTIR) spectrometer. Instead of recording the amount of energy absorbed when the frequency of the IR radiation is varied by a monochromator, the IR radiation

is guided through an interferometer. The purpose of the interferometer is to have a beam of IR radiation, split it into two beams, and make one of the beams travel a different (optical) distance than the other in order to create alternating interference fringes.

A diagram of a Michelson interferometer is shown in figure (2.1). The Michelson interferometer consists of four arms. The first arm contains a source of IR radiation, the second arm contains a stationary mirror, the third arm contains a moving mirror, and the fourth arm is open. At the intersection of the four arms a beamsplitter is placed, which is designed to transmit half the radiation that impinges upon it, and reflect the other half. As a result, the light reflected by the beamsplitter strikes the fixed mirror, and the light transmitted by the beamsplitter strikes the moving mirror. After reflecting off their respective mirrors, the two light beams recombine at the beamsplitter, and then leave the interferometer to strike a detector.

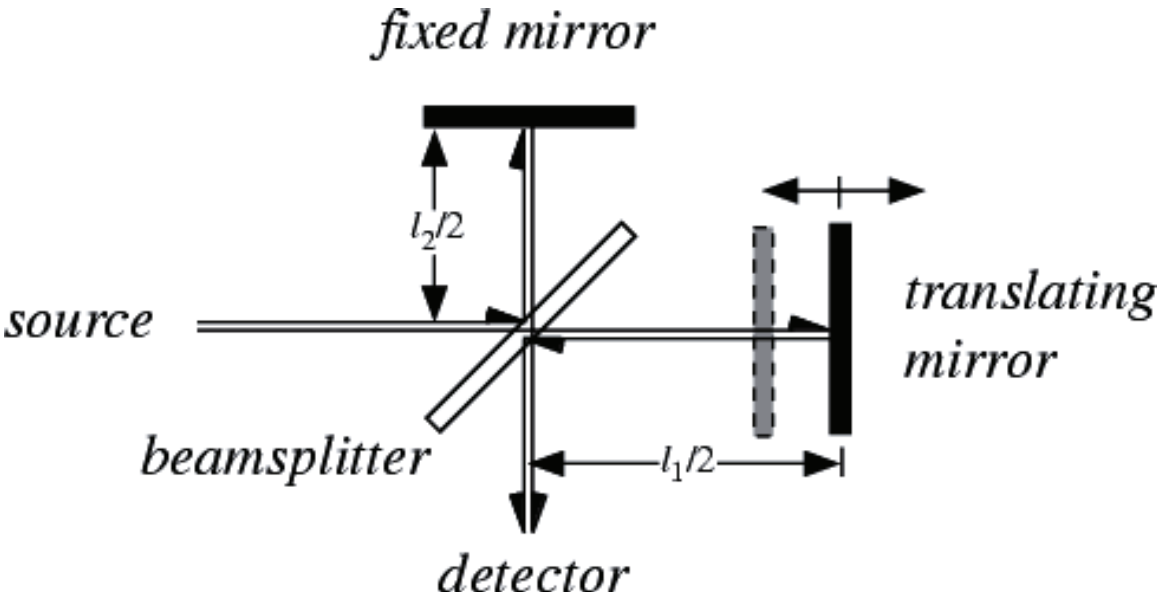

Figure 2.1 Schematic of a Michelson interferometer

In a Michelson interferometer an optical path difference is introduced between the two beams by translating the moving mirror away from the beamsplitter. A general property of optical waves is that their amplitudes are additive. When the beams

that have reflected off the fixed and moving mirrors recombine at the beamsplitter are in phase, an intense beam leaves the interferometer as a result of constructive interference. When the fixed and moving mirrors beams are recombined at the beamsplitter and the waves are completely out of phase, a low intensity beam leaves the interferometer as a result of destructive interference. A plot of light intensity versus optical path difference is called an interferogram. In fact, the interferogram is a measurement of the temporal coherence of the light at each different time/delay setting. Using the Fourier transformation, a signal in the time/delay domain is convolved to the frequency domain (i.e., the spectrum). The fundamental measurement obtained by an FTIR is made in the time/delay domain, which is Fourier transformed to give a spectrum (see figure (2.2)). This is where the term Fourier Transform IR spectroscopy comes from.

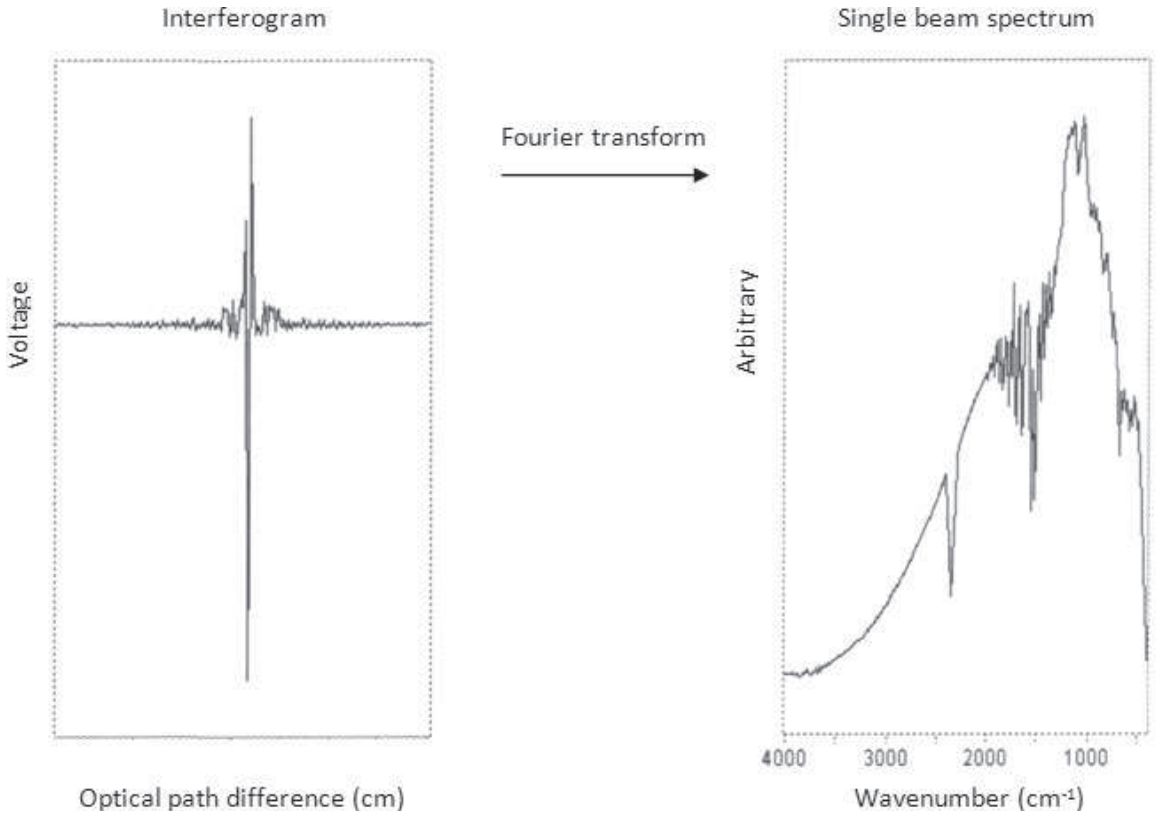

Figure 2.2 An Interferogram is Fourier transformed to give a spectrum

2.2 Satellite-borne hyper-spectral sounder

Following the success of the airborne interferometer HIS, Japan built and launched the Interferometric monitor for Greenhouse gases (IMG)[Shimoda and Ogawa (1997)] during 1997, which led to the first space demonstration of the ultra-spectral sounding capabilities. As part of Earth Observation System (EOS), an experimental ultra-spectral sounder, the Atmospheric Infrared Sounder (AIRS) [Aumann et al. (2003); Chahine et al. (2006)] onboard of the Aqua platform was launched into orbit on 4 May 2002. Based on a large focal plane detected the grating spectrometer design, the AIRS provides radiance within 2378 spectral channels, over 3 wavelength ranges: LWIR (9.14 - 15.38um); MWIR (5.71 - 8.26um); and SWIR (3.92 - 4.64 um). AIRS looks toward the ground through a cross-track rotating scan mirror which provides +/- 49.5 degrees (from nadir) ground coverage with 13.5-km spatial resolution at nadir from the 705.3 km orbit.

Also motivated by the success of HIS, Europe developed an advanced sounder for both atmospheric chemistry and meteorological applications for its operational polar orbiting Metop satellite. Because the interferometer design can provide wider spectral coverage and higher spectral resolution ($\sim$ 2-10 times higher depending upon wavenumber) and more precise apertural calibration and fidelity than the AIRS grating instrument, it was chosen for the Infrared Atmospheric Sounding Interferometer (IASI) instrument. The IASI was successfully launched into polar orbit aboard the Metop-A satellite on 19 October 2006. As one of main payloads of NPOESS Preparatory Program (NPP) satellite, which was launched successfully on 28 October 2011, the Cross-track Scanning Infrared Sounder (CrIS) also chose a Michelson interferometer, based on the design of the University of Wisconsin's Interferometer Thermal Sounder (ITS). Thanks the developing of new techniques, the CrIS achieves a spectral resolution, spectral coverage, and number of spectral channels similar to AIRS but much lower cost and in a much smaller volume and lower radiance noise than

the AIRS grating spectrometer. This evolution of the satellite based ultra-spectral sounders are shown in the figure(2.3). The characteristics of these ultra-spectral sounders are provided by table(2.1).

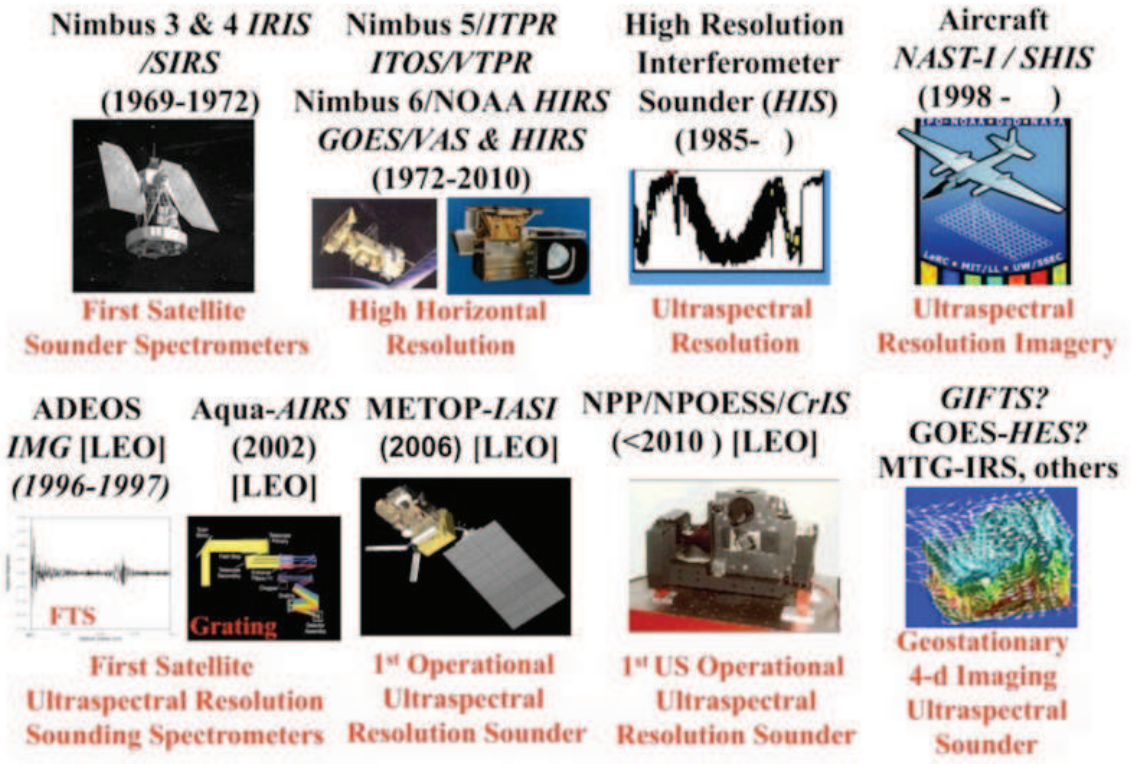

Figure 2.3 Evolution of the satellite-borne ultra-spectral resolution sounders

2.2.1 IASI instrument description

The Infrared Atmospheric Sounding Interferometer (IASI) [Matricardi and Saunders (1999); Chalon et al. (2001)] has been designed as an advanced infrared sounder on the new generation of operational meteorological polar orbiter by the Center Nationale d'Etudes Spatiale (CNES) in the framework of a cooperative agreement with EUMETSAT. In combination with the Advanced Microwave Sounding Unit (AMSU), the Microwave Humidity Sounder (MHS), and the Advanced Very High Resolution

Table 2.1 Characteristics of satellite advanced infrared sounders

Name	AIRS	IASI	CrIS	IRFS-2	IRS
Orbit	705km	833km	824km	850km	Geostationary
Instrument type	grating	FTS	FTS	FTS	FTS
Agency	NASA	EUMETSAT	IPO	RSA	EUMETSAT
Spectral range (cm^1)	649-1135 1217-1613 2169-2674	Contiguous 645-2760	650-1095 1210-1750 2155-2550	Contiguous 665-2000	685-1130 1650-2250
Unapodized spe -ctral resolving power($\nu/\delta\nu$)	1200	2000-4000	1000-1800	2000-4000	2000-4000
Field of view(km)	13	12	14	35	4
Sampling density per 50km square	9	4	9	1	144
Power(W)	225	200	86	50	300
Mass(kg)	140	230	81	50	200
Platform	Aqua	Metop-A,B,C	Suomi-NPP JPSS	METEOR	Geostationary
Launch date	2002	2006,2012 2017	2011(NPP) 2017(JPSS-1)	2014	2017

Radiometer (AVHRR),this is the core payload of the European Organization for Exploitation of Meteorological Satellite (Metop-2) which was successfully launched into orbit on 19 October 2006. The second and third instruments will be mounted on the Metop-B and C satellites with launches scheduled in 2012 and 2016/17 respectively, to provide a continuous long-term data record. The goal of IASI is to improve medium range weather forecasts by providing global operational meteorological soundings. Detecting and monitoring global trace gases including ozone, methane and carbon monoxide is another IASI's goal.

The IASI spatially scans perpendicular to the satellite obit track, the scan process is step by step, with rapid move between the different look positions, and a stop during each look (acquisition of interferogram). The optical axis moves from -47.85 degrees to +47.85 degrees in relation to the nadir. With the orbit height of Metop being about 840 km, the IASI swath (length of ground measurement track) is about approximately 2400 km corresponding 30 mirror positions. As shown in figure(2.4),

there are 30 scene viewing positions along the measurement track. Thus, the IASI total angular field-of-view (FOV) is conical with a vertex angle of 3.3 × 3.3 degrees or 50 km × 50 km at nadir. It is composed by a matrix of 2 × 2 circular cells corresponding to a 1.25 degree angle, with centers positioned on lines and columns located at ±0.825 degrees from the instrument optical axis. On the ground, each cell of the analysis matrix corresponds to a circular pixel of 12 km diameter at a sub-satellite point.

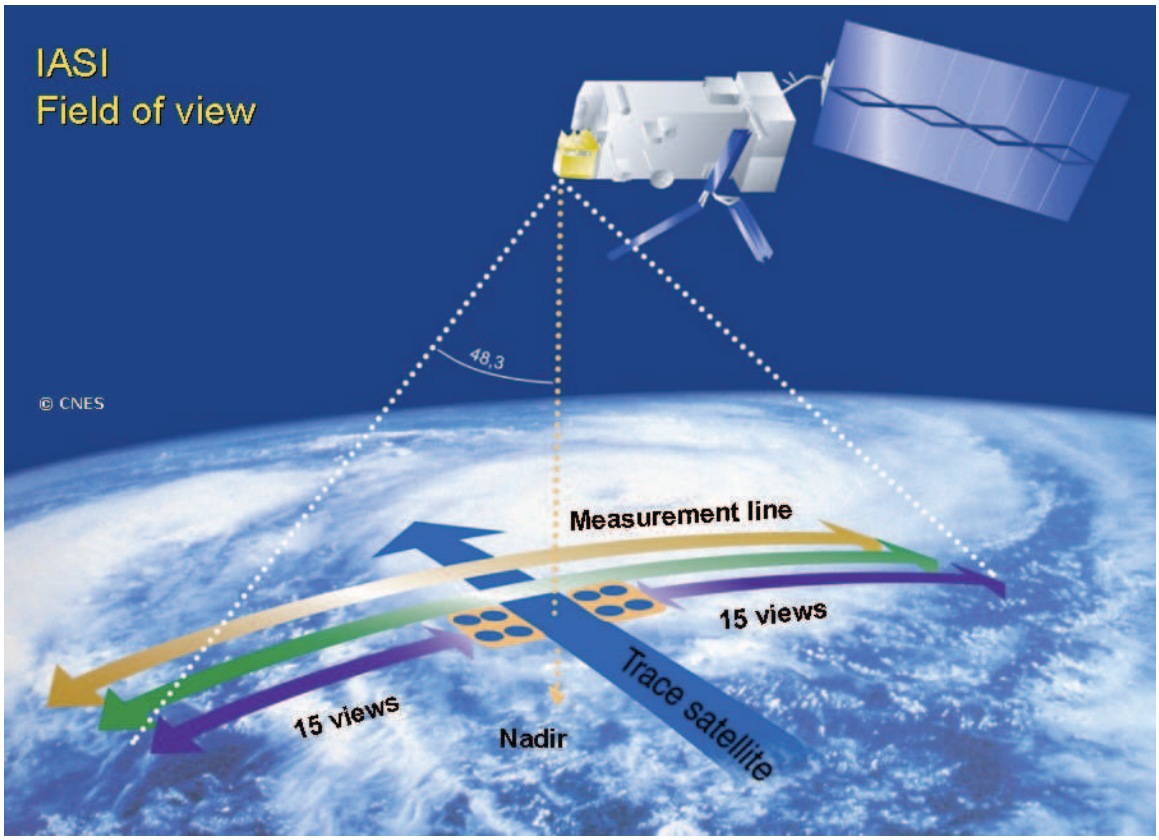

Figure 2.4 IASI field of view

The IASI instrument is a Fourier-transform spectrometer. The diagram of this innovative instrument is shown in the figure(2.5). The design of interferometer is based on a classical Michelson instrument. The IASI has a constant spectral sampling interval of 0.25 cm^{-1} which was driven by the 2-cm FTS optical path, and it covers the spectral range form the CH_4 absorption band at 3.62 μm (2760 cm^{-1}) to the

CO_2 absorbtion band at 15.5 μm (645 cm^{-1}) with a self-apodized spectral resolution between 0.35 and 0.5 cm^{-1}. The apodized instrument function is a Gaussian with a 1/e point at 0.25 cm^{-1}.

The optical configuration of IASI, along the light path through the instrument are:

-Scan mirror. Fluid lubricated bearings are used for the step by step scene scanning and the field motion compensation device is based on flexural blade pivot.

-Off-axis afocal telescope that transfer the aperture stop onto the scan mirror.

-Michelson interferometer,including a beamsplitter, a compensating plate and two corner cube mirrors: one corner cube move linearly by $\pm$1 cm within 151 milliseconds, which corresponds to an optical path difference of 2 cm, necessary to obtain the specified spectral resolution. In a operating instrument, a 1.54 μm frequency-stabilized laser is injected into the interferometer. The interferometer output of the laser beam is used as a reference to sample the interferogram.

-A folding mirror directs the recombined beams onto the off-axis focusing mirror, which images the earth at the entrance of the cold box.

-The cold box contains field and aperture stops.

The IASI Level 1 processing generates calibrated and apodized atmospheric spectra (Level 1C data) from raw interferograms. The raw spectra are of high radiometric quality, with a noise equivalent temperature difference lower than 0.2K for wavenumbers lower than 2200 cm^{-1}, except for the narrow portion between 1800 and 2000 cm^{-1} where it approaches 0.3K (see Figure(2.6)). As a guideline to these high performances, the noise is well below 0.1K between 1150 and 1500 cm^{-1}. It starts to increase above 2500 cm^{-1}, where the TIR emission drops.

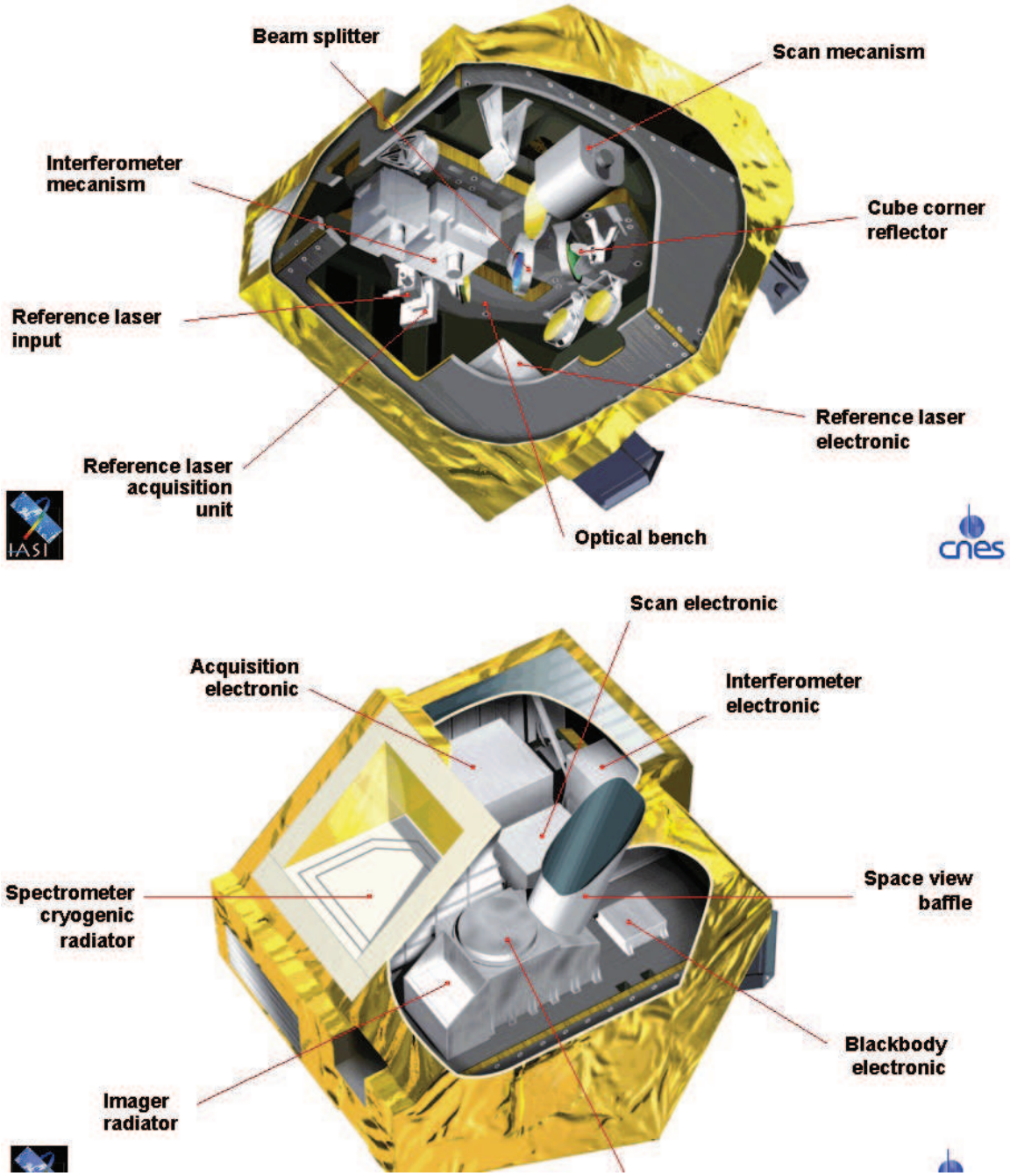

Figure 2.5 Scheme of IASI instrument

2.3 Ground based hyper-spectral radiometer

Smith first proposed using ground-based infrared instruments to retrieve atmospheric temperature profiles from infrared radiance [Smith (1970)]. In 1988, dur-

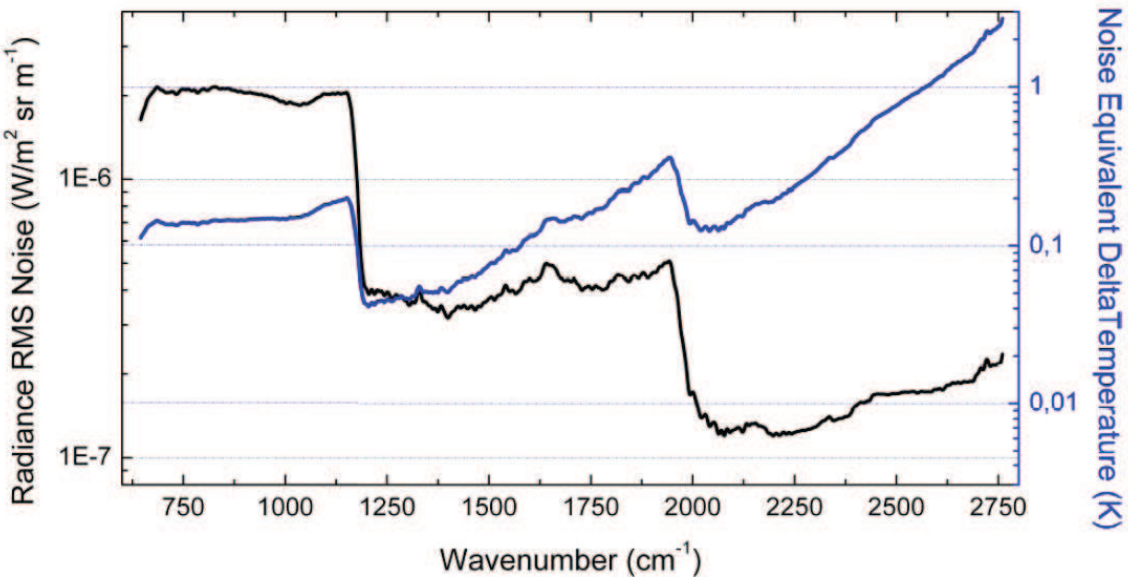

Figure 2.6 IASI radiometric noise as established from a set of representative spectra. Values are provided in radiance units (W/(m^2 srm.1), black line, left scale), and were converted to noise equivalent temperature difference (Ne1T , blue line, right scale) for a given reference temperature of 280 K.

ing the Ground-based Atmospheric Profiling Experiment(GAPEX), the advantage of retrieving lower atmospheric temperature and water vapor profiles from a ground based interferometer was demonstrated by using the High-resolution Interferometer Sounder (HIS) aircraft instrument looking upward from the surface. The temperature and water vapor retrieval result compared favorably with radiosondes used as ground truth[Smith et al. (1990)]. Motivated by GAPEX result, the Department of Energy's Atmospheric Radiation Measurement (ARM) program funded the development of AERI to meet the needs of the ARM Program for to continuously monitoring atmospheric downwelling 0.5-wavenumber spectral resolution infrared radiance for studies of both clear-sky molecular emission and cloud-radiative properties[Revercomb et al. (1995); Smith et al. (1993)]. The clear-sky AERI observations are contributing to a better understanding of infrared spectroscopic issues, such as the water vapor continuum absorption.

2.3.1 AERI instrument description

Atmospheric Emitted Radiance Interferometer (AERI) is an advanced version of the high-resolution interferometer sounder [Revercomb et al. (1988)] developed and fabricated at the Space Science and Engineering Center (SSEC) at the University of Wisconsin-Madison, Madison, Wisconsin, which has a long history of developing aircraft and ground-based interferometer instrument and software to obtain calibrated infrared radiances. The instrument is portable, robust, and field hardened so it could be installed at the three Department of Energy (DOE) Atmospheric Radiation Measurement Program (ARM) field sites (South Great Plains site in north central Oklahoma, North Slope of Alaska site in Barrow Alaska, and Tropical Western Pacific site on the equatorial island of Nauru) and other ARM mobile facilities in Germany, Portugal, China, India, Niger and California[McMillan et al. (2001); Knuteson et al. (2004a,b)](figure(2.7)). There are couple variants of AERI including the Marine-AERI (M-AERI)[Minnett et al. (2001)] mounted on the vessels to participate the AEROSE expeditions and the Polar-AERI (P-AERI)[Walden et al. (2006)] installed at the Antarctic plateau.

The AERI (figure(2.8)) is a fully automated ground-based passive infrared interferometer that measures downwelling atmospheric radiance in the 3.3 to 18.2 -μm (550-3000 cm^{-1}) region of the infrared spectrum at about half wave number resolution and at a less than 10-min temporal resolution. With careful calibration, the instrument can yield absolute calibration accuracy to better than 0.5 % of the ambient radiance. These radiances contain valuable information about the vertical thermal and moisture structure in the atmosphere below 3 km. Furthermore, If the view angle of instrument was varied, the surface properties such as skin temperature and surface spectra emissivity can be calculated as with the M-AERI measurements in AEROSE expeditions [Smith et al. (1996)].

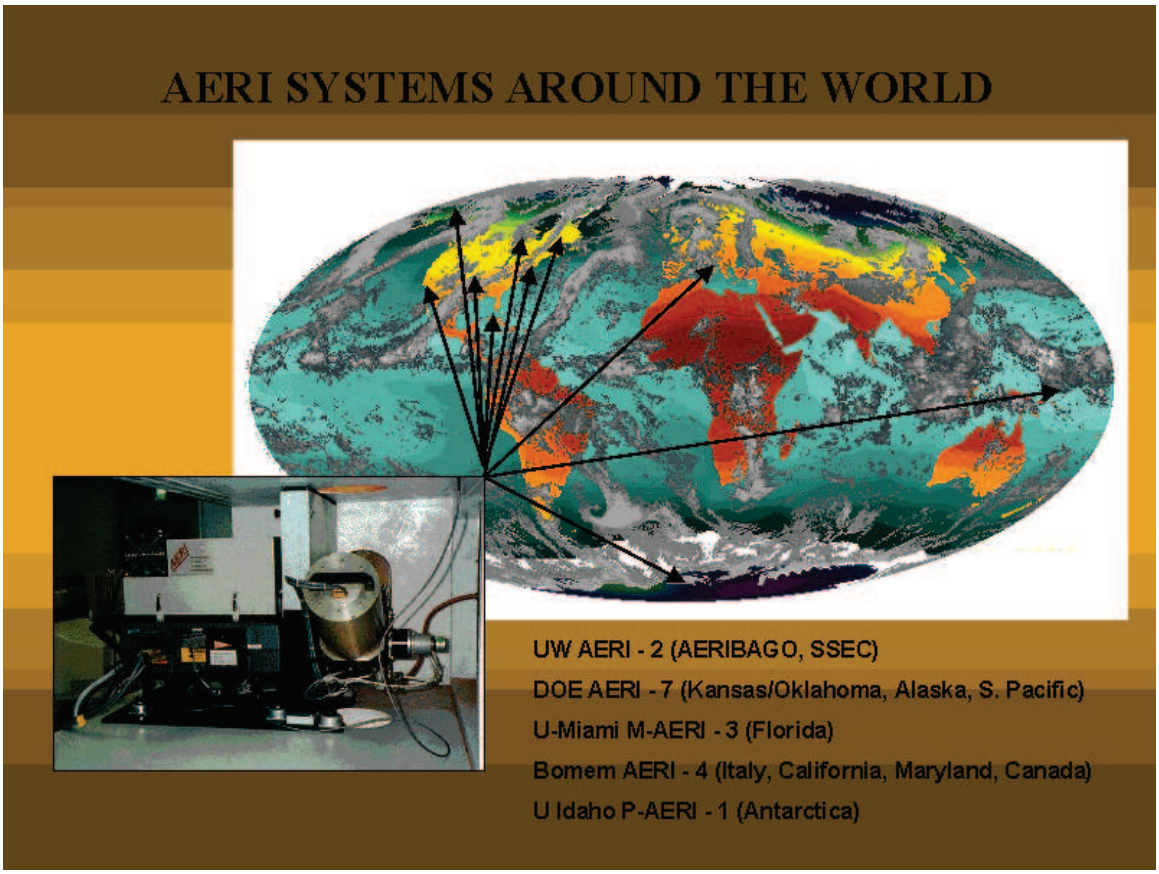

Figure 2.7 AERI systems around world

The AERI instrument optical configuration consists of a two-brand, Michelson interferometer; two detectors (5-20 and 3-5 μm); a scene-imaging scan mirror; and a two-point calibration system. The scheme of the interferometer is described as follows: (1)the downwelling infrared radiation enters the top the instrument and encounters the scene scan mirror, (2)the incoming IR radiation is reflected toward a beam splitter as it strikes the scan mirror, (3)after the splitter, one portion of radiation is reflected onto one moving mirror, while the other portion is transmitted onto another mirror moving in the opposite direction, (4)the two beams are reflected back to the beam splitter, where they are recombined, and (5)an interference pattern call an interferogram is created. Constructive or destructive interference occurs as a result of the optical path difference between the two beams within the interferogram.

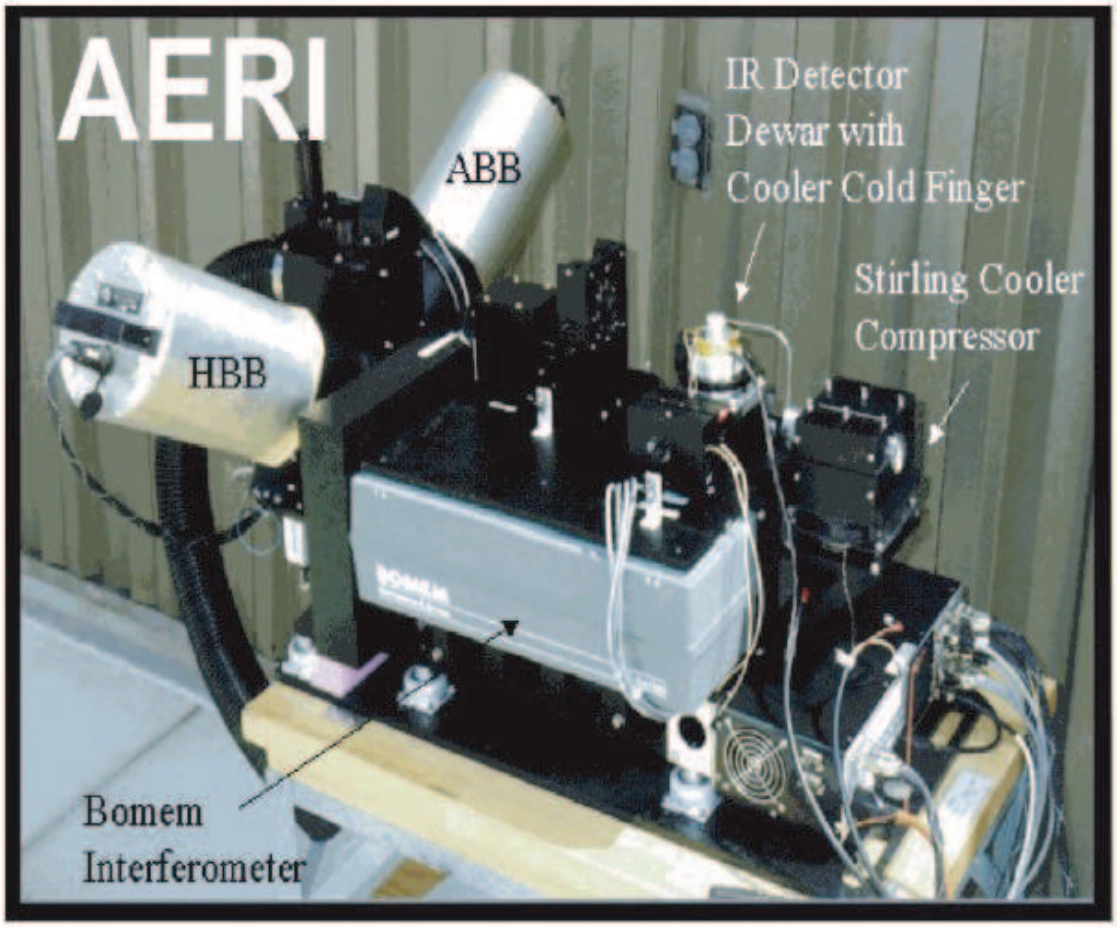

Figure 2.8 AERI Instrument

The result is the summation of all interference patterns caused by every wavelength of the earth's electromagnetic spectrum.

An operating AERI instrument consists of a typical 10-min measurement cycle that includes a 3-min sky dwelled period followed by 2-min dwell periods for each of two black bodies. An uncalibrated spectrum is obtained in every 2 seconds, the spectrum sets are averaged over a 3-min time period (90 samples) to reduce radiometric noise and to decrease data volume. The operational calibration system consists of "hot" and "ambient" high-emissivity black bodies, which are kept at fixed 333 K and at fluctuating ambient air temperature, respectively. Both of the AERI calibration reference sources are high-emissivity black body cavities that contain highly accurate

temperature sensors. Calibration error analysis shows that for an instrument that must operate within an ambient atmospheric environment, the extrapolation of the hot-ambient calibration to the coldest ambient scene temperature has a comparable accuracy to a calibration that makes use of a stable cold target. This is because the temperature and emissivity uncertainty in reference cavities operated at or above ambient temperature can be made much smaller than those typically operatings below the dew point temperature.

Because the AERI system performs a self calibration every 10 min, before and after each sky view, any temperature drifts in the ambient black body or the internal instrument temperature are accurately accounted for. One the advantages of using an ambient calibration point is that much of the emission that the AERI measures is radiating from the low levels of atmosphere near the environmental ambient temperature. This means that the emission from near the surface is measured very precisely with AERI instrument. This hot-ambient approach greatly simplifies the operations of the instrument by removing the requirement for bulk of liquid nitrogen to provide a cold calibration source (*Revercomb et al.*, 1988). On the other hand, the temperature detectors in Blackbodies (a sandwiched HgCdTe/InSb detector, providing sensitivity for 5.5-18.2 and 3.3-5.5 μm, respectively) requires cooling. A mechanical Stirling cooler is used to cool the detectors.

2.3.2 Maritime-AERI (MAERI) and ASSIST

In our research, beside the data measured by AERI, the downwelling radiance spectra measured by two other spectrometers (M-AERI and ASSIST), which are both variants of AERI, were also used for the profile the retrieval. High-resolution atmospheric and ocean spectra are provided by the Marine Atmospheric Emitted Radiance Interferometer (M-AERI). M-AERI is a ship based Fourier transform spectrometer (FTS) which measures IR radiance spectra from upwelling and downwelling directions

near the surface. M-AERI observations are made on the 02 Deck on the starboard side looking forward on the NOAA ship Ronald H. Brown, with one downward viewing and two upward viewing angles [Nalli, et al., 2006]. The downward view allows measurements of upwelling radiation from the ocean at 55^o, while the upward views allow measurements of downwelling atmospheric radiation at 0^o and 55^o [Nalli, et al., 2006]. M-AERI spectra are used to derive important geophysical parameters such as radiometric sea surface skin temperature, IR spectral emissivity, and boundary layer temperature and water vapor [Nalli, et al., 2011].

Figure 2.9 The M-AERI installed on the NOAAS Ronald H. Brown. The instrument is on the forward 02 deck at the starboard railing. The field of view intersects the sea surface ahead of the bow wave.

Sponsored by the Department of Energy (DoE) National Nuclear Security Administration (NNSA), the Atmospheric Sounder Spectrometer for Infrared Spectral Technology (ASSIST) has been developed in order to support upwelling and downwelling radiance measurements for ground truth validation. The primary purpose

of the ASSIST is to monitor the atmospheric column, water mixing ratio and temperature profiles, during remote sensing tests. The ASSIST radiance observations enable precise determinations of the PBL thermodynamic profiles, as well as trace gas, aerosol, and cloud properties, important for characterizing the atmosphere's meteorological, chemical, and radiative properties. The second purpose of the ASSIST remote sensing and evaluation program is to measure the upwelling radiance from calibration and material targets. These measurements will be utilized for several purposes to include ground truth monitoring of calibration targets, long-term solid signature migration research, and spectral signature discovery on various substrates.

Like AERI, the ASSIST spectrometer (figure(2.10)) is base on a four-port configuration Michelson interferometer using a flex pivot as the scanning mechanism. The instrument sub modules are including 5 sub-modules: Michelson interferometer assembly; Calibration unit; AFT optics and detectors; Acquisition, housekeeping modules and platform manager; and Environment Enclosure.

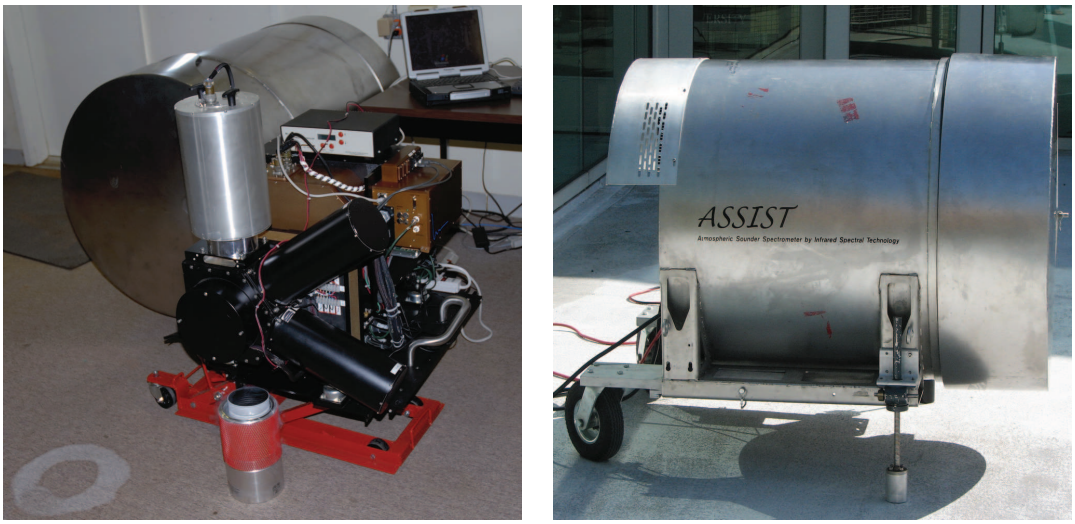

Figure 2.10 ASSIST platform and enclosure

The ASSIST interferometer is based on a double beam modulator using the corner cube configuration. It utilizes an internal He-Ne laser emitting at 15798cm-1 in the interferometer module. This monochromatic laser radiation gives a sinusoidal inter-

ferogram, which is detected and digitized to provide the optical path difference (OPD) feedback. The calibration unit is similar to AERI, which includes two blackbodies. These two blackbodies are cavities with a clear aperture of 6.8 cm. Each of the cavities use 3 thermistors located at different positions of the cavity allowing a better characterisation and control of the cavity temperature. The controller can control 2 blackbodies and offer a read out precision of ± 2 Millikelvins with a control accuracy of 5 millikelvin (ADC 22 bits). The calibration of ASSIST has be validated by radiative transfer calculation based on the in situ radiosondes and through comparison of side-by-side AERI measurements.

CHAPTER 3

THEORY OF RETRIEVAL

3.1 Radiative Transfer model

Radiative transfer serves as a mechanism for exchange energy between the atmosphere and the underlying surface and between different layers of the atmosphere. Infrared radiation emitted by the atmosphere and detected by a satellite or ground-based sensors is the basis for remote sensing of atmosphere structure. For most remote sensing applications, notably the assimilation of satellite radiance in near real time, fast and accurate radiative transfer models (RTMs), which simulate observed radiance, are required. Radiative transfer models are also the core of the retrieval procedure.

Excluding effects of any absorbers such as clouds or aerosols, the upwelling spectral radiative transfer model can be expressed as:

$$R^{\uparrow}(\nu) = \epsilon(\nu)B_s(\nu, T_s)\tau_s - \int_{P_{TOA}}^{P_S} B(\nu, T)d\tau_{\nu}^{\uparrow}(P) + (1-\epsilon(\nu))\int_{P_{TOA}}^{P_S} B(\nu, T)d\tau_{\nu}^{*}, \quad (3.1.1)$$

without the contribution of surface emittance the downwelling radiative transfer model has more simply form:

$$R^{\downarrow}(\nu) = -\int_{P_S}^{P_{TOA}} B(\nu, T)d\tau_{\nu}^{\downarrow}(P), \quad (3.1.2)$$

where $R^{\uparrow}(\nu)$ / $R^{\downarrow}(\nu)$is the up/downwelling spectral radiance at certain frequency ν respectively; $B(\nu, T)$ is Planck function at wave number ν and temperature T which can be calculated by following function:

$$B(\nu, T) = \frac{C_1 \nu^3}{e^{\frac{C_2 \nu}{T}} - 1},$$

$C_1 = 1.191066 \cdot 10^{-5} (mW/m^2/ster/cm^{-4})$,

$C_2 = 1.438833 (cm \cdot deg \cdot K)$.

ϵ refers to Earth's surface emissivity; $\tau_\nu^\uparrow(P)$ is the spectral atmospheric transmittance from any given pressure P to the top of atmospheric P_{TOA}, while $\tau_\nu^\downarrow(P)$ is the spectral atmospheric transmittance from surface P_S to given pressure P, τ_s is the total transmittance from surface to the top of atmosphere, and $\tau_\nu^* = \tau_s^2/\tau_\nu^\uparrow$

3.1.1 Line-by-Line Radiative transfer model

To calculate the absorption of radiation by molecules in the atmosphere accurately is very critical to the implementation of various remote sensing techniques. The line-by-line models are the most accurate radiative transfer models for accounting molecular absorption. Most recently, Kratz et al. have demonstrated that the line-by-line methods are quite accurate in the far infrared spectral region[Kratza et al. (2005)]. In Support of the IASI mission the IASI Sounder Science Working Group (ISSWG) initiated an international LBL inter-comparison experiment to validate the simulation accuracy of Line-by-line model on IASI measurement[Tjemkes et al. (2003)]. In this inter-comparison, seven different line-by-line algorithms namely LBLRTM[Clough et al. (1992)], GENLN2[Edwards (1992)], HARTCODE[Rizzi et al. (1992)], KOPRA[Clarmann et al. (2000)], LARA, LITMS[Trotsenko and Formin (1989)], and 4A00[Scott and Chédin (1981)] were selected to simulate aircraft HIS observations, which were then compared to real observations. The simulation results indicated that most line-by-line models can simulate the IASI measurements with relative high accuracy within most of the spectral interval between 650 and 2600 cm^{-1} region.

The line-by-line spectral calculation requires the detailed line shape of gas involved calculation. Each molecule of each active gas undergoes internal transition as it exchanges radiation energy with environment, and each transition is associated with a spectral line at a certain characteristic frequency. And each line has a broaden shape because the exchange of energy is distributed around that frequency grid due to various mechanisms such as collisions. Therefore, the optical depth at each spectral grid include individual contributions from every significant line. Each absorption line can be characterized by its central frequency, strength and pressure normalized half-width at particular reference temperature. All these information are stored in the molecular line database called HITRAN[Rothman et al. (1987, 1992)]. Besides this molecular line database, the line-by-line models may need the coefficients for the continuum contributions of water vapor.

In the line-by-line computing, at each frequency grid, model obtains data for the contributing lines from HITRAN, adjusts them to the layer condition, determines the contribution of each line to the layer attenuation, then combine these contributions to generate the optical depth across the layer. Once this procedure is repeated for every layer of atmosphere to obtain the optical depth, the monochromatic transmittance from each layer to ground surface or space can be calculated by taking the negative exponential function on the summation of the optical depths. This process must be repeated for each broaden line the spectral grid. Since there are tens of thousands of spectral lines, the line-by-line models get a significant computation problem.

The Line-by-Line Radiative transfer model (hereafter referred as LBLRTM) developed by Atmospheric and Environmental Research Inc. is based on the FASCODE [Clough et al. (1981)]. The LBLRTM has very strong flexibility that can be used over the full spectral range from microwave to the ultraviolet, providing the foundation for many radiative transfer application. The long and successful heritage of LBLRTM

makes it been widely used for a number years as the starting point for many retrieval algorithms

The LBLRTM has three features: it has been and will to be extensively validated against atmospheric radiance spectra, it incorporates a full water vapor continuum model (CKD) [Clough et al. (1989)] which includes self- and foreign-broadened water vapor as well as continua for carbon dioxide, oxygen, nitrogen, ozone and extinction due to Rayleigh scattering is incorporated in the LBLRTM model, and its relatively computational efficiency.

LBLRTM includes the following attributes: (1) the Voigt line shape is used at all atmospheric levels with an algorithm based on a linear combination of approximation function, (2) all parameters on the HITRAN line database are used, including the pressure shift coefficient, the half width temperature dependence, and the coefficient for the self-broadening of water vapor; (3) a version of the Total Internal Partition Function (TIPS) program is used for the temperature dependence of the line intensities [*Gamache et al.*, 1990]; (4) the effects of line coupling are treated to second order with the coefficients for carbon dioxide in the 600-800 cm^{-1} region included explicitly; (5) temperature dependent cross-section data such as those available with the HITRAN database may be used to treat absorption due to heavy molecules,(e.g., the halocarbons); (6) an algorithm is implemented for the treatment for the variation of the Planck function within a vertically inhomogeneous layer; (7) Fast Fourier Transform (FFT) instrument function is included in the apodziation of monochromatic radiance to simulate instrument measurement.

Those attributes provide spectral radiance calculations with accuracies consistent with the measurement accuracies. Algorithmic accuracy of LBLRTM is approximately 0.5% and the errors associated with the computational procedures are of the order of five times lees than the errors associated with the line parameters. The

LBLRTM line parameter inputs are obtained by running the LNFL program on the ASCII spectroscopic line database for the spectral lines.

3.1.2 Fast Forward Model

Though the line-by-line radiative transfer model provides very accurate radiance simulation from the provided atmospheric profiles, the computation through the inhomogeneous atmosphoere is still time-consuming process. In infrared region, most molecular gases in the atmosphere have numerous vibrational-rotational transitions, or pure rotational transitions. Molecular line intensities and shapes are nonlinear function of vertical profiles of atmospheric temperature, pressure and concentration of gases. The inhomogeneous atmosphere has to be divided into numerous thin layers and use properly weighted atmospheric properties within these layers for the calculation. Since the line-width are very small in the upper atmosphere, the monochromatic calculation interval is about 0.0001-0.0008 wavenumber in the infreared spectral region. For example the IASI instrument spectral coverage ranges from 645 to 2760 cm^{-1} with an average wavenumber interval of 0.0004 cm^{-1}; thus there are about 6 $\times$ 10^6 monochromatic radiative transfer calculations for whole spectral range. It is necessary to apply a fast accurate enough forward model to replace the line-by-line model in the retrieval practise.

There are several forward model approaches to minimize the computational time. The model of the TES science team used is to store absorption coefficients as a function of atmospheric state at a monochromatic frequency grid in a large lookup table. Then the optical depth at a particular pressure layer can be calculated by interpolations or additions. The approach can avoid the burden calculations of spectral line shapes and intensities, but it still involve numerous monochromatic radiative transfer calculation to obtain atmospheric radiance. To minimize the calculations and to take advantage of the high spectral resolution and high information content of mea-

surements, the TES science team selects narrow microwindows to perform retrievals for a specific trace gas. Unfortunately, this approach does not apply all channels simultaneously to produce a simultaneous retrieval for all the desired atmospheric parameters.

Another method of parameterization is to predict channel transmittances or radiances by using a a few representative monochromatic transmittances or radiance. Correlative-k distribution (CKD) [Lacis and Oinas (1991); Gerstell (1993)], exponential sum fitting transmittance (ESFT) [Wiscombe and Evans (1997); Armbruster and Fischer (1996)], and optimal spectral sampling (OSS) [Liu et al. (2003); Moncet et al. (2004)] are examples of this type of fast RT models approach. In this approach, the channel radiances or transmittances are calculated in:

$$R^{ch}(\nu) = \int_{\Delta\nu} \phi(\nu - \nu') R^{mono}(\nu') d\nu' = \sum_{i=1}^{N} w_i R^{mono}_{\nu_i}, \tag{3.1.3}$$

$$t^{ch}(\nu) = \int_{\Delta\nu} \phi(\nu - \nu') t^{mono}(\nu') d\nu' = \sum_{i=1}^{N} w_i t^{mono}_{\nu_i}. \tag{3.1.4}$$

In equations, $R^{ch}(\nu)$ and $t^{ch}(\nu)$ represent channel radiances and transmittance at a center frequency ν, and w_i is the weight for the predetermined monochromatic radiance of transmittance. Both CKD and ESFT methods have the advantage of computing efficiency and accuracy for single atmospheric layer. One the other hand, both models are usually trained on one atmospheric layer, and the dependency of channel transmittance on pressure, temperature, and gas amounts are introduced later by assuming good correlation between vertical layers and no correlation between overlapping gases. Extending them to the vertically inhomogeneous atmosphere leads to limited accuracy. To overcame this drawback, the OSS model was developed by AER. The OSS model fits TOA channel radiances using a robust ESFT minimization scheme, where 1-15 monochromatic radiative transfer calculations are needed to pre-

dict channel radiance and layer or space-to-layer transmittances. The OSS model is planned to be used to process the CrIS and Advanced Technology Microwave Sounder (ATMS) data from Suomi-NPP and forthcoming JPSS satellites.

Another forward model approach is to predict layer effective optical depths by using an efficient fast parameterization. Assuming the transmittance is the type described by [McMillin and Fleming (1976); Eyre and Woolf (1988), thus the spectral transmittance at a certain frequency ν to a radiometer along a given atmospheric path at zenith angle θ from a given pressure level p_j can be written as:

$$\tau_j^\nu(\theta) = \tau_{j-1}^\nu(\theta) \exp[-\Delta\sigma_j^\nu(\theta)], \tag{3.1.5}$$

where $\Delta\sigma_j^\nu(\theta)$ is the slant-path optical depth across the jth layer, which is regarded as homogeneous, and is determined by the representative pressure p_j, temperature T_j and absorber gas amount n_j; it is the layer attenuation caused by the net gaseous absorption along the path. If a reference profile (r) is chosen, the Eq.(3.1.5) can be deducted as:

$$\frac{[\tau_j^\nu(\theta)/\tau_{j-1}^\nu(\theta)]}{\tau_j^{\nu,r}(\theta^r)/\tau_{j-1}^{\nu,r}(\theta^r)} = \exp\{-[\Delta\sigma_j^\nu(\theta) - \Delta\sigma_j^{\nu,r}(\theta^r)]\} \tag{3.1.6}$$

This may be approximated by the low-order terms of a multivariate Taylor expansion about the reference profile. When the logs are taken, it can be written in the form of

$$\sigma_j^\nu(\theta) = \sigma_{j-1}^\nu(\theta) + \sum_k a_{jk}^\nu X_k, \tag{3.1.7}$$

where $\sigma_j^\nu(\theta)$ is the spectral optical depth at frequency ν for a slant path at zenith angle θ from the jth level to space. The $k$the predictor is denoted by X_k, and one of them will represent the constant term contributed by then r-labeled reference quantity on the left-hand side in Eq.(reftau2). The other predictors on in Eq(3.1.7) will each depend on one or more profile elements drawn from the set of difference

$\delta T_j = (T_j - T_j^r)$ and $\delta n_j = (n_j - n_j^r)$, and perhaps also from the deviation of vier angle θ, here the same for all levels j, from nadir.

Equation (3.1.8) indicates how the layer effective optical depth is calculated:

$$\begin{aligned}\tau_{eff}^{ch}(l) &= -\ln \frac{\int_{\Delta\nu} \phi(\nu - \nu') t^{mono}(\nu, l) d\nu'}{\int_{\Delta\nu} \phi(\nu - \nu') t^{mono}(\nu, l-1) d\nu'} \\ &= -\ln \frac{t^{ch}(\nu, l)}{t^{ch}(\nu, l-1)} \\ &= \text{Func}[\sec(\theta), T_r, T_z(P, T_r), W, O, M \ldots], \end{aligned} \tag{3.1.8}$$

where τ is the effective channel layer optical depth, ϕ is the normalized SRF, $\Delta\mu$ is the spectral span of the SRF, l is the atmospheric layer index, t^{mono} and t^{ch} are monochromatic and channel transmittance, respectively. T_z is the pressure weighted layer temperature ratio above l^{th} layer , and T_r is the ratio of the layer average temperature to a layer reference temperature. θ is the satellite zenith angle and P is the atmospheric pressure. W, O, M are the water amount ratio, ozone amount ratio and methane amount ratio respectively. This variables list can be expended to other trace gases.

There are several fast model parameterizations based on the effective optical depth for satellite remote sensing applications. Optical path transmittance (OPTRAN)[*McMillin et al.*,1995], stand-alone radiative transfer algorithm (SARTA)[*Saunders et al.*,1999], and radiative transfer for TIROS Operational Vertical Sounder(RTTOVS)[*Stow et al.*,2003] are three well known fast models of this kind. These fast parameterizations have been successfully applied in several operational satellite borne detectors such as High Resolution Infrared Radiation Sounder (HIRS), Advanced Microwave Sounding Unit (AMSU), and AIRS.

In numerical practice, to generate the database of the fast forward model, a line-by-line radiative transfer models is used to compute the monochromatic optical depths for a set of specified atmospheric profiles on a fixed pressure grid. These monochromatic optical depths are converted to atmospheric transmittances to the surface or to

space, which are then convolved with a spectral response function of the instrument to yield effective transmittances. The effective transmittances are then apodized to reduce the convolution-induced "ringing". These convolved and apodized transmittance are the converted back into layer effective optical depths. Regression relations are then used to relate these optical depths to the atmospheric state at each pressure level for each spectral element.

There is another fast approach to simulate radiance spectra in a different way. Unlike the models described above which calculate channel transmittance by using nonlinear functions of atmospheric temperature and gas profiles, the principle component based radiative transfer model (PCRTM) predicts the principal component (PC) scores, which has less dimensions as compared to the number of spectral channels. The physical base of PCRTM is following: for monochromatic spectra, many absorption lines have similar Lorentz or Doppler half-width, and dependencies of the line strength and half-width on atmospheric status are similar, thus the number of independent pieces of information is much less than the number of monochromatic spectra.

SARTA fast forward Model

The Stand-alone AIRS Radiative Transfer Algorithm (SARTA) effectively parameterizes atmospheric transmittances in 100 pressure layers [Strow et al. (2003)] by using the instrumental spectral response functions (SRFs).

The regression training data set consists of 48 profiles, each calculated at 6 viewing angles between 0 and 60 degrees (measured from the vertical, i.e., nadir=0 degrees). The 48 profiles were selected to span the expected range of profile varibility. The monochromatic transmittances for each profiles were calculated by using KCARTA code, and includes all gases contained in 2002 HITRAN database. The pressure coordination of SARTA fast forward model covers from 1000 hPa to 0.005 hPa($\sim$

80km). The pressure grid is establised according to $p(i) = (a \times i^2 + b \times i + c)^{7/2}$, the parameters of a, b, and c are determined by solving the equation of $p(1)$ =1100 mbars, $p(38)$ = 300 mbars, and $p(101) = 5 \times 10^{-3}$ mbars.

Table 3.1 Pressure (hPa) grid of SARTA fast model

0.0050	0.0161	0.0384	0.0769	0.1377	0.2244	0.3454	0.5064	0.7140
0.9753	1.2972	1.6872	2.1526	2.7009	3.3398	4.0770	4.9204	5.8776
6.9567	8.1655	9.5119	11.0038	12.6492	14.4559	16.4318	18.5847	20.9224
23.4526	26.1829	29.1210	32.2744	35.6504	39.2566	43.1001	47.1882	51.5278
56.1259	60.9895	66.1252	71.5398	77.2395	83.2310	89.5203	96.1138	103.017
110.237	117.777	125.646	133.846	142.385	151.266	160.496	170.078	180.018
190.320	200.989	212.028	223.441	235.234	247.408	259.969	272.919	286.262
300.000	314.137	328.675	343.618	358.966	374.724	390.892	407.474	424.470
441.882	459.712	477.961	496.630	515.720	535.232	555.167	575.525	596.306
617.511	639.140	661.192	683.667	706.565	729.886	753.627	777.789	802.371
827.371	852.788	878.620	904.866	931.523	958.591	986.066	1013.95	1042.23
1070.92	1100.00							

The layer effective optical depths are modeled as simple function of various profile dependent predictors. Typically these predictors are terms related to the layer temperature, absorber amount, and viewing angle. The SARTA fast model uses seven main sets of predictors for the optical depths. The predictors are based upon simple functions involved basic atmospheric state variables for the given profiles. These are:

$P(i)$: mean air pressure in layer i

$T(i)$: mean air temperature in layer i

$W(i)$: Water amount in layer i

$O(i)$: Ozone amount in layer i

$M(i)$: Methane amount in layer i

$C(i)$: CO amount in layer i

The gas amount used here refer to the molecular amount of the absorber contained within the layer along a nadir path. This is sometimes called a column amount or an integrated cross-sectional density, and typically has units of molecules per square centimeters.

The predictor tables use the following notations:

Table 3.2 Temperature predictors for SARTA model

index	set 1,2,3	set4	set 5	set 6,7
1	a	a	a	a
2	a^2	a^2	a^2	a^2
3	aT_r	aT_r	aT_r	aT_r
4	aT_r^2	aT_r^2	aT_r^2	aT_r^2
5	T_r	T_r	T_r	T_r
6	T_r^2	T_r^2	T_r^2	T_r^2
7	aT_z	aT_z	aT_z	aT_z
8	aT_z/T_r	a^2T_z	aT_z/T_r	$\sqrt{a}$
9		a^2T_r	a^2T_r	
10		a^3	$\sqrt{a}$	
11		$\sqrt{a}$	T_z	

a : secant of the path zenith angle

T_r : Temperature ratio T_{prof}/T_{ref}

ΔT : Temperature difference $T_{prof} - T_{ref}$

W : Water amount ratio W_{prof}/W_{ref}

O : Ozone amount ratio O_{prof}/O_{ref}

P : layer mean pressure

T_z : pressure weighted temperature ratio

W_z : pressure weighted water ratio

O_z : pressure weighted ozone ratio

O_x : ozone ratio

T_o : pressure and ozone weighted temperature difference

AERI fast forward Model

The AERI fast forward model is a variant of RTTOVS [*Eyre*,1991; *Garand*,2001). For the first two ARM versions of AERIPROF retrieval programs, the AERI fast forward model was based on the Fast Atmospheric Signature Code (FASCODE) [*Clough et al.*, 1981] line-by-line model using the water vapor continuum absorption model CKD v2.1 [*Clough et al.*, 1989]. However, the validation research conducted by ARM

Table 3.3 Water line predictors for SARTA model

index	set1	set2	set3	set4
1	aW	aW	aW	aW
2	$\sqrt{aW}$	$\sqrt{aW}$	$\sqrt{aW}$	W
3	aWW/W_z	$aW\Delta T$	aWW/W_z	$\sqrt{aW}$
4	$aW\Delta T$	$aW(aO_x)$	$aW\Delta T$	$aW\Delta T$
5	$(aW)^2$	$(aW)^2$	$(aW)^2$	$(aW)^2$
6	$\sqrt{aW}\Delta T$	$\sqrt[4]{aW}$	$\sqrt{aW}\Delta T$	$\sqrt{aW}\Delta T$
7	$\sqrt[4]{aW}$	$\sqrt{aW}\Delta T$	$\sqrt[4]{aW}$	$\sqrt[4]{aW}$
8	$\sqrt{aW}W/W_z$	aWW/W_z	$(aW)^3$	aWW/W_z
9	$(aW)^3$	$(aW)^3$	W	aWa
10	W	$aW(aO_x)^2$	$\sqrt{aW}W/W_z$	$(aW)^3$
11	$aW\Delta T\|\Delta T\|$	$\sqrt{aW}W/W_z$	$aW(aM_z)$	$aW(aC_z)$
12				$\sqrt{aW}W/W_z$
13				$aWa\Delta T$

index	set5	set6	set7
1	aW	aW	aW
2	$(aW)^{3/2}$	$(aW)^{3/2}$	$(aW)^{3/2}$
3	$aW\Delta T$	$aW\Delta T$	$aW\Delta T$
4		$(aW)^2$	$(aW)^2$
5		$(aW)^{3/2}\Delta T$	$(aW)^{3/2}\Delta T$
6		$(aW)^3$	$(aW)^3$
7		aWa	aWa
8			aWW/W_z
9			$(aW)^{3/2}W/W_z$
10			$(aW)^{5/4}$
11			$(aW)^2W/W_z$
12			aWW
13			$(aW)^{7/4}$

has resulted a well-validated line-by-line model called LBLRTM [*Clough et al.*,1992; *Clough and Iacono*,1995; *Tuner et al.*,2004]. Thus, the latest version of AERI fast forward model was built using the LBLRTM v6.01 and CKD v2.4.

To generate the regression coefficients, the training dataset which includes 31 radiosonde-rocketsonde sets launced from the tropic and the Arctic, plus the 1976 U.S. Standard Atmosphere are selected to compute monochromatic optical depth on a fixed pressure grid. A weak-beer function $(1-(x/a)^2)^2$ is applied as IRF in Eq.(3.1.8), where a is half of maximum optical path difference of an equivalent interferometer, for AERI instrument, a=(1/0.4871)/2. These convolved and apodized transmittances

Table 3.4 Ozone predictors for SARTA model

index	set1	set2	set4	set5,6,7
1	aO	aO	aO	aO
2	$\sqrt{aO}$	$\sqrt{aO}$	$\sqrt{aO}$	
3	$aO\Delta T$	$aO\Delta T$	$aO\Delta T$	
4	$(aO)^2$	$(aO)^2$		
5	$\sqrt{AO}\Delta T$	$\sqrt{AO}\Delta T$		
6		aOO/O_x		
7		$\sqrt{aO}O/O_x$		
8		aOO_z/O_x		
9		$aO\sqrt{aO_x}$		
10		$aOaT_O$		

are then converted back into layer effective optical depths. Regressions are then used to relate these optical depths to the predictors in the Table(3.5). This process is performed for dry air(which includes all absorbing gases except water vapor and ozone), water vapor, and ozone and the regression coefficients are saved into binary coefficients files. The pressure coordination of AERI fast forward model covers the pressure altitude ranges from 1000 to 2 hPa ($\sim$ 35km). To capture the structure of planetary boundary layer, the grid interval below 900 hPa is 5 hPa, the grid interval for the middle of troposphere (600 - 900 hPa) is 20 hPa, and grid interval for upper troposphere (600 - 200) is 50 hPa, as the Table(3.6) shown.

Table 3.5 Predictors of AERI fast model

index	dry air	water vapor	ozone
1	ΔT	ΔT	ΔT
2	$(\Delta T)^2$	$2\cdot(\sum \Delta T\cdot\Delta p)/p_j^2$	$2\cdot(\sum \Delta T\cdot\Delta p)/p_j^2$
3	$(\sum \Delta T\cdot\Delta p)/p_j$	ΔW	ΔO
4	$(\sum \Delta T\cdot\Delta p\cdot p_j)$	$2\cdot(\sum \Delta W\cdot\Delta p\cdot p_j)$	$2\cdot(\sum \Delta O\cdot\Delta p\cdot p_j)$
5		$\Delta T\cdot\sqrt{\lvert\Delta p\cdot W_j\rvert}$	$\Delta T\cdot\sqrt{\lvert\Delta p\cdot O_j\rvert}$
6		$(\Delta T)^2\cdot\sqrt{\lvert\Delta p\cdot W_j\rvert}$	$(\Delta T)^2\cdot\sqrt{\lvert\Delta p\cdot O_j\rvert}$
7		$\Delta W\cdot\sqrt{\lvert\Delta p\cdot W_j\rvert}$	$\Delta O\cdot\sqrt{\lvert\Delta p\cdot O_j\rvert}$
8		$(\Delta W)^2\cdot\sqrt{\lvert\Delta p\cdot W_j\rvert}$	$(\Delta O)^2\cdot\sqrt{\lvert\Delta p\cdot O_j\rvert}$
9		$\Delta W\cdot\Delta T\cdot\sqrt{\lvert\Delta p\cdot W_j\rvert}$	$\Delta O\cdot\Delta T\cdot\sqrt{\lvert\Delta p\cdot O_j\rvert}$

The AERI predictor tables use the following notations:

ΔT : temperature difference $T_{prof} - T_{ref}$

ΔW : water vapor mixing ratio difference $W_{prof} - W_{ref}$

ΔO : ozone mixing ratio difference $O_{prof} - O_{ref}$

Δp : pressure difference $p(j-1) - p(j)$

Table 3.6 Pressure (hPa) grid of AERI fast model

2.0	3.0	4.0	5.0	7.0	10.0	15.0	20.0	25.0	30.0
50.0	75.0	100.0	125.0	150.0	175.0	200.0	250.0	300.0	350.0
400.0	450.0	500.0	550.0	600.0	620.0	640.0	660.0	680.0	700.0
720.0	740.0	760.0	780.0	800.0	820.0	840.0	860.0	880.0	900.0
905.0	910.0	915.0	920.0	925.0	930.0	935.0	940.0	945.0	950.0
955.0	960.0	965.0	970.0	975.0	980.0	985.0	990.0	995.0	1000.0

3.1.3 Principal Component Radiative Transfer Model (PCRTM)

PCA is a multivariate analysis method was first proposed by Pearson in 1901 and developed by Hotelling in 1933. It is commonly used to reduce the dimensionality of a data set with a large number of interdependent variables. This reduction can be obtained by finding a set of N_t orthogonal vectors in the input space of dimension of N_c, with $N_t < N_c$, these orthogonal vectors represent as much as possible of the data variances. Hence the problem of dimensionality reduction is one of finding a linear transformation from the N_c-dimensional input space to an N_t-dimensional subspace spanned by N_t orthogonal vectors which are referred as principal components (PCs). In the remote sensing, the data set $\mathbf{M}$ is form by N_c spectra and N_t channel frequency radiance. Then a singular value decomposition (SVD) is performed on the covariance matrix $C = M^T M$ of $\mathbf{M}$ and yields:

$$C = UDV^T, \tag{3.1.9}$$

where $\mathbf{D}$ is a diagonal matrix with the diagonal entries being the eigenvalues; and the columns of $\mathbf{U}$ are the eigenvectors or principal components (PC) of $\mathbf{C}$. The first PC generated by SVD represented an average channel spectrum. The second PC is

orthogonal to the first one and accounts for a major fraction of the variance in the data matrix. Each successive PC is responsible for a smaller fraction of the total variance in the data, only a few hundred PCs are needed to regenerate any spectrum in the data matrix. Once the PCs are generated, they are pre-stored in the forward model.

For high-resolution spectra, many channel have similar properties, i.e., the absorption lines have similar Lorentz or Doppler half-widths. Dependencies of the line intensity and half-width on atmospheric status are similar. The number of independent pieces of information is much less than the number of monochromatic radiances, thus, many radiative transfer calculation is redundant. By PCRTM, only couple hundreds monochromatic lines are selected to calculate radiance from given atmospheric status, then the relation between channel radiance and these monochromatic radiance with PC scores are obtained.

$$R^{ch} = \sum_{i=1}^{N_{PC}} Y_i U_i + \epsilon = \sum_{i=1}^{N_{PC}} (\sum_{j=1}^{N_{mono}} a_j R_j^{mono}) U_i + \epsilon. \tag{3.1.10}$$

In this equation, R^{ch} is the channel spectrum vector, U_i is the ith PC vector, N_{PC} is the number of significant PCs. Y_i is the PC score, which is generated by linearly combination monochromatic radiance R^{mono}, and a_j are the associated weights. The PC score (Y_i) is a dot product of PC vectors ($U^T_{N_{ch}X1}$) with the channel radiance vector ($R^{ch}_{N_{cn}X1}$),

$$Y_i = U^T_{N_{ch}X1} R^{ch}_{N_{ch}X1} = \sum_{j=1}^{N_{ch}} u(j,i) \times R^{ch}(j). \tag{3.1.11}$$

The index i represents the ith PC score, j represents the channel index, the superscript T stands for transpose, and $u(i,j)$ is an element of the PC matrix(U). In general, each channel radiance is the linear combination of the monochromatic radiances within the frequency span of that channel and the weighting functions which are normalized SRF at the monochromatic grid.

3.2 Inversion Theory

In his pioneering paper, King pointed out that the angular radiance distribution is the Laplace transform of the Planck intensity distribution as a function of the optical depth. On this basis, he first proposed the idea of inferring atmospheric state from satellite observation of infrared emission at different angles[King (1956)]. Kaplan advanced this conception by demonstrating that the vertical resolution of the atmospheric parameters field could be inferred from from the spectral distribution of atmospheric emission[Kaplan (1959)].

In order to determine the atmospheric temperature from the thermal emission measurement, the source of emission must be a relatively abundant gas of known with homogeneous distribution.

The main problem of inverting the radiative transfer equation to retrieve the state of atmosphere which produced the corresponding observation is that there is no unique solution for the detailed vertical profile of temperature or an absorbing constituent. Three reasons induces this problem : (1) The outgoing radiance arise from relatively deep layers of the atmosphere; (2) The radiances observed within various spectral channels come from overlapping layers of the atmosphere and are not vertically independent of each other; (3) Measurements of outgoing radiance possess errors. As a consequence, there are number of approaches to the profile retrieval problem[Fleming and Smith (1971); Fritz et al. (1972); Rodgers (1976); Twomey (1977)]. Rodgers presents a comprehensive tutorial on retrieval theory and outlines many of the various methods on approaching the under-determined, nonlinear problem of geophysical retrievals [Rodgers (2000)].

The general forward model equation mapping the atmospheric state into the measurement space (measured radiance spectrum) has the form [*Rogers*,2000]:

$$\mathbf{Y} = \mathbf{F(X)} + \epsilon, \tag{3.2.1}$$

where $\mathbf{Y}$ is the measurement vector with N observed radiances or brightness temperatue, $\mathbf{F(x)}$ is the forward model operator for a given vector $\mathbf{x}$, the vector $\mathbf{x}$ contains L (levels of pressure) atmospheric temperature, L atmospheric water mixing radios etc., and ϵ is the measurement error. The measurement error is combined by the terms of systematic biases and random noise. The linearization form of Eq.(3.2.1) is

$$\delta\mathbf{Y} = H'\delta\mathbf{X} \tag{3.2.2}$$

where H' is the linear tangent model of the forward model F e.g. $\partial F/\partial\mathbf{X}$. The derision of this perturbation form can be seen in appendix. The linear model can be obtained by numerical perturbation, or an approximated analytical form [Li (1994)] can be used. Unfortunately, this equation cannot be solved directly because of the near-singularity of the weighting function matrix H'. Many studies pointed out that the solution is unstable because the equation is under-constrained. Furthermore, the instability of this solution may also be caused by the the errors arising from the numerical quadrature used for the calculation of H'.

3.2.1 Statistical Retrieval

The most straightforward approach to solving the retrieval problem (i.e., the solution of Eq.(3.2.1) is applying large quantity of the atmospheric state data already compiled through radiosonde or numerical forecast. If by one or more of these methods, one were to make measurements that are coincident in space and time with satellite or ground measurements, the problem could be solved by regression techniques.

Given a statistical ensemble with K pairs of observed radiance R which have M channels and corresponding atmospheric profiles B which have N elements, we define the matrix

$$R'(i,k) = R(i,j) - \bar{R}(i)$$
$$q'(j,k) = B(j,k) - \bar{B}(j)$$
$$i = 1,\ldots,M; k = 1,\ldots,K; j = 1,\ldots,N; \tag{3.2.3}$$

where $\bar{q}$ represents the mean profile of atmospheric ensemble, and $\bar{R}$ represent the mean spectra of radiance ensemble.

The regression problem is to find a $N \times M$ matrix C which fits the relationship $B = CR$ in the sense of least squares, or to determine the C that minimizes the square of the Euclidean distance

$$\rho(C) = \sum_{j,k=1}^{N,K} (q'(j,k) - \sum_{i=1}^{M} C(j,i)R'(i,k))^2$$
$$= tr\{(q' - CR')(q' - CR')^T\}, \tag{3.2.4}$$

where tr represents the trace of the matrix and superscript T denotes the matrix transpose.

By differentiating this equation with respect to the element of the matrix C, the solution of C can be obtained,

$$\frac{d\rho}{dC} = 2q'R'^T - 2CR'R'^T = 0$$
$$or$$
$$C = q'R^T(R'R'^T)^{-1}. \tag{3.2.5}$$

Now any particular solution can be obtained from the equation **q=Cr**.

The advantage of the least square regression method are obvious: the knowledge of the weighting functions or the observation errors are not required in the retrieval which is comparing the radiance and radiosonde data to the statistical ensemble; the instrument need not be calibrated in an absolute sense, and the regression is numerically stable.

The shortcomings of the least square regression method include: (a)it disregards the physical properties of the radiative transfer model that the solution is linear whereas the exact solution is non-linear because the weighting function and consequently the solution coefficients **C** are functions of temperature or water vapor mixing

ratio;(b) the solution uses the same operator matrix for a range of radiance depending upon how the sample is stratified, and thus the solution coefficients are not situation dependent; and (c) radiosonde data is required.

To overcome the shortcomings of the least square regression method, the constrained linear inversion which the instrumental errors are taken into retrieval is introduced. The measured radiance contain errors due to instrumental noise and biases as the following equation:

$$r_i^{meas} = r_i^{true} + \epsilon_i, \tag{3.2.6}$$

where ϵ_i represents the measurement errors. Within the measurement error, the solution $\mathbf{q(p)}$ is not unique. To determine the best solution, constrain the following function to be a minimum:

$$\sum_{\imath=1}^{M} \epsilon_i^2 + \gamma \sum_{k=1}^{K} (q_k - q^{mean})^2 \tag{3.2.7}$$

where γ is a smoothing coefficient which determines how strongly the solution is constrained to be near the mean. A least squares solution with quadratic constraints implies

$$\frac{\partial}{\partial q_j}[\sum_{i=1}^{M} \epsilon_\lambda^2 + \gamma \sum_{k=1}^{K} (q_k - q^{mean})^2] = 0 \tag{3.2.8}$$

with

$$\epsilon_i = \sum_{j=1}^{N} C_{ij} q_j - r_i^{true}$$

, the equation leads to

$$\sum_{i=1}^{M} [\sum_{k=1}^{K} C_{ij} q_k - r_i^{true}] C_{ij} + \gamma [q_k - q^{mean}] = 0. \tag{3.2.9}$$

By definition

$$q^{mean} = \frac{1}{K}\sum_{k=1}^{K} q_k,$$

and

$$q_k - q^{mean} = -K^{-1}q_1 - K^{-1}q_2 - \ldots + (1 - K^{-1})q_k - \ldots - K^{-1}q_K,$$

the constrained least squares solution can be written in matrix form

$$C^T Cq - C^T r + \gamma Mq = 0, \tag{3.2.10}$$

where $\mathbf{M}$ is the matrix of

$$M = \begin{pmatrix} 1-K^{-1} & -K^{-1} & 0 & \cdots \\ -K^{-1} & 1-K^{-1} & 0 & \cdots \\ -K^{-1} & -K^{-1} & 1-K^{-1} & \cdots \\ \vdots & \vdots & \ddots & \vdots \\ -K^{-1} & -K^{-1} & \cdots & 1-K^{-1} \end{pmatrix}$$

which become the identity matrix as $\mathbf{K}$ approach ∞. Thus the solution has the form

$$q = (C^T C + \gamma M)^{-1} C^T r. \tag{3.2.11}$$

Thus, the statistical sounding retrieval algorithm has the form:

$$q_{ret} = q_0 + (r_m - r_0)C \tag{3.2.12}$$

where the vector q_{ret} represents the retrieval atmospheric profiles of temperature, water vapor, or other trace gases, q_0 represents the priori profiles, r_m is the radiance measurements from IASI or AERI instrument, r_0 is the simulated radiance corresponding priori profiles. The matrix $\boldsymbol{C}$ is a statistical coefficient matrix computed from atmospheric profile and corresponding simulated radiance spectra deviations from an ensemble means, $\overline{q}$ and $\overline{r}$ respectively. This statistical coefficient matrix, $\boldsymbol{C}$,

is given by,

$$C = (R'^T \cdot R' + \lambda E^T \cdot E)^{-1} \cdot R'^T \cdot Q' \tag{3.2.13}$$

where the matrices Q and R are climatological ensembles of atmospheric profiles and associated simulated radiance spectra. The prime symbol represents a deviation from the priori conditions q_0 and r_0,e.g.,

$$\begin{aligned} R'(i,j) &= R(i,j) - r_0(j) \\ Q'(i,k) &= Q(i,k) - q_0(k) \end{aligned} \tag{3.2.14}$$

$E^T \cdot E$ is a statistical covariance of spectral radiance noise.

3.2.2 Physical Retrieval

To solve the inverse problems associated with equation(3.2.1), i.e., the retrieval of temperature and humidity profiles $\mathbf{x}$ from radiance measurements, $\mathbf{y}$, the numerical perturbation form of radiative transfer model is used (The derivative this perturbation form are shown in Appendix A):

$$\delta Y_j = \sum_{i=1}^{l_s} \delta T(i) K_T(i,j) + \sum_{i=1}^{l_s} \delta q(i) K_q(i,j), \tag{3.2.15}$$

where the perturbation δ is with respect to an *a-priori* estimated or mean condition. Y is the measured radiance spectrum vector; and K_T, K_q are the weighting functions of atmospheric temperature and water vapor, respectively.

Assuming the measurement error and the atmospheric estimation error is following Gaussian distribution, the probability distribution function (*pdf*) of radiance measurement can be written as

$$-2\ln(P(y|x)) = [y^m - F(x)]^T S_\epsilon^{-1} [y^m - F(x)] + c_1, \tag{3.2.16}$$

where $P(y|x)$ is the conditional *pdf* of y given x, c_1 is a constant, and S_ϵ is the measurement error covariance. Also, we can describe prior knowledge of $\mathbf{x}$ by a

Gaussian possibility distribution function:

$$-2\ln(P(x)) = [x - x_a]^T S_a^{-1}[x - x_a] + c_2, \tag{3.2.17}$$

where $P(x)$ is the priori *pdf* of state $\mathbf{x}$, x_a is the *a-priori* value of $\mathbf{x}$, and S_a is the associated covariance matrix $S_a = \varepsilon\{(x - x_a)(x - x_a)^T\}$. From the Bayes' theorem which provides the relationship between the two different conditional *pdf*'s, the conditional *pdf* of x given y, $P(x|y)$ can be obtained by:

$$P(x|y) = \frac{P(y|x)P(x)}{P(y)}, \tag{3.2.18}$$

where P(y) is the priori *pdf* of the measurement with a similar meaning, in practice it is only a normalising factor, and it is often not needed. In the inversion theory, $P(x|y)$ is the posterior *pdf* of the state when the measurement is given. Using the definitions of P(x) and $P(y|x)$ into Bayes' theorem, we obtain the posterior *pdf*:

$$-2\ln P(x|y) = [y^m - F(x)]^T S_\epsilon^{-1}[y^m - F(x)] + [x - x_a]^T S_a^{-1}[x - x_a] + c_3, \tag{3.2.19}$$

The first two items of right hand side of this equation is called a "cost" function $J(x)$ [Eyre (1989)]. Our inversion task can be considered to find the best estimate $\mathbf{x}$ and an error characteristic that describes this *pdf* well enough for practical purpose.

To find the maxima probability state $\mathbf{x}$, we set the derivative of Eq.(3.2.19) equal to zero:

$$\nabla_x\{-2\ln(P(x|y))\} = -[\nabla_x F(x)]^T S_\epsilon^{-1}[y^m - F(x)] + S_a^{-1}[x - x_a] = 0. \tag{3.2.20}$$

The gradient ∇_x of a vector-valued function is a matrix-valued function. Use matrix $K_j(x_i)$ to replace $\nabla_x F(x)$, the Eq.(3.2.20) change to:

$$-K^T(x)S_\epsilon^{-1}[y - F(x)] + S_a^{-1}(x - x_a) = 0 \tag{3.2.21}$$

To solve the general problem $x : g(x) = 0$ numerically, Newtonian iteration gives a way of

$$\begin{aligned} x_{i+1} &= x_n - \frac{g(x_n)}{g'(x_n)}, \\ x_{i+1} &= x_n - [\nabla_x g(x_i)]^{-1} g(x_i). \end{aligned} \tag{3.2.22}$$

Apply the $g(x) = \nabla_x J(x)$ into Newtonian iteration, we get

$$x_{n+1} = x_n - [\nabla^2 J(x_n)]^{-1} \nabla J(x_n). \tag{3.2.23}$$

This equation is known as inverse Hessian method.

The non-linear algorithm incorporates this inverse Hessian method and the steepest descent method of solution,

$$x_{n+1} = x_n - \gamma^{-1} \nabla J(x_n), \tag{3.2.24}$$

to control the convergence process. The combined solution can be written as

$$x_{n+1} = x_n - [\nabla^2 J(x_n) + \gamma I]^{-1} \nabla J(x_n), \tag{3.2.25}$$

which is called Levenberg-Marquardt method. This method is an improvement over Newtonian iteration when the *a-priori* s far from the solution.

The derivative of cost function $\nabla J(x)$ can be written as

$$\nabla J(x) = 2S_a^{-1}(x - x_a) - 2K^T(x) S_\epsilon K(x), \tag{3.2.26}$$

and the second derivative of cost function $\nabla^2 J(x)$ can be written as

$$\nabla^2 J(x) = 2S_a^{-1} + 2K^T(x)S_\epsilon K(x), \tag{3.2.27}$$

assuming we ignore the derivative of the weighting function. Substituting Eq.(3.2.26) and Eq.(3.2.27) into Eq.(3.2.25) yields

$$X_{i+1} = X_0 + S_i K_i^T S_\epsilon^{-1}[(Y^m - Y(x_i)) + K_i(X_i - X_0], \tag{3.2.28}$$

where the subscript i is the iteration index. $X_{i/i+1}$ and X_0 are the iterated and *a-priori* state vectors, respectively ($\mathbf{T}$, ln$\mathbf{q}$ combined in one state vector), and the S_i is the retrieval error covariance matrix, defined by:

$$S_i = [S_a^{-1} + K_i^T S_\epsilon^{-1} K_i]^{-1}. \tag{3.2.29}$$

Here S_a is an *a-priori* matrix that constrains the solution. S_{ap} can be the inverse of the *a-priori* first-guess error covariance matrix or another type of matrix. However, the *a-priori* can not be estimated easily. Here we let S_{ap}=λH in Eq.(3.2.28), where λ is a Lagrangian multiplier that serves as a smoothing factor. The optimazation scheme expressed by equation (3.2.28) is usually termed the Gauss-Newton method and provides a reliable maximum *a posteriori* estimate for "small residual" inverse problem as the one dealt with here. The solution X_i is highly depended on the smoothing factor λ which is difficult to determine. Different λ result in quite different solutions,e.g., the solution could be overconstrained and large biases can be created in the retrieval when λ is too large; the solution could be underconstrained and possibly unstable when the λ is too small. Therefore Eq.(3.2.28) is not a closed equation [Li and Huang (1999)]. It is noted that the determination of proper λ is effected by

the observation radiance itself, the observation errors, and the *a-priori* profiles of retrieval, often it is chosen empirically[Hayden (1988)].

Since the strong dependence of the retrieved state on the *a-priori* due to the ill-posedness of the sounding problem, the *a-priori* is still well reflected in the retrieved state after applying a simple physical retrieval. Most physical retrievals are confined to rather close regions around the *a-priori*. Another disadvantage of the physical retrieval is the necessity of calculating the weighting functions explicitly. Usually a numerical perturbation of the forward model is implied as weighting function, the related numerical residual errors may induce a severe deterioration of the retrieval accuracy.

For the inversion from ground based measurement, the weighting functions decrease exponentially with increasing altitude as figure(1.4) shows, with the rate dependent on the strength of the absorption. This means that the radiance signal are dominated by contributions from near the surface with rapidly decreasing sensitivity to the atmosphere with altitude. This altitude sensitivity characteristic leads to computational instability because of the strong correlation of the weighting functions among different spectral channels.

CHAPTER 4

DATA AND METHODOLOGY

4.1 Data

Four data sets are selected for this research. Each data set contains radiosondes, radiance spectra measured by ground based spectrometer, and matchup IASI spectra for the retrieval. These four observation locations represents 4 different geographical and climatological types: dessert with high altitude (Nevada) in spring season, southern grand plain (DoE ARM SGP site, Lamont) in fall season, east coast maritime (Hampton) in spring and summer season, and Atlantic tropical ocean in summer season.

In this research, not every radiosonde is matched to an IASI field of view (FOV), to provide the consistency between the IASI measurements and the in-situ measurements. The following criteria was used to obtain "coincident" in-situ measurement and IASI measurements FOV : The temporal and spacial difference between IASI overpasses and radiosonde launches must be smaller than one hour, and the distance between in-situ location and the nearest IASI footprint is less than 150 kilometers.

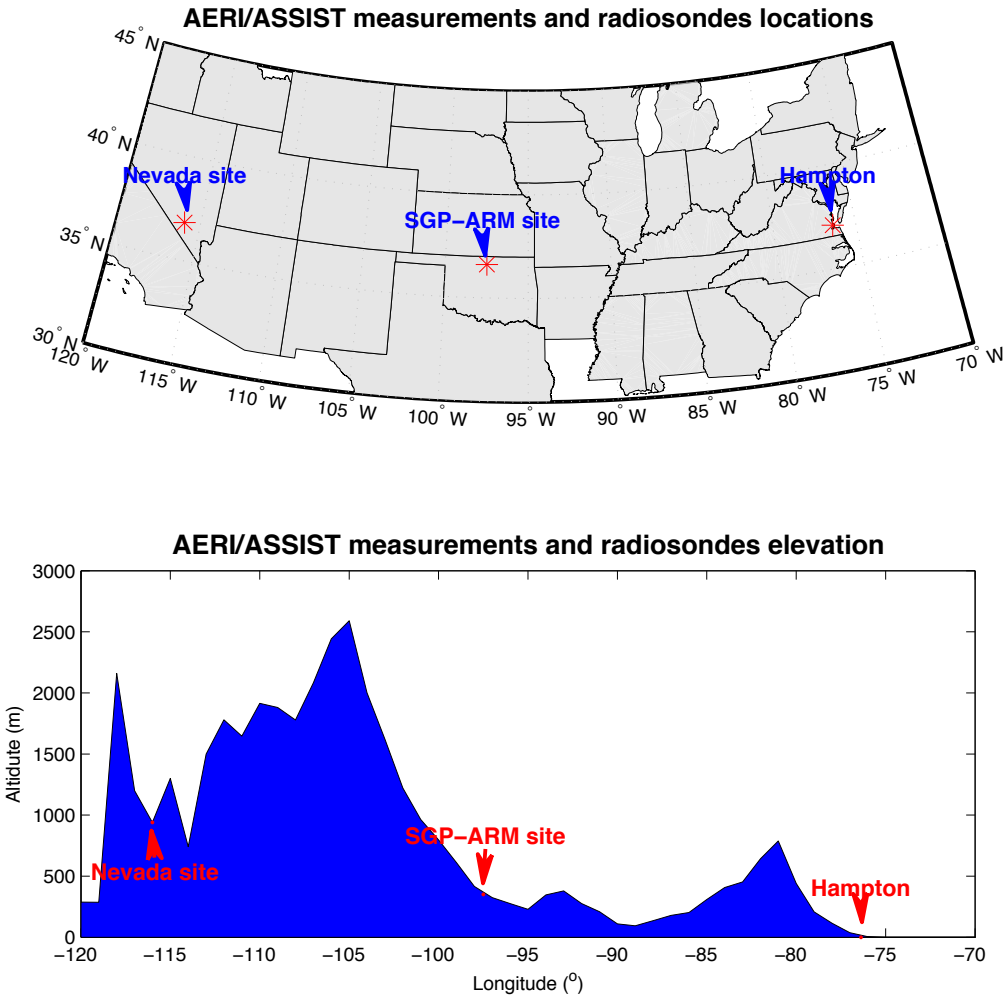

Figure 4.1 Geography of Nevada site, ARM SGP site, and Hampton,VA

4.1.1 Data for Nevada and Hampton case

ASSIST data was collected as part of a DOE NNSA ground truth operation and measurement program conducted during April and May 2010. The collection took place at Trailer Park 3 located at NPTec on the Nevada Test Site (NTS). ASSIST downwelling radiance data was collected on April 15, 19, and 20-23, May 9-10, 12, 14, 17-18, 20-21 and 23-26 totaling over 95 hours of data at an approximately 3 minute collection rate. During these days, 14 of total 24 radiosondes have match-up with the IASI FOVs as defined by the criteria provided earlier.

During August 2009, the NASA Langley Research Center (LaRC) in Hampton VA conducted a chemistry ground truth validation experiment (GeoCape) in which the AERI instrument was brought to the NASA site by the University of Wisconsin. The DOE and HU were invited to participate with the ASSIST instrument, which once again provided an opportunity for a direct comparison of the ASSIST measurements with the AERI. During this experiment, the AERI instrument collected the downwelling radiance spectra on August 4-7, and 10-12. In the experiment, 5 ozonesondes and 6 radiosondes were launched. Among them, there were 6 ozone/radiosondes that fit the IASI match-up criteria.

The Chemistry and Physics Atmospheric Boundary Layer Experiment (CAPBLE) was held during 21st June - 6th August, 2010 at NASA Langley Research Center in Hampton, Virginia. ASSIST was deployed in this field study for running approximate 276 hours and collecting 5718 downwelling radiance spectra. That period coincided with 23 IASI overpasses and 20 AIRS overpasses. Fifteen ozone sondes and 34 radiosondes were launched for validation of atmospheric temperature, water vapor, ozone, and other trace gases profiling. Excluding the cloudy cases, there were 8 radiosondes which satisfied the IASI match-up criteria and thus could be used for validating the IASI retrieval.

The Hampton University Ground-based Remote Atmospheric Sounding Project (HUGRASP) experiment was held during 19th April - 30th, 2012. During this experiment, 25 radiosondes had been launched, and ASSIST collected 132-hour downwelling radiance spectra. Among them, 7 radiosondes which have match-up IASI spectra can be used for the retrieval of clear sky.

4.1.2 ARM SGP site data

The Southern Great Plains (SGP) site was the first field measurement site established by DOE's Atmospheric Radiation Measurement (ARM) Program. The SGP

was chosen as the first ARM field measurement site for several reasons including its relatively homogeneous geography and easy accessibility, wide variability of climate cloud type and surface flux properties, and large seasonal variation in temperature and specific humidity. It also already had a large, existing network of weather and climate research and instrumentation. Scientists are using the information obtained from the SGP to improve cloud and radiative models and parameterizations and, thereby, the performance of atmospheric general circulation models used for climate research.

The routing balloon launch time of the ARM SGP CART site is at about 05:30Z, 11:30Z, 17:30Z, and 23:30Z each day, meanwhile the Metop satellite overpasses the SGP CART site at around 01:30Z-3:30Z and 16:00Z-18:00Z, thus the balloon launch at 17:30Z could match up the IASI daytime overpass. For this site, the cloudy cases can be filtered using the on site lidar data, and the cases which a time difference between balloon launch and IASI overpass is more than 1 hour were also filtered. Even though, there is abundant number of cases to fit our match-up criteria, for instance, for the fall season (September, October, and November) of year 2010, 40 cases could be used for this retrieval research study.

4.1.3 AEROSE data

The Aerosol and Ocean Science Expeditions (AEROSE) is a series of intensive field experiments conducted onboard the U.S. National Oceanic and Atmospheric Administrations (NOAA) ship Ronald H. Brown [Morris et al., 2006]. The primary goal of AEROSE is to characterize the atmospheric and oceanic impacts, as well as the chemical, microphysical, and biological evolution of Saharan and sub-Saharan aerosols and air masses during trans-Atlantic transport. Each AEROSE research mission is supplied with radiosondes and ozonesondes to support satellite validation of low earth orbit (LEO) passive sounders, specifically AIRS and IASI [Nalli, et al., 2011].

Each radiosonde is launched approximately 0.5 hours before a predicted overpass of Aqua or Metop while each ozonesonde is released approximately an hour before a predicted satellite overpass. Approximately three radiosondes and one ozonesonde are launched per day. These radiosondes include thermodynamic measurements of temperature, pressure, and relative humidity (RH), (collectively referred to as "PTU). RS92 sondes provide vertical wind profiles of wind speed and direction via a Global Positioning System (GPS). Vaisala RS92 sondes also provide geometric heights of each measurement level which may be of great value for the validation of satellite derived pressure as a function of altitude level because GPS heights are obtained independently of the pressure sensor. Radiosondes typically provide PTU soundings through the upper troposphere and sometimes the extreme lower stratosphere while ozonesondes provide ozone profiles through the lower stratosphere.

In this research, since the M-AERI data in 2009 and 2010 were not reliable because of a calibration issue, it was decided to chose the observation data in 2008 for this study. In the AEROSE2008, there were total over 70 radiosondes and ozonesondes during May 2008, and 18 radiosonde tha fit the IASI matchup criteria we discussed earlier. Locations of these 18 radiosondes and locationsof 4 nearest coincident IASI footprints for each radiosonde are shown in Figure 4.2.

Table 4.1 Characteristics of sounding data

Data Name	Location	Elevation(m)	Time	Number of sounding	RAOB ensemble
GeoCape	76.38W, 37.08N	5	Aug.,2009	6	Wallops Is.
CAPBLE	76.38W, 37.08N	5	June-July,2010	8	Wallops Is.
HUGRASP	76.34W, 37.02N	3	April,2012	7	Wallops Is.
Nevada	115.96W, 36.81N	940	April-May,2010	14	Mercury Station
ARM-SGP	97.49W, 36.61N	316	Sep.-Nov.,2010	40	Lamont Station
AEROSE08	South Atlantic	0	May,2008	15	GFS data

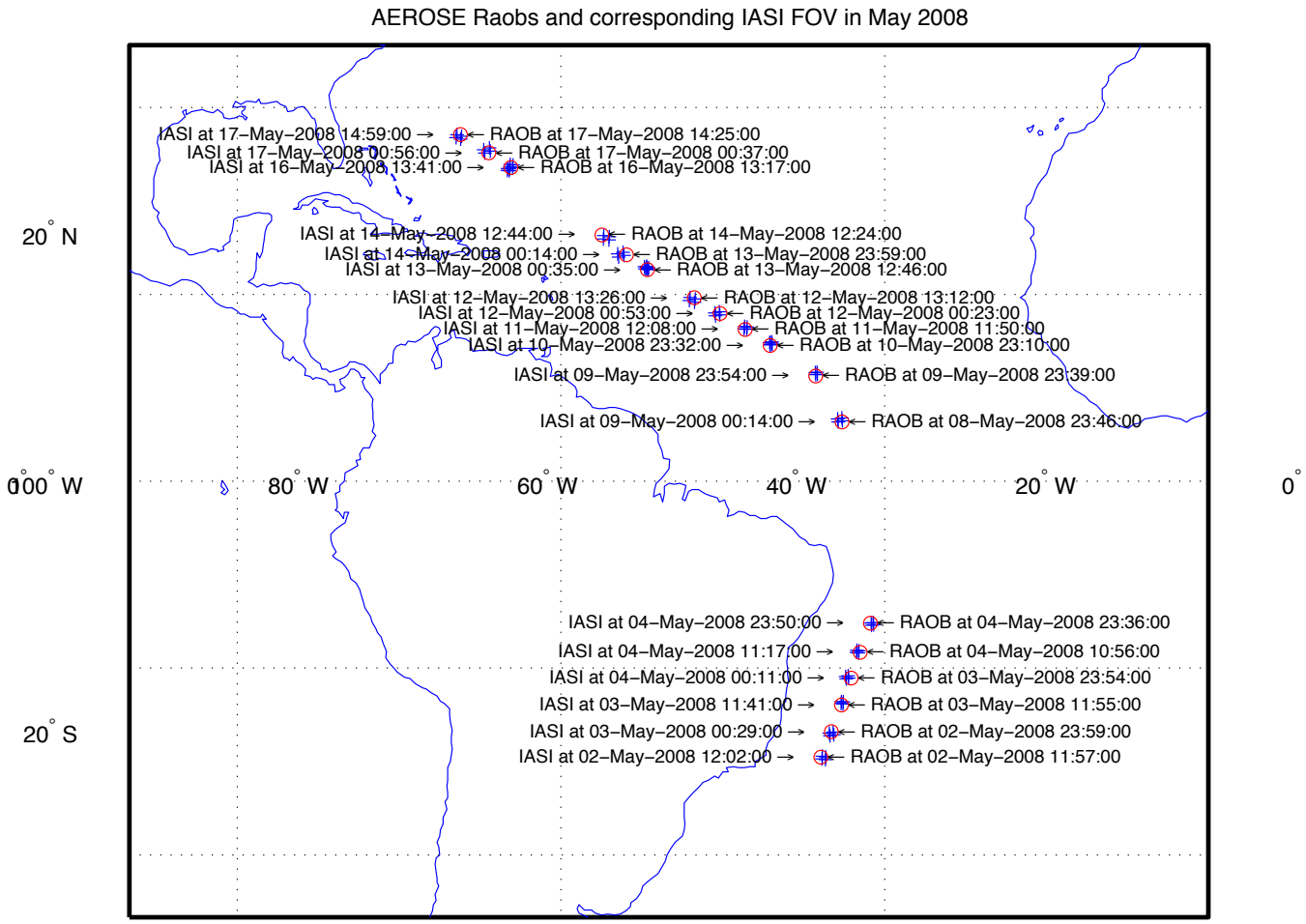

Figure 4.2 Locations of RAOBs and corresponding IASI FOV in AEROSE 2008. Circles are the locations of RAOB, crosses are the nearest 4 IASI footprints

4.1.4 Auxiliary Data

The purpose of this research is to demonstrate the advantage of combined retrieval for clear sky case. Though radiosondes provide the vertical distribution of atmospheric relative humidity, it is very hard to distinguish the cloud from only the relative humidity profile. Other data can be used to determine if it is cloudy above the in-situ location at the time the IASI overpass.

Accompanying with IASI, the Advanced Very High Resolution Radiometer (AVHRR) is mounted on the Metop thus it scan the same area as IASI does . This radiometer provides infrared and visible images at 1 km horizontal resolution. The brightness

temperature at channel 4 (10.3-11.3 μm) and channel 5 (11.5-12.5 μm) and the solar reflectance channel 1 (0.58-0.68 μm) can be used to determine if the scene is cloudy.

As discussed in previous chapter, the retrieval result dependeds on an initial profiles. Although a statistical profile can be used in the retrieval, a good *a-priori* profile will improve the accuracy and computing efficiency of the retrieval. For the cases of Nevada, SGP ARM, and Hampton, NOAA Rapid Update Circle(RUC)[Benjamin et al. (1994, 2004)] profile data with a grid domain covering the north America are chosen for the *a-priori* of retrieval. The RUC model assimilates in-situ data from radiosondes and aircraft temperature reports, as well as remotely sensed data such as PWV and cloud top pressure from GOES. Compared with other reanalysis/forecast data sets, RUC has two advantage: very high horizontal resolution of $\sim$13 km and it is run at hourly interval while the others NWP data sets, such as North America Mesoscale Forecast System (NAM), are 4 times daily. The middle and upper tropospheric section of RUC profiles are quite accurate, while at the lowest section, the RUC data can not portrait the thermodynamic characteristics of the boundary layer. Still, the RUC output is an optimal source of middle and upper tropospheric information for use as the retrieval initial profile.

For the case of AEROSE2008, all the observation occurred in the tropical Atlantic ocean which is outside the RUC domain. In that region, the spatial and temporal variation of temperature and water vapor in middle and upper troposphere is relative small if there is no strong convection occuring. The NOAA Global Forecast System (GFS) reanalysis data was selected to construct a statistical ensemble for the retrieval process using for its $1^o \times 1^o$ horizontal resolution and 4 time daily output.

4.2 LBL-fast model and Principal Component Analysis

As the previous chapter described, the vertical resolution for AERI fast forward model below the 900 hPa is very high (5 hPa interval), but above 900 hPa, the vertical

resolution drops off with increasing altitude to 20 hPa. This coarse resolution would affect the simulation accuracy of fast forward model if the height of observation is above 900 hPa (cases of Nevada). Furthermore, one can not resolve the subtle boundary structure of a mountainous or plateau region if this fast forward model is applied in the retrieval procedure directly. For the observation location where surface pressure is larger than 1000 hPa (cases of Hampton and cases of AEROSE), the profiles grids have to normalized to the AERI fast forward model pressure grids, this adjusting will affect the simulation accuracy. On other hand, the accuracy of LBLRTM calculation would not be affected by altitude of the ground instrument, since the actual surface pressure can be used in an LBLRTM calculation.

To overcome the topographic effect on the AERI fast forward model, the Principal Component Analysis (PCA) was introduced to improve the original fast model. In the practice, we need create a statistical ensemble for the observation location, e.g., collect 3-year radiosonde data from meteorological station which is closest to the observation site. Then the radiance spectrum for each profile of the data set was calculated using the AERI fast model and LBLRTM separately. Prior to the AERI fast model calculation, the pressure of the profile is normalized to AERI fix pressure grid. With these two spectrum data sets, the covariance matrix of difference between LBLRTM and AERIFFM can be generated. Using the PCA, a correction matrix was calculated for the AERI fast forward model. In the final radiance simulation, the radiance spectrum of AERI fast forward model was corrected using this correction matrix. After this correction, the output radiance spectrum matches the corresponding LBLRTM spectrum very well. Through this modification, high vertical resolution for boundary layer features using the AERI fast forward model for the retrieval, can be retained in mountainous or plateau region. The accuracy of LBLRTM and efficiency of AERI fast forward model can be retained in this new radiative transfer model approach.

For this research, the radiosonde data of Mercury station (116.02^{o}W, 36.62^{o}N, 1007 m), Wollops Islands station (75.48^{o}W, 37.93^{o}N, 14 m) were selected for the Nevada (115.92^o, 36.81^o, 940 m) and Hampton (76.39^{o}W, 37.10^{o}N,3 m) cases respectively. The radiosonde data of Lamont station which is located at ARM-SGP cart site is selected for the ARM-SGP case For the cases of AEROSE, since there is no constant radiosondes observation in the tropic Atlantic ocean, the reanalysis data of Global Forecasting System (GFS) with in experimental region was selected to set up statistical ensemble.

4.2.1 Validation of LBL-fast model

The LBLRTM has been well validated for IASI spectra during Sodankylä campaign in 2010[Calbet et al. (2011)]. The result of this campaign indicate that the LBLRTM can reproduce IASI measurement to within the accuracy of one sigma instrumental noise with adequate radiosonde measurements. Also, the validation of SARTA fast forward model for the IASI and AIRS spectra shows that simulation can achieve a very high accuracy, on the order of the instrumental noise [Strow et al. (2006, 2008)]. Thus, we can apply the LBLRTM and SARTA model in our retrieval procedures. It is necessary to validate the AERI-LBL radiative transfer model before we apply this model for simulating the AERI measurements in the retrieval process.

Figure(4.3) shows the mean and standard deviation of difference between the LBLRTM simulation and corresponding simulation of AERI fast forward model and simulation of LBL-AERI model for the statistical ensemble of profiles which include 211 radiosondes from the Mercury weather station which is 950 m high, 2000 GFS re-analysis data of tropical ocean, and the 235 radiosondes from the Lamont DoE CART site which is 316m high. Comparing the simulation of AERI fast forward model, the LBL-AERI model improves the simulation dramatically for the profiles

at high altitude observation site. Furthermore, for the observations near sea surface, where the surface pressure is about 1010 mbar, the improvement is also significant.

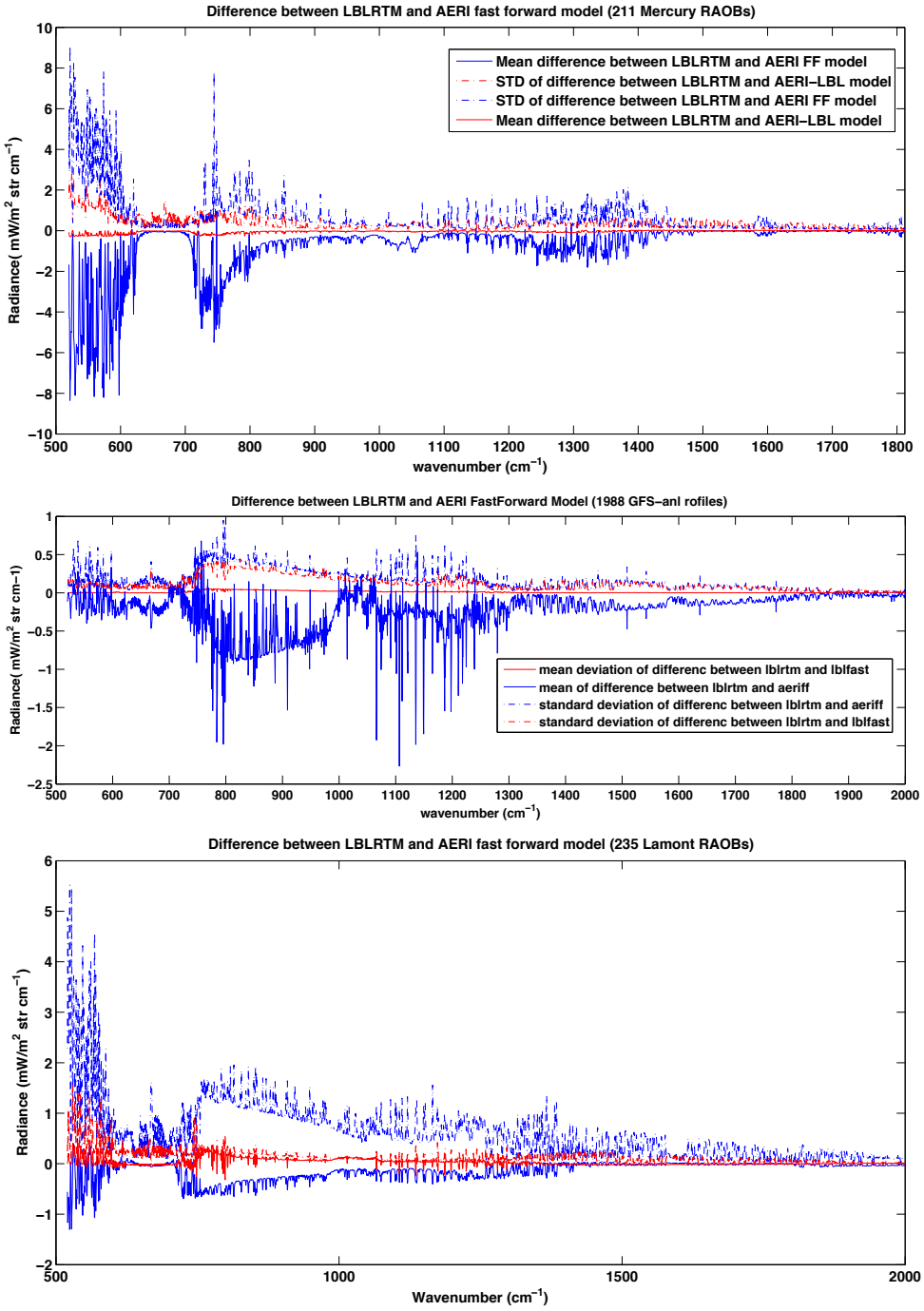

Figure 4.3 Mean and standard deviation of difference between LBLRTM and AERI fast models, upper plot shows the high altitude observation scenario, lower plot shows the sea surface observation scenario.

For the water vapor region within 520-620 cm^{-1}, systematic bias between the AERI fast forward model and LBLRTM can reach more than 8 mW with variance of 6 mW for the worst scenario, meanwhile, the systematic bias between LBL-AERI and LBLRTM is no more than 0.2 mW with variance of 2 mW in this region. For the opaque region within 620-700 cm^{-1}, The absorption in the window regions between 800 and 1200 cm^{-1} is primarily due to water vapor absorption and water vapor self-continuum.

4.3 Surface Emissivity and Temperature Calculation

For the upwelling radiative transfer model, even the contribution of ground surface (the first and the third items of left side of Eq.(3.1.1) is relatively small, it affects the accuracy of radiance simulation significantly in the windows region (800 - 1200 cm^{-1}), especially for the Nevada where dry air makes the transmittance of window region as high as 0.9 and the difference of ground skin temperature and air temperature may be more than 10 K. This simulation error of upwelling radiance will deteriorate the retrieval result at low level. Thus before the retrieval starts, it is necessary to determine proper surface temperature and emissivity, which is function of wavelength and view zenith angle.

The observation of M-AERI provided one solution of this issue [Smith et al. (1996)]. The zenith view angle of M-AERI can be switched, thus M-AERI can measure the radiance in upward and downward directions within a short time period. Then the sea surface temperature and emissivity can be calculated from these two radiance spectrum measurements. Walden et. al. also applied this method to determine surface temperature and spectral emissivity for the Antarctic scenario[Walden et al. (2006)].

From the definition of RTM, if we use satellite measurement(i.e., IASI or AIRS) to replace the left item of the Eq.(3.1.1), the ground measurement to replace the

downwelling term $\int_{P_{TOA}}^{P_S} B(\nu,T)d\tau_\nu^*$, thus, Eq.(3.1.1) can be simplified as

$$R_\nu^{IASI}(\theta) = \epsilon_\nu B_\nu(T_s)\tau_s + \int_{P_{TOA}}^{P_S} B(\nu,T)d\tau_\nu^{\uparrow}(P) + \tau_s(1-\epsilon_\nu)R_\nu^{AERI}F(\theta), \qquad (4.3.1)$$

where $R_\nu^{IASI}(\theta)$ is the satellite measurement (IASI) at zenith angle θ, R_ν^{AERI} is measurement of the up-looking ground spectrometers (AERI, ASSIST, or M-AERI) for the zenith direction angle, $F(\theta)$ is a geometry factor. Then the spectral emissivity can be written as function of measurements of up/downwelling radiance ($R_\nu^{IASI}(\theta)$, R_ν^{AERI}), surface temperature (T_s), total transmittance of atmosphere (τ_s) and total upwelling radiance of atmosphere itself. The last two items can be calculate from the RTM:

$$\epsilon_\nu = 1 - \frac{R_\nu^{IASI}(\theta) - \int_{P_{TOA}}^{P_S} B_\nu(T_p)d\tau_\nu^{\uparrow}}{\tau_s(R_\nu^{AERI}F(\theta) - B\nu(T_s))}. \qquad (4.3.2)$$

The two prerequisites of solving this equation are (1). the total transmittances τ_s is relatively large, otherwise the errors induced by calculation of upwelling atmospheric radiance will be magnified; (2). the atmospheric parameters in the calculation should be close to the real atmospheric state. For the window region (750-1150 cm^{-1}), the spectral total transmittances are generally larger than 0.5 except at ozone absorption region (950-1050 cm^{-1}) or for some strong water vapor absorption lines. Also within window region, the spectral upwelling atmospheric radiances are mainly contributed by low level atmosphere which can be retrieved precisely from measurements of ground based spectrometers.

Even when these two conditions are satisfied, the Eq.(4.3.2) which has two unknown variables (emissivity ϵ and surface temperature T_s) can not be solved explicitly. From physics point of view, unlike the transmittance spectrum which has lots of absorption lines, the emissivity spectrum of surface should be continuous, e.g., proper surface temperature couples with smoothest emissivity spectrum[Bower (2001)]. If surface temperature is too high, there would be deep gaps in the emissivity spectrum

while if the surface temperature is too low, there would be prelude peaks in the emissivity spectrum. In practice, a set of emissivity spectrum is calculated by adjusting the surface temperatures until find the spectrum which has the minimum variance of derivatives ($\partial\epsilon/\partial\nu$). The temperature corresponding to this minimum is the surface skin temperature. Figure(4.4) provides an example of the surface emissivity calculation from the simulated upwelling and downwelling radiance. The solid line is the preset artificial emissivity spectrum, while the dashed lines are the calculated emissivity spectra for varied skin temperature. The spectra with the region of 975 - 1075 cm^{-1} in this figure are ignored since this region is the strong ozone absorption region. The purple dashed line in this plot is the smoothest dashed lines and matches the target spectra better than the other lines. Also the difference between corresponding skin temperature for this purple line and the preset skin temperature is no more than 0.2 K. It should be noticeable that this example is under the most ideal conditions, for the real radiance observation, the result of emissivity calculation would be much worse than this example.

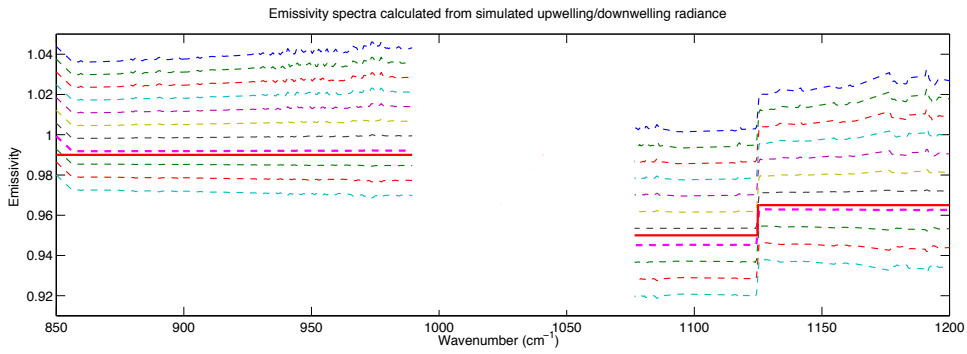

Figure 4.4 An example for the surface emissivity calculation. The solid line is the preset artificial emissivity spectrum, the dashed lines are the calculated emissivity spectra for varied skin temperature

4.4 Retrieval Procedure

In theory, physical retrieval that incorporates a profile covariance matrix and uses the mean profile as the initial guess can be shown to be the same as regression as far as external information dependence is concerned. The main difference between physical retrieval and regression retrieval is how the residual minimization takes place. In physical retrieval, the residual between the observed radiance and simulated radiance (i.e., calculated via the RTE) is minimized over spectral space which means the residual is minimized across the spectrum. In the regression approach, this minimization for all spectral channels used over profile sample space. In this case the residuals may not be minimal across each individual spectrum but will be minimal for each channel across all the profiles within the ensemble of soundings used for the regression. Considering the advantages and disadvantages of the physical retrieval and statistical retrieval discussed above, the best approach is to use both regression retrieval, which can provide a relatively accurate *a-priori* profiles, followed by the physical retrieval, which can minimize the residual between the radiance spectrum measurement and spectrum simulated from retrieval result.

Many numerical experiments indicate that the statistical retrieval generally produce the most accurate solution. This method contains most information about the problem. While the physical retrieval can not achieve as same accuracy as the statistical method and it's result depends highly on the *a-priori* profiles, especially retrieval from ground-based measurements for the reasons mentioned in the previous chapter. As a tradeoff, a successful statistical retrieval can be achieved using a statistical library for particular observation conditions (i.e., location and season). In this research, this statistical library can be set up by collecting abundant balloon sondes from the nearest meteorological stations (e.g., Mercury station for Nevada case, with 21 km distance; Wallops Island station for Hampton case, with 120 km distance) to the ground-based spectrometers. For the case of AEROSE, both balloon sondes

which are limited in number and the GFS reanalysis for the tropical Atlantic ocean provide the variance of atmospheric parameters for the regression. Thus the GFS reanalysis data can be used to setup the statistical library needed.

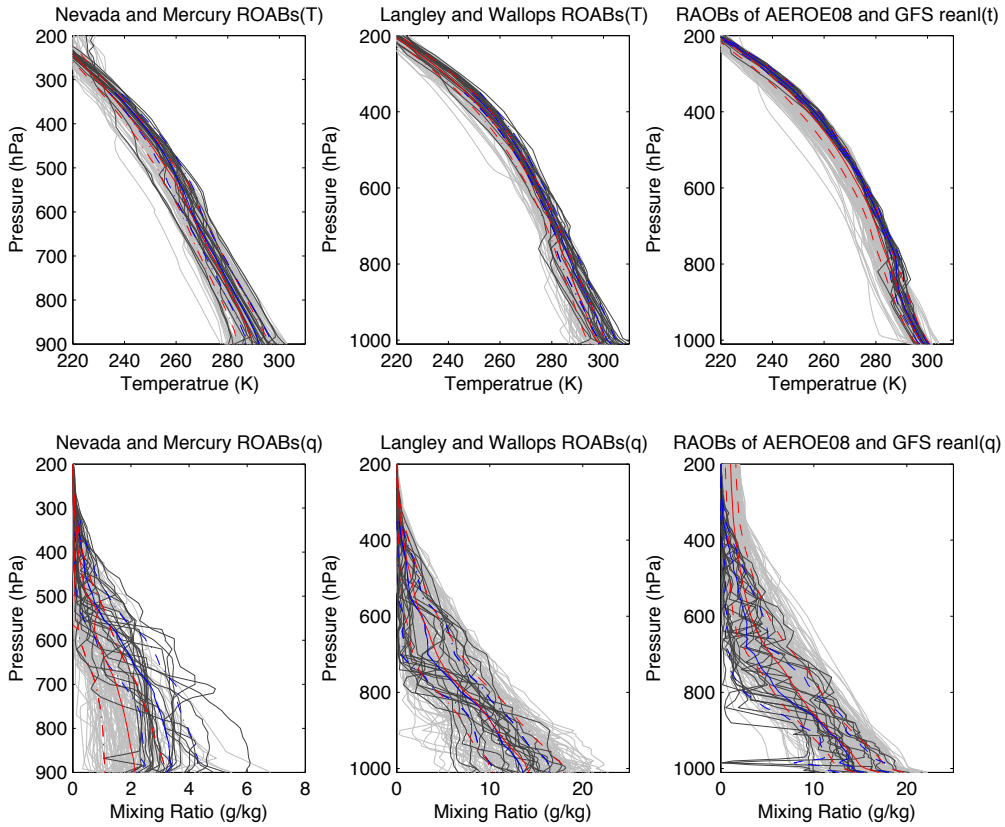

Figure 4.5 Radiosonde variability. Dark grey lines indicate the radiosonde in the retrieval, light grey lines indicate the corresponding statistical radiosondes or GFS reanalysis profiles, solid blue/red lines are the means of observation/statistical.

In our retrieval procedure, the temperature and water vapor are retrieved simultaneously. For the retrieval from downwelling radiance, to avoid the windows region where the difference between simulation of LBLRTM and observation are maxima except water vapor absorption lines, and ozone region near 1000 cm^{-1}, the spectrum within 540 - 740 cm^{-1} and 1100 - 1350 cm^{-1} are selected. For the retrieval from upwelling radiance, the spectrum within 640 - 1000 cm^{-1} and 1100 -1350 cm^{-1} are

selected. These regions provide abundant information of CO_2 absorption and water vapor continuum and absorption.

The interval for pressure grid of the retrieval profiles are varied with the difference locations, though these pressure sets are basically the combination of pressure grid of AERI fast forward model (Table(3.6)) and pressure grid of SARTA fast forward model (Table(3.1)). Below the 600 hPa the pressure grid of AERI model is applied while above the 600 hPa pressure level, the pressure grid of SARTA model is used. Since the surface pressure varies around 1010 hPa in the cases of AEROSE and Hampton, the retrieval pressure grid is expanded to 1010 hPa, and the radiosonde pressure should be normalized to 1010 hPa. For the Nevada cases, where the surface pressure is about 900 hPa, the pressure interval between 900 hPa and 800 hPa is set to 5 hPa to characterized the structure of the boundary layer, and the interval between 800 hPa and 700 hPa is set as 10 hPa.

The flow chart in the figure(4.6) contains the overview of the retrieval procedure. The result of an example of this retrieval procedure are shown in figure(4.7). For this example, both the *a-priori* profiles (the yellow dashed lines in upper plots) of temperature and water vapor are far from the radiosondes (the blue solid lines in upper plots). As the previous section stated, before the combined retrieval, it is necessary to acquire the correct surface information such as skin temperature and surface spectral emissivity. For this reason, the first step of retrieval is to input the ground radiance measurement and the *a-priori* temperature/water vapor profiles into the regression retrieval module with the Eq.(3.2.13):

$$q_{ret} = q_0 + (r_m - r_0)C,$$

$$C = (R'^T \cdot R' + \lambda E^T \cdot E)^{-1} \cdot R'^T \cdot Q'.$$

The retrieval result would be very close to real atmospheric status at planetary boundary layer (the red dashed lines in upper plots of figure(4.7). In the second step of retrieval procedure, the retrieval result of the first step, ground radiance measurements, and coincident satellite radiance measurements are put into the surface retrieval module discussed in section 4.3 to get correct surface information including skin temperature and surface emissivity spectra within window region. In the third step, the result of previous two steps and the ground/satellite radiance measurements are put into the regression retrieval module with the Eq.(3.2.13). After this step, the result (the purple dashed lines in the upper plots of figure(4.7) matches the radiosondes within whole troposphere. In the final step, the physical retrieval module Eq.(3.2.28)

$$X_{i+1} = X_0 + S_i K_i^T S_\epsilon^{-1}[(Y^m - Y(x_i)) + K_i(X_i - X_0],$$

is applied on the results of the third step. It is noticeable that the result of this step (the black solid lines in the upper plots of figure(4.7) are very close to the result of the previous step. As the previous chapter discussed, the regression retrieval can provide very accurate retrieval result, so the improvement of the physical retrieval would not be significant.

The iteration of a retrieval can be considered converged, or completed when the root mean square difference(RMS) between the observed and retrieval calculated radiance falls below a given threshold. For this purpose, the root mean square difference(RMS) of brightness temperature is defined as

$$\chi^2_{n+1} = \frac{1}{nch} \sum_{k=1}^{nch} \frac{[y_k^m - y_k(x_{n+1})]^2}{\sigma^2(k)}, \tag{4.4.1}$$

where k is a channel number, nch is the total number of channels used in the retrieval, the σ^2 is the instrument noise variance, and y_k^m and y_k are the measured and simulated brightness temperature for channel k. For every iteration, a convergence

test is performed on the brightness temperature residual. If $\chi_{n+1} \geq \chi_n$ within two sequential iteration, (i.e. iteration diverges), the iteration would be stopped, and the retrieval result is set to first guess or the previous atmospheric state. If $r_{n+1} \leq r_n$, the iteration continues until r_{n+1} is acceptably small, i.e., less than expectation due to instrumental noise or the iteration is converging a certain value. In addition, at each iteration, each level of the water vapor profiles is checked if it is saturated. For the supersaturated level, the relative humidity is assumed to be unity in magnitude.

The smoothing factors γ in both physical retrieval Eq.(3.2.28) and regression retrieval Eq.(3.2.13)control the background error covariance working in the retrieval and both are difficult to determine. Thus, a discrepancy principle is applied to find the appropriate factor. In the retrieval, for each iteration, the γ is changed according to

$$\gamma_{n+1} = q_n \gamma_n, \tag{4.4.2}$$

where q_n is a factor for γ increasing or decreasing. Starting with $\gamma_0 = 30$, at each iteration we apply the following procedure:

- If $\chi_n^2 < \chi_{n-1}^2$, q_n=0.5.
- if $\chi_n^2 > \chi_{n-1}^2$, q_n=1.5 and set the state vector back to the previous retrieved values ($x_{n+1} = x_n$).

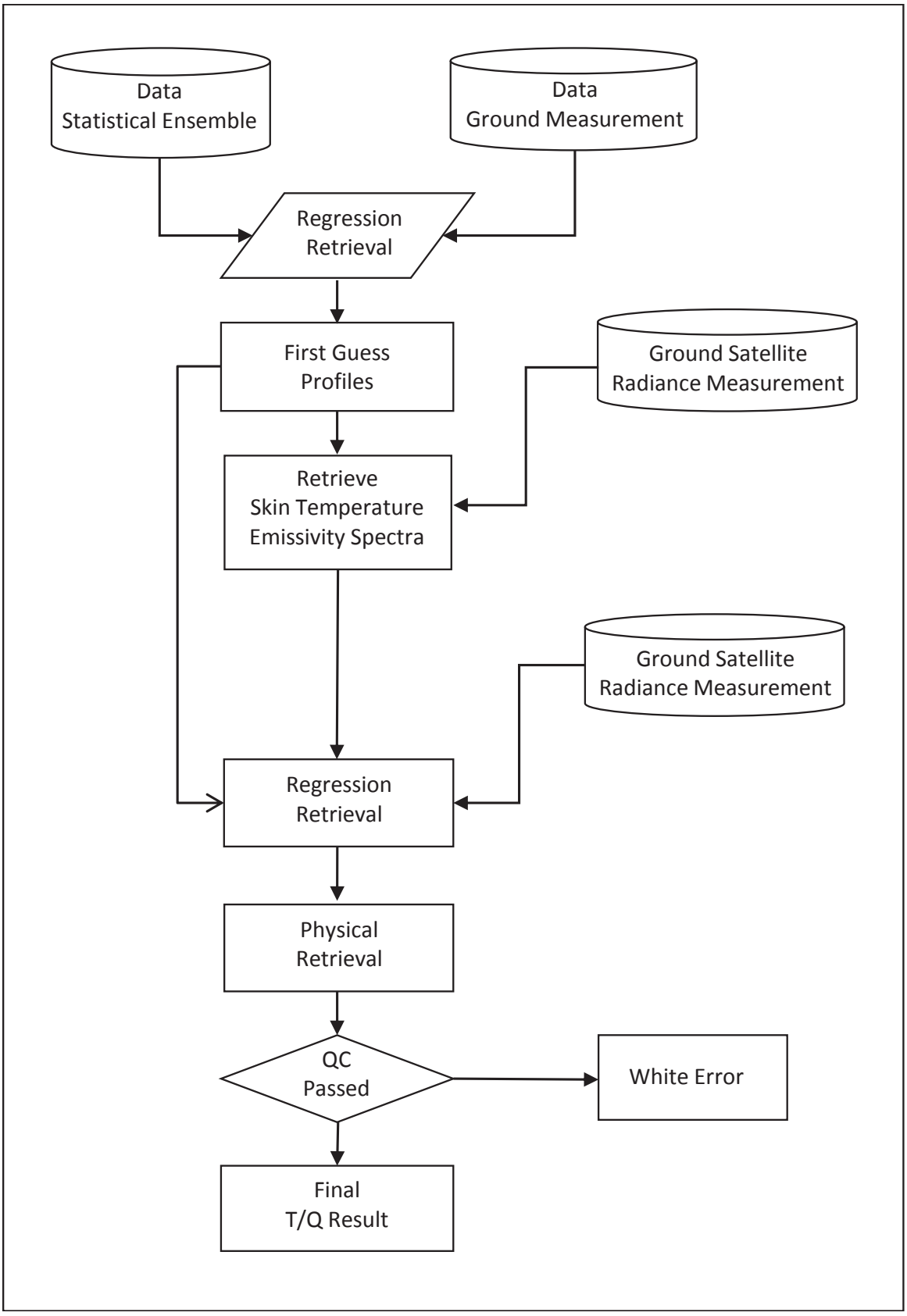

Figure 4.6 Flow chart for the retrieval procedure

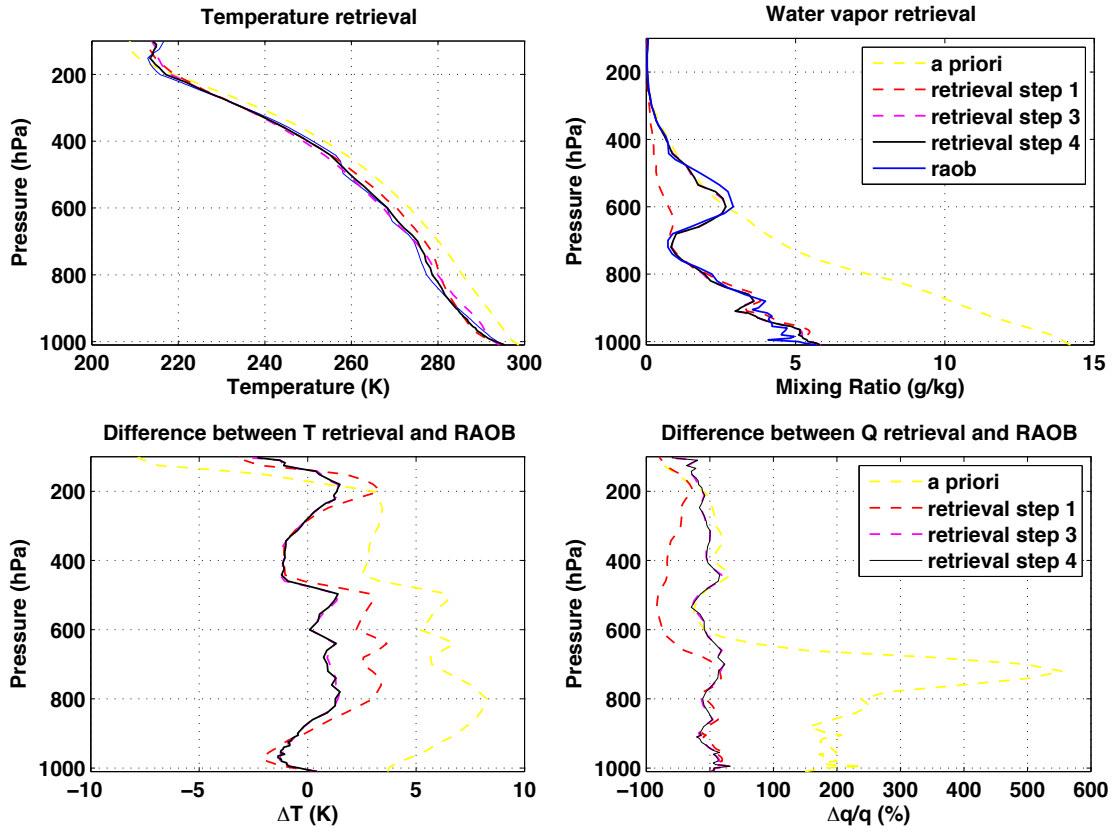

Figure 4.7 An example for the retrieval procedure. The upper plots shows the *a-priori*, the retrieval result of each step of retrieval procedure and the radiosondes. The lower plots shows the difference between the *a-priori*, the retrieval result of each step of retrieval procedure and the radiosondes

CHAPTER 5

RETRIEVAL RESULTS

5.1 Retrieval Validation

Before we apply the retrieval procedure to real radiance measurement, we need to verify its reliability using simulated radiance observations. The downwelling and upwelling radiance are calculated from radiosonde profiles, or RUC reanalysis data, (i.e., simulated data) instead of real measurement as input, thus, the numerical errors induced by the system bias between measurement and RTM simulation are eliminated. On the other hand, the errors induced by instrumental noise are retained for the retrieval, being input using a random number generated with a standard deviation prescribed from instrument calibration data. The noise level for the upwelling (IASI) measurement radiance noise corresponds to 0.3 K in brightness temperature for 280 K of atmospheric scene temperature [Hilton et al. (2012)], whereas the noise level for the downwelling (AERI/ASSIST) measurement assumed to be at 0.4 mW/m^2 str cm $^{-1}$ [Turner et al. (2006)]. More than 200 radiosonde and corresponding simulated radiance spectra for the 4 locations described in previous chapter are selected for the algorithm validation.

To illustrate that the retrieval algorithm dependence on the *a-priori*, the retrieval result for a case where the radiosonde is far from the *a-priori* (statistical mean) is shown in figure (5.1). For plotting the of water vapor mixing ratio, below 500 hPa the x-axis is set to be linear while above 500 hPa the x-axis is set to the logarithm to best visualize the results in view of the exponential decay of specific humidity with decreasing pressure.

Near the ground, the temperature observed by radiosonde is about 8 degree lower than the temperature of the *a-priori* atmospheric state. The temperature of ra-

diosonde remains lower than the temperature of the *a-priori* state until reaching the stratosphere. Meanwhile, the water vapor mixing ratio of the radiosonde is much lower than the mixing ratio of the *a-priori* state from surface to 400 hpa level. The plot of relative humidity indicates that the radiosonde profile has a very significant moistening between 400 hPa to 100 hPa while the relative humidity of the *a-priori* decreases steadily.

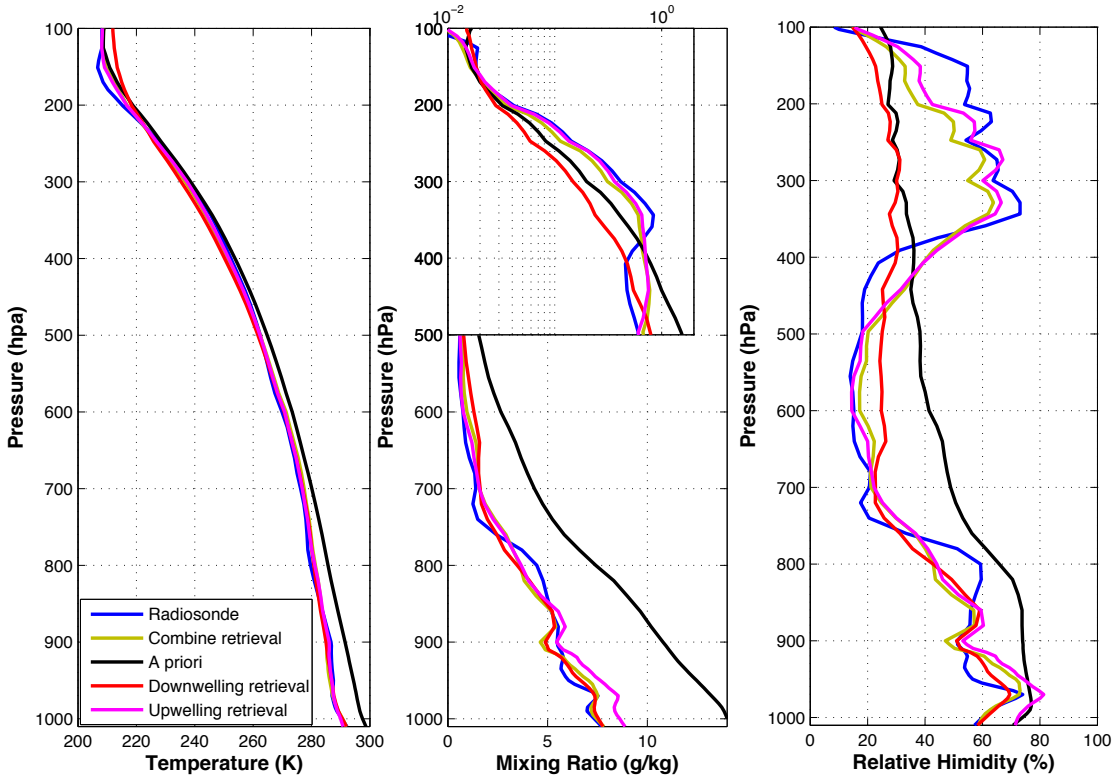

Figure 5.1 A simulation profile retrieval. Retrieved temperature and water vapor profiles compared to the *a-priori* and the radiosonde profiles.

Figure (5.1) also shows typical features of the retrieval from downwelling radiance (called the "downwelling retrieval"), the retrieval from upwelling radiance (called "upwelling retrieval") and the retrieval from both spectra (called "combined retrieval"), respectively. For the temperature retrieval, although all three retrieval appear to be very close to radiosonde near the ground, there is a 1.5 K difference between the

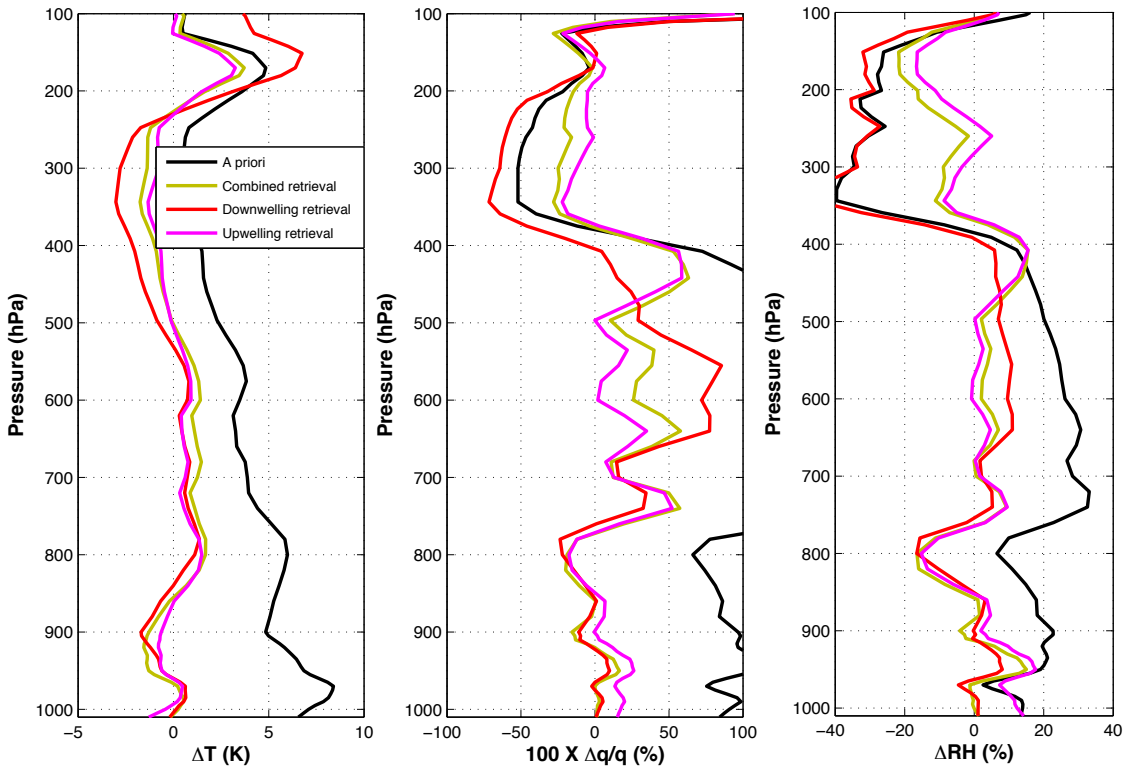

Figure 5.2 A simulation profile retrieval comparison. Differences between the retrievals, *a-priori* and the radiosonde profiles

radiosonde and the upwelling retrieval while the difference between radiosonde and downwelling and combined retrieval is near zero. Below 500 hPa, there is no discernable difference between the three retrievals. Above 500 hPa, the downwelling retrieval diverges from radiosonde reaching a maximum 10 K difference at the tropopause. Both the upwelling retrieval and the combined retrieval diverge from the radiosonde at tropopause with a much smaller error of 4 K, nevertheless they match the radiosonde very well at all other levels. The peak difference at the tropopause associated with the inability to resolve the sharp tropopause temperature structure as expected due to the relatively low vertical resolution of the radiance observations used for the retrieval.

For the water vapor retrieval, the maximum difference between the combined retrieval (upwelling retrieval, low part of downwelling retrieval) and radiosonde is $\sim$ 50 % . Since the relative differences between the initial water vapor profile and radiosonde are larger than 100%, in main part of troposphere, all three retrieval are considered to be successful. Like the temperature, the improvement in mixing ratio accuracy of obtained by combining the upwelling and downwelling radiance spectra for profile retrieval is impressive. Below 800 hPa, the combined retrieval follows the downwelling retrieval and maintains a relative difference less than 20%. Near the ground, these two retrievals match the radiosonde exactly. Although the upwelling retrieval catches the inversion structure of radiosonde near ground, it possesses a larger error. From 800 hPa to the tropopause, the difference between upwelling retrieval and radiosonde is less than $\sim$ 20%, except in the 840 hPa to 440 hPa layere where the difference between downwelling retrieval and radiosonde deteriorates and follows the structure of the *a-priori* profile. The combined retrieval follows the upwelling retrieval above the lower tropospheric boundary layer. The plot of relative humidity profiles shows a similar result. From the plot of difference of relative humidity (ΔRH), it can be concluded that the combined retrieval error of relative humidity is less than 10% throughout most of the troposphere.

Figure (5.3) shows the difference between the radiance calculated from the radiosonde considered to be the "measured" radiance for this retrieval simulation, and the radiance calculated from retrieval result. Both the radiance spectrum residuals from the upwelling radiance simulation and downwelling radiance simulation indicate that the profile accuracy improvement provided by the combined retrieval is dramatic. The magnitude of the difference between the simulation from combined retrieval and the "measurement" is no more than 0.1K, while the magnitude of difference between the radiances calculated from the other two retrievals and the "measured" radiance can reach 1 K for upwelling radiance and 0.5 K for downwelling radiance, respec-

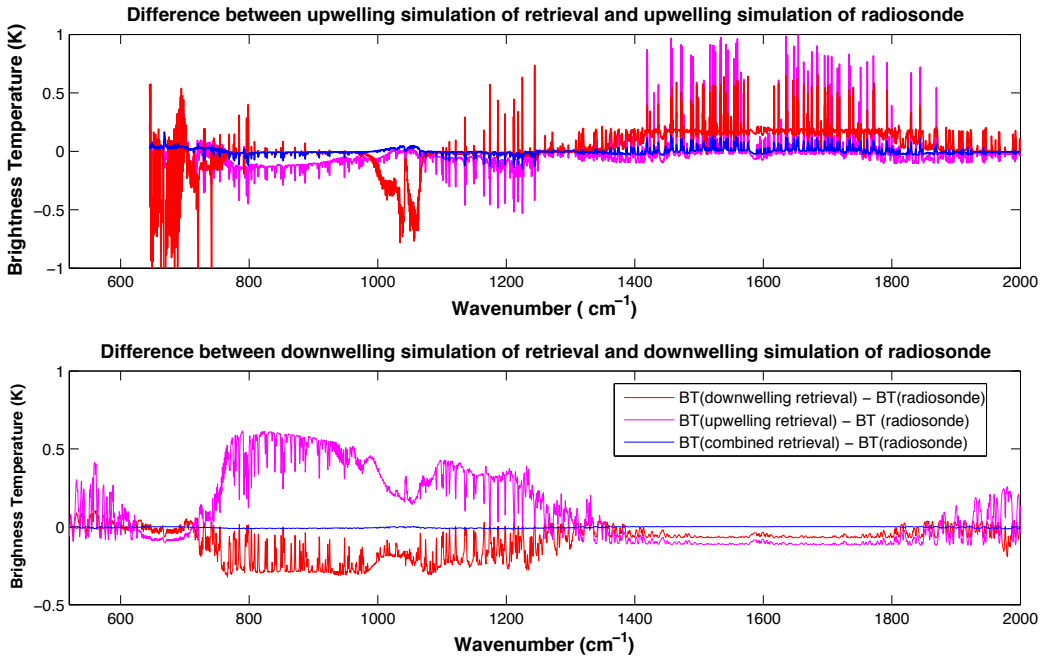

Figure 5.3 Brightness difference between simulated radiance from retrieval result and from radiosonde, Upper panel for upwelling radiance simulation, lower panel for downwelling radiance simulation, respectively.

tively. For the upwelling radiance spectra, within the opaque region (650-750 cm^{-1}, the residual between simulation from upwelling retrieval and "measurement" is much closer to the residual between the simulation from combined retrieval and "measured" radiance than to the residual between the simulation from downwelling retrieval and "measured" radiance. On the other hand, within window region (750 - 1200 cm^{-1}), the residual between the simulation from the downwelling retrieval and "measurement" is much samller than the residual between the simulation from the combined retrieval and the "measurement" than to the residual between the simulation from upwelling retrieval and "measured" radiance, except for the ozone region (1000 - 1100 cm^{-1}) and some strong water vapor absorption regions. This result indicates that the upwelling retrieval and the combined retrieval are better than the downwelling retrieval above the low-troposphere whereas the downwelling radiance and combined retrieval are better than the upwelling retrieval.

For the downwelling radiance spectra, within the opaque region, the residual between simulation from the upwelling retrieval and the "measurement" is much smaller than the residual between the simulation from the combined retrieval and "measurement". Within the rest of the atmosphere, the residual between the simulation from the upwelling retrieval and the "measurement" is on the same order of the residual between the simulation from the downwelling retrieval and the "measurement" (0.5K vs. 0.3K). This result is consisted with the comparison between retrieved profiles and the radiosonde as discussed previously: that is within the boundary layer the combined retrieval and the downwelling retrieval is better than the upwelling retrieval while within free troposphere, the upwelling retrieval and the combined retrieval are better than the downwelling retrieval. In both the upwelling spectra and the downwelling spectra, the magnitude of all three residuals are remarkably smaller than measurement noise and errors induced by radiative transfer models.

5.2 Retrieval case studies

5.2.1 Hampton, VA

Because the sea-land distribution of the Peninsula area is very complicated, the IASI spectra for every footprint in each 2×2 footprint field of regard may be different from all others. Unlike other cases studies here, it is necessary to choose the IASI spectrum for the proper footprint which has almost same surface properties of the in-situ radiosonde measurement (i.e., NASA Langley Research Center) thus avoiding the footprints for true ocean regions.

August 11th 2009

The figure(5.4) shows the AVHRR infrared image (brightness temperature at Channel 4) and visible reflectivity image of the peninsula area and the ground-based

measurement location (37.1 °N, 76.32 ° W) and the 4 FOVs (16 footprints) nearest to that location on August 11th 2009. In this figure, the nearest footprint to the Langley Research Center (LaRC) where the balloon was launched is located in the Chesapeake bay, while the second nearest footprint is located at Norfolk, VA, but a brightness temperature and visible reflectivity similar to that at Langley, thus this footprint is assumed to represent the LaRC area for the retrieval. On that day, the time of the IASI overpass was 14:29UTC while the balloon was launched at 14:58UTC. Although there was about a half hour time difference and a 26-km distance between the IASI overpass and balloon launch. Considering that the location time the IASI overpass is about 10:00 am local time when the atmosphere is stable, the atmospheric state represented by the IASI radiance measurement was comparable to the atmospheric state represented by radiosonde.

The figure(5.5) shows the retrieval result at the time when the IASI overpass. In this retrieval, the mean profiles of the 3-year radiosonde climatology for the Wallops island were used as the *a-priori* profiles. On that day, the radiosonde profile indicates a typical mid-latitude summer atmospheric state with a very high($\sim$ 305K) surface temperature and a moderate relative humidity ($\sim$ 60%). The water vapor mixing ratio profile from radiosonde indicates that there is a small inversion layer from surface to 950hPa with the value of about 15g/kg, above that, the water vapor mixing ratio decreases exponentially as the altitude increases except for a protrusion within the 700-600 hPa layer which is obvious in the relative humidity plot. Above the 500 hPa level, the magnitude of the mixing ratio is small, so we can use relative humidity profiles in the right plot describe the variance of water vapor. In the relative humidity plot, the value of radiosonde reaches a minima of 10% at 500 hPa, then the value increases slowly until 150 hPa (tropopause) with some oscillations. Above the tropopause, the value of radiosonde decreases dramatically.

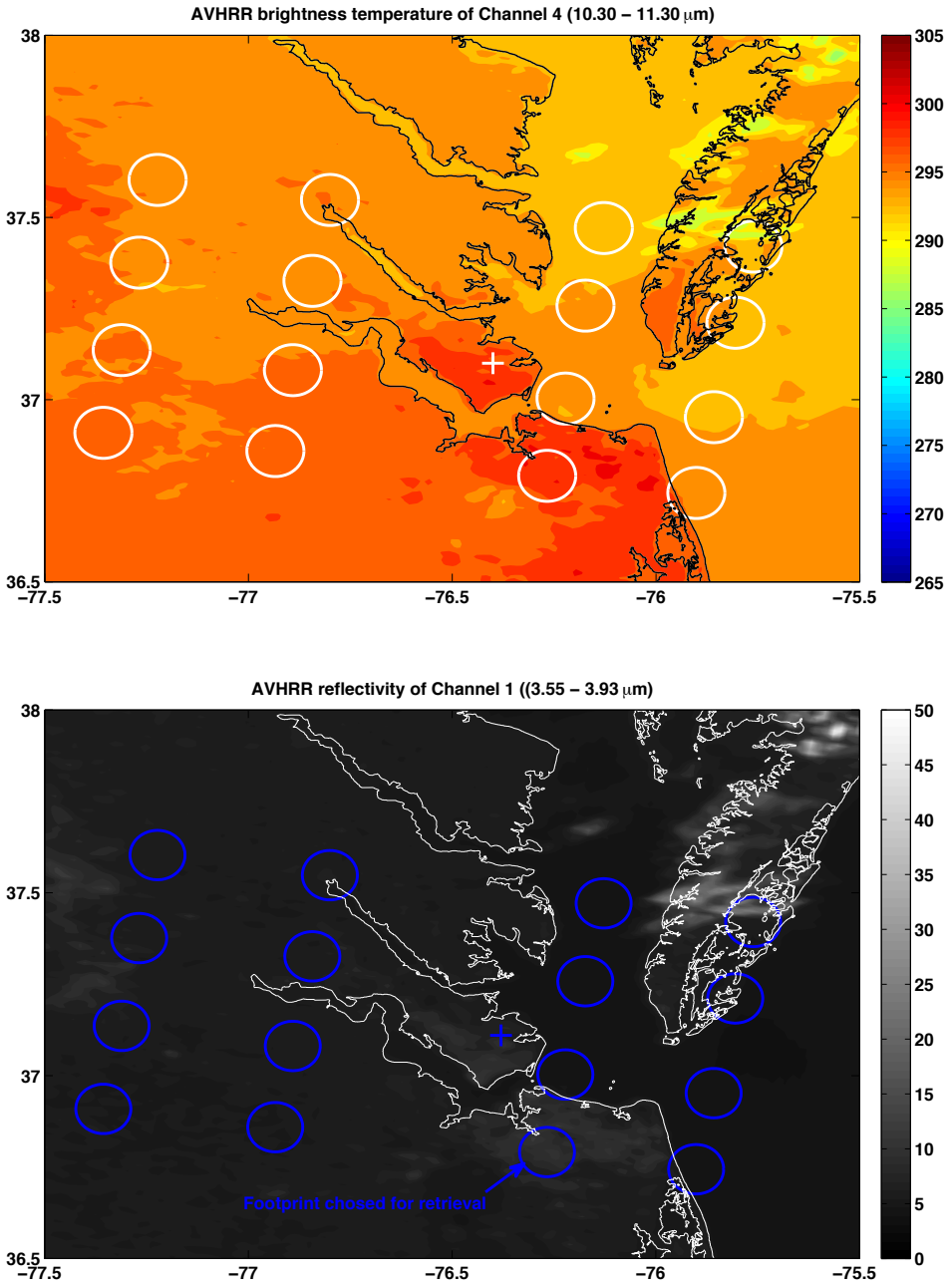

Figure 5.4 AVHRR images of case on 2009-08-11. Circles indicate the IASI footprint, cross indicates location of balloon launches

For the temperature retrieval, the retrieval from the ground-based AERI measurement matches the radiosonde very well at low levels up to 500 hPa, except at about top of the planetary boundary layer where the temperature retrieval is higher than

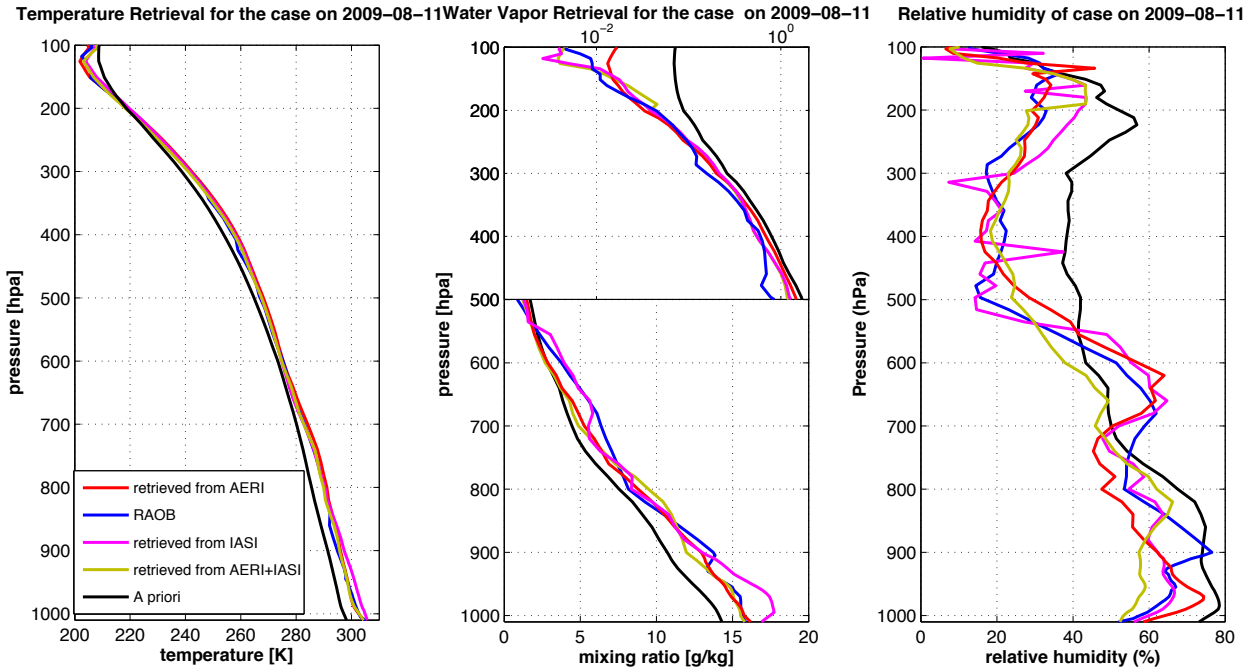

Figure 5.5 Retrieval profiles of the case on 2009-08-11, 15:00UTC, Langley, VA. Black lines are the *a-priori* (statistical mean for radiosonde at Wallops Is.); Blue lines are the radiosonde profiles; Purple lines are the retrieval from IASI measurement; Red lines are the retrieval from ground AERI measurement; Dark yellow lines are the retrieval from IASI and AERI measurement combination.

radiosonde by about 1 K. On the other hand, the retrieval from IASI measurement matches the radiosonde very well above 800 hPa. Below 800 hPa, this retrieval is about 1-2 K higher than the radiosonde. The temperature retrieval from combined radiance measurements is identical with AERI retrieval for the atmosphere below 700 hPa, above which this combined retrieval close to the IASI retrieval.

For the water vapor retrieval, within the low troposphere, the satellite retrieval is wetter than the other two retrievals which are retrieved from the ground based measurement and the combined measurements. Both the AERI retrieval and the combined retrieval catch the inversion structure shown by the radiosonde profile below 950 hPa, while the inversion structure of IASI retrieval is not as large as the other two retrievals. Unfortunately, the water vapor feature at 900 hpa shown by the

radiosonde can not be retrieved by any of three methods. In the mid-troposphere, the protruding within 700-600 hPa of the radiosonde was catched by the IASI and combined retrievals. The AERI retrieval places same protrusion at a higher altitude. Around 700 hPa, the retrieval from the AERI spectrum drier than the other retrievals and the radiosonde. Above the 500 hPa, the difference of water vapor mixing ratio between retrievals can not be distinguished. The plot of relatively humidity profiles indicate that the retrieved profiles have a smoother structure than radiosonde profile. Within lower troposphere, the difference between the retrieved profiles and radiosonde profile are less than 15 percent except at around 920 hPa and 430 hPa where the radiosonde has strong protrusions. Above 300 hPa, the relative humidity retrieved from AERI spectrum increases much more rapidly than the other retrievals and the radiosonde.

The detailed differences between radiosonde and the retrievals from real measurement are shown in the figure(5.6). The differences between the radiosonde and the retrieval from simulated radiance of radiosonde are also be presented in this figure. In later comparisons, the retrieval errors can be considered to be mostly due to the input radiance sensitivity and the retrieval algorithm statistics, the errors caused by the radiative transfer model and the difference due to the mismatch between radiosonde and IASI field of view being much smaller. The left plot indicates that the retrieval from simulation radiance improves the temperature slightly except the upwelling retrieval at lower atmosphere where the improvement reaches about 0.3 K. Also, both the simulated and real measurement two downwelling retrievals get a systematic 1K warmer than the radiosonde result, meanwhile the combined retrieval and upwelling retrieval are oscillating around radiosonde with magnitude of 1K up to tropopause. Near the tropopause, all the oscillations of three retrievals are more larger.

The plot of relative difference between radiosonde and retrieval water vapor shows that below the 650 hPa all three retrievals are very close to radiosonde, i.e., the

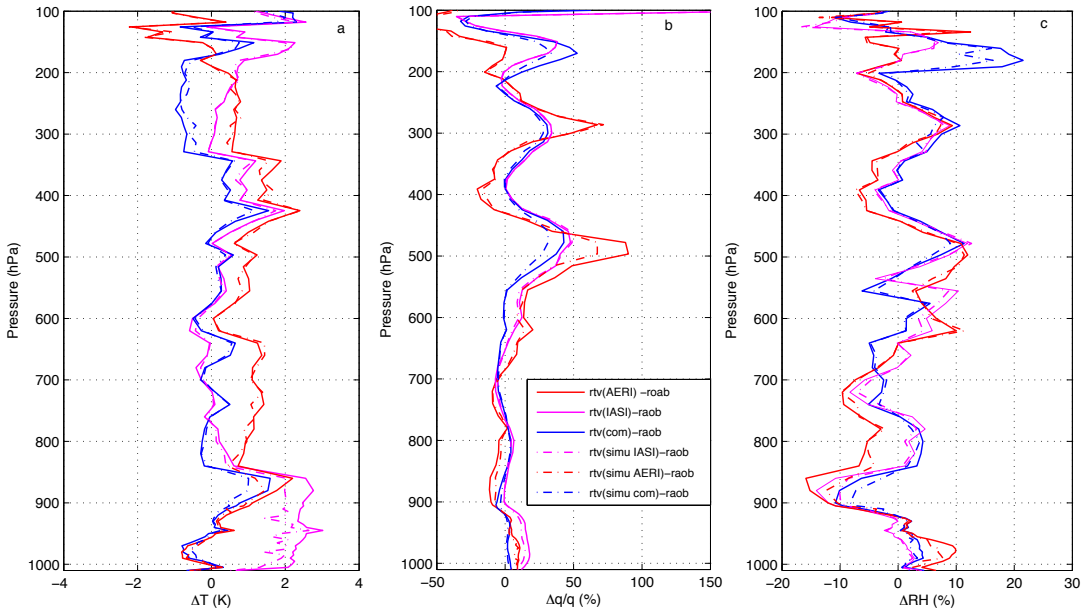

Figure 5.6 Difference between retrieval results and radiosonde of temperature(a), water vapor (b), and relative humidity (c). In (b) the relative difference for water vapor (($q_{retrieval}$-q_{raob})/q_{raob}) on 2009-08-19. Blue lines are the difference between combined retrieval and radiosonde; Purple lines are the difference between upwelling retrieval and radiosonde; Red lines are the difference between downwelling retrieval and radiosonde. Solid lines are the retrieval from real measurements, and dot-dashed lines are the retrieval from simulated radiance of radiosonde.

magnitude of difference are about 25%. Near the surface the downwelling retrieval and combined retrieval performance are much better than upwelling retrieval. And in this section, the improvement of retrieval from simulated radiance is not noticeable. From 650 hPa to tropopause, all plots of the difference show that there are three peaks in this section. The residual of the upwelling retrieval and the residual of combined retrieval have same magnitude ($\sim$ 35%), while the residual of downwelling retrieval has a larger magnitude (¿50%). These three peaks occur at 480 hPa, 290 hPa, and 180 hPa. The water vapor profile of radiosonde in figure(5.5) shows that the lapse rate of water vapor changes so dramatically at these three pressure levels and that all retrievals can not retrieval these inflexion points.

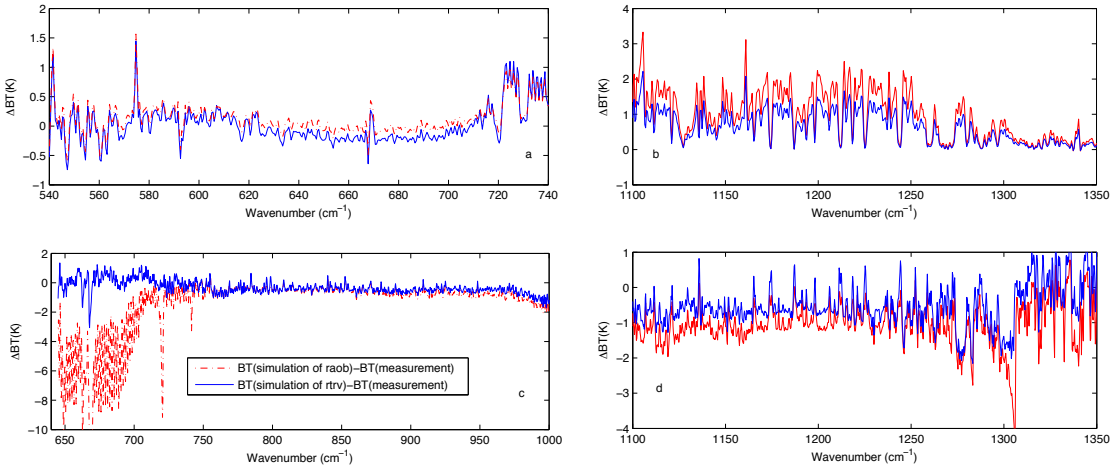

Figure 5.7 Brightness temperature spectra comparison of measurement and simulation on 2009-08-19. Plot (a) and (b) show the difference between AERI measurement and simulation from radiosonde / retrieval profiles within 540 - 720 cm^{-1}, 1100 - 1350 cm^{-1}. Plot (c) and (d) show the difference between IASI measurement and simulation from radiosonde / retrieval profiles within 645 - 1000 cm^{-1}, 1100 - 1350 cm^{-1}.

Figure(5.7) shows the comparison between the measured spectra and simulated spectra in the brightness temperature scale for this retrieval case. In the previous chapter the spectra coverage used in the retrieval was described. For the retrieval from downwelling radiance the regions of 540 - 720 cm^{-1} (CO_2 and H_2O region), 1100 - 1350 cm^{-1} (H_2 region)are selected to avoid the window region of 800 cm^{-1} - 1000 cm $^{-1}$ and the ozone region of 1000 - 1100 cm^{-1}. For the retrieval from upwelling radiance the regions of 645 - 1000 cm^{-1} and 1100 - 1350 cm^{-1} are selected to avoid the ozone region. For this case, both downwelling spectra and upwelling spectra indicate that the simulations from radiosonde and measurements match very well. The magnitude of difference for downwelling spectra are about 1K and 2K for CO_2 region and H_2O region, respectively. The difference for upwelling spectra has almost the same magnitudes as the downwelling spectra except the opaque region of 645 - 700 cm^{-1} where the contribution from the upper atmosphere are represented. Because the balloon can only reach a height of 30 hPa, climatological profiles above 30 hPa are

applied to fill in the radiosonde profiles. This small difference can explain the small difference between retrieval from real measurement and retrieval from the simulation from the radiosonde which are shown in the figure(5.6). The curves of the difference between the simulation retrieval result and the real radiance measurement indicate that there is only a slight improvement from the simulation except for the retrieval for the very high atmosphere where the improvement is large. This case implies that even the mismatch errors and radiative transfer model error of radiance have a small effect on the retrieval. If the lapse rate of water vapor in upper troposphere changes rapidly, none of the retrievals can catch this structure.

5.2.2 Nevada

As described in the previous chapter, the altitude of the Nevada ground measurement site is about 980 m ($\sim$ 900 hPa), the ground type is vegetable free, and the humidity is very low ($\sim$ 30 %) during spring . All these make the transmittance within window region very high, and the difference between the ground skin temperature and ground air temperature very large ($\geq \pm$ 5K). This difference may affect the retrieval result from the IASI measurement in the planetary boundary layer. So even for the retrieval from IASI spectrum, the ground ASSIST measurement and the corresponding IASI spectrum is needed to define the proper surface skin temperature and surface emissivity for the retrieval.

April 19th 2010

For this case the balloon was launched at 18:31 UCT while the IASI overpassed the measurement site at 17:56 UTC, thus the temporal difference is less than one hour. The figure(5.8) shows the AVHRR channel 4 infrared image and the channel 1 visible reflectance image of the region of the balloon launch and ASSIST measurement (36.81 ^{o}N,115.96 ^{o}N W), the ground measurement location. The nearest IASI footprints are

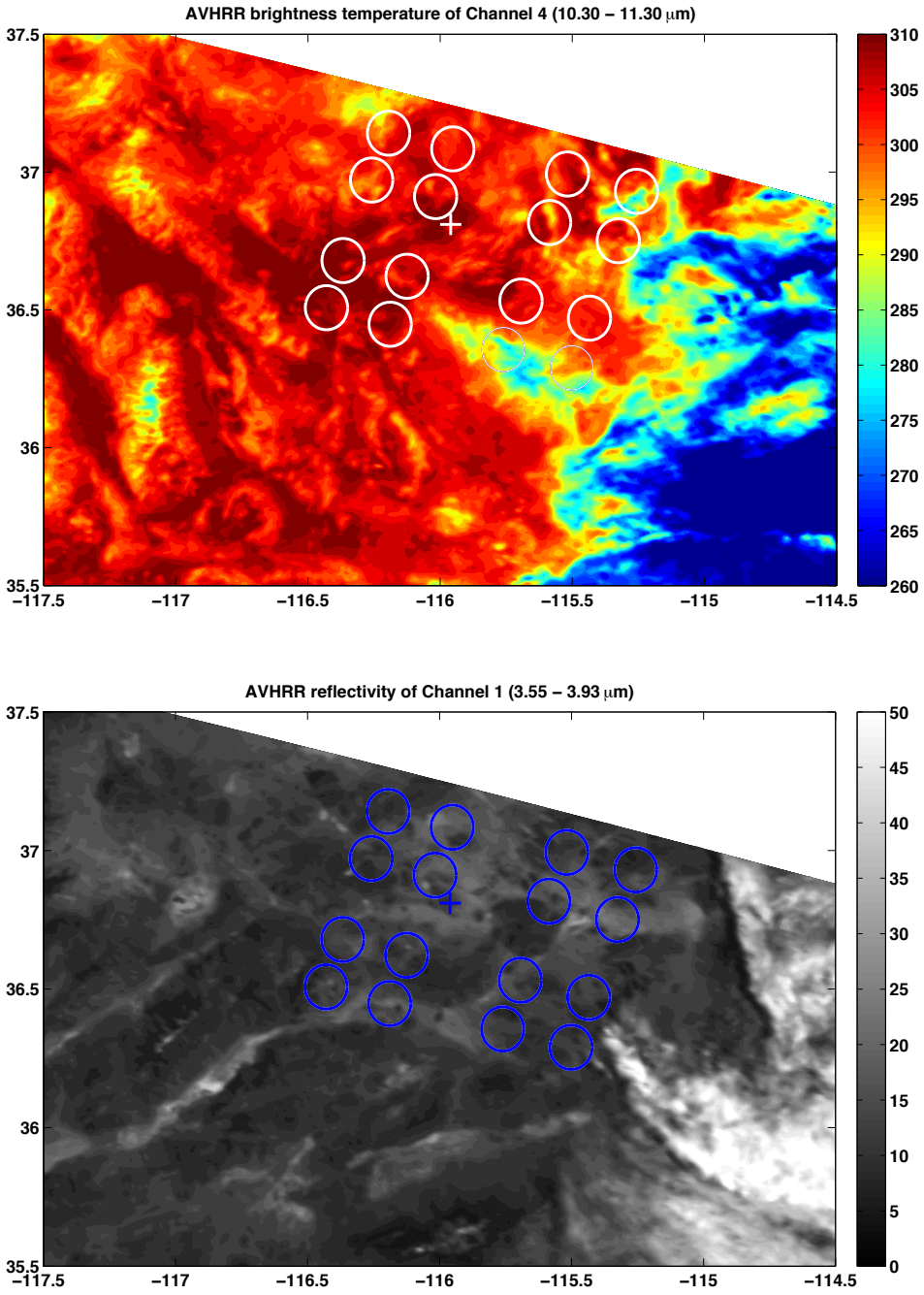

Figure 5.8 AVHRR images of case on 2010-04-19. Circles indicate the IASI footprint, cross indicates location of balloon launches

also plotted in the figure. This figure indicates that the balloon launch location was covered by one IASI foot print. Thus, the IASI and radiosonde represent the same

atmospheric state. The figure of infrared image from AVHRR channel 4 also indicates that the surface temperature of the in-situ location is about 310 K, while the visible reflectivity of AVHRR channel 1 at the in-situ locatio is no more than 30 percent, thus we can assume that this case is a clear case with a very high skin temperature.

The left plot of figure(5.9) shows the temperature profiles of radiosonde and retrievals respectively. From the surface to the 500 hPa, the temperature retrieval from the IASI measurement is oscillating around the radiosonde with the magnitude of 2K; meanwhile, the retrieval from ASSIST measurement and retrieval from the combined IASI and ASSIST measurements matches the radiosonde very well. Above 500 hPa to 350 hPa, the temperature of ASSIST retrieval is lower than temperature of radiosonde and the other two retrievals about 2-3 K. Above 350 hPa, the temperature of all retrievals are lower than the radiosonde temperature about 2-4 K. Near the tropopause, where the temperature decreases dramatically, none of the retrievals can resolve the strong temperature features. Above the tropopause, these difference are significant.

The middle plot of figure(5.9) shows the water vapor mixing ratio profiles of radiosonde and the three retrievals. There is a very large inversion below 600 hPa where the radiosonde has a constant value of about 3.4 g/kg for water vapor profile. Above 600 hPa, the value of radiosonde deceases exponentially with altitude except at 650 hPa and 370 hPa, where other inversions exist. All three retrievals catch the large near constant moisture mixing ratio layer near surface, but value of the retrieval from IASI spectrum is about 0.7 g/kg lower than the value of radiosonde; the moisture layer of retrieval from ASSIST measurement reaches about 700 hPa; while the combined retrieval retains the same features of radiosonde. For the inversion at 650 hPa, both retrieval from IASI spectrum and combined retrieval catch it with more protruding shapes. For the inversion at 370 hPa, all retrievals failed to catch it. Above the 250 hPa, the radiosonde water vapor drops dramatically which could be

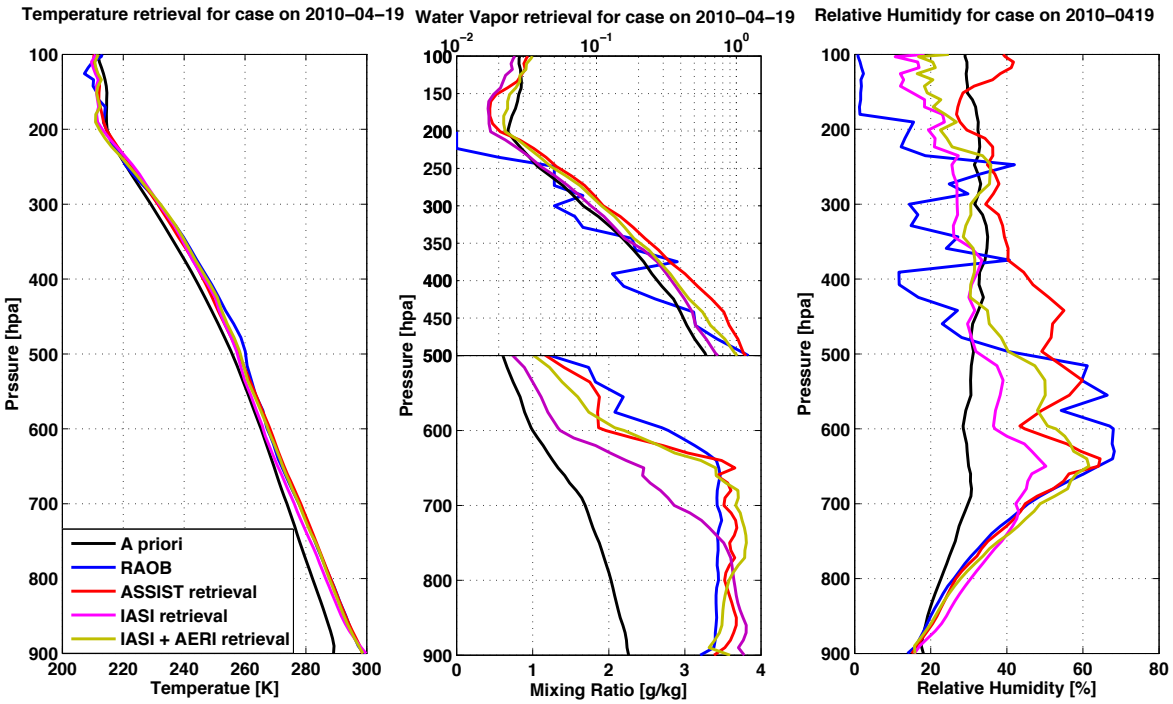

Figure 5.9 Retrieval profiles of the case on 2010-04-19, 15:00UTC, Nevada. Black lines are the *a-priori* (statistical mean for mercury station radiosondes; Blue lines are the radiosonde profiles; Purple lines are the retrieval from IASI measurement; Red lines are the retrieval from ground AERI measurement; Dark yellow lines are the retrieval from IASI and AERI measurement combination.

caused by instrumental error, while all the retrievals keep a lower lapse rate until the tropopause. The relative humidity plot of figure(5.9) shows that from surface to 600 hPa all three retrieval catch the inversion structure of radiosonde except the maxima value at 650 hPa where the IASI retrieval is 10 percents lower than maximum values of the others. Above 500 hPa, the combined retrieval is gradually approaching the IASI retrieval. Unfortunately, for the upper portion of atmosphere, all three retrievals smooth through zigzag shape of radiosonde.

The detailed difference between the retrieval and the radiosonde for this case are shown in the figure(5.10). The retrievals from the simulated radiances are also shown. From surface to 500 hPa, all the temperature retrievals match the radiosonde very well, the differences are no more than 1 K. The improvement of the retrieval

from simulated radiance can be observed in this section, especially for the upwelling retrieval. The radiosonde temperature structure at 480 hPa makes the residual of the retrievals reach 3 K, 2 K, and 1K for downwelling retrieval, combined retrieval, and upwelling retrievals, respectively. Near the tropopause, the residual of all three retrievals oscillate as the altitude increase. The middle plot of figure(5.10) shows the residual of the water vapor retrieval, from to surface to 850 hPa, the residual of the combined retrieval, and the downwelling retrieval are a constant 6% while the

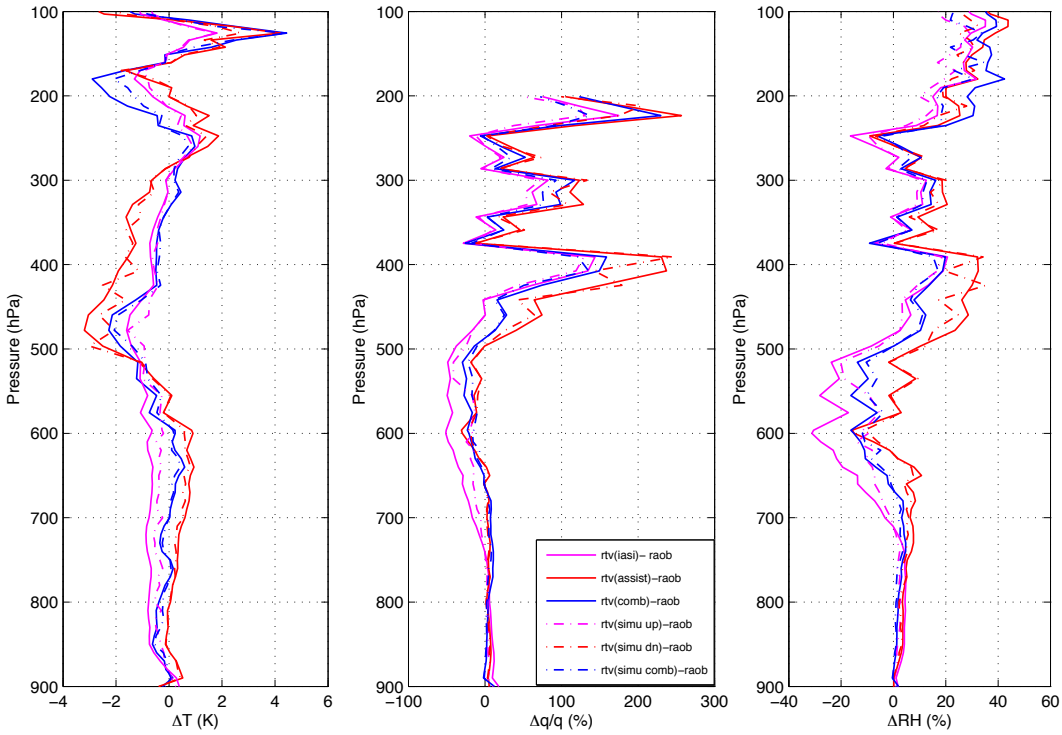

Figure 5.10 Difference between retrieval results and radiosonde of temperature(a), water vapor (b), and relative humidity (c). In (b) the relative difference for water vapor (($q_{retrieval}$-q_{raob})/q_{raob}) for case of 2010-04-19. Blue lines are the difference between combined retrieval and radiosonde; Purple lines are the difference between upwelling retrieval and radiosonde; Red lines are the difference between downwelling retrieval and radiosonde. Solid lines are the retrieval from real measurements, and dot-dashed lines are the retrieval from simulated radiance of radiosonde.

residual of upwelling retrieval varies up to 15%. From 850 hPa to 500 hpa, all retrieval residuals increase gradually with different rates. In this section, the improvement of retrieval from simulated radiance is the insignificant throughout the whole atmosphere. From 480 hPa to 200 hPa, as in the previous case, all three water vapor retrieval residuals have three peak at 400 hPa, 300 hPa, and 260 hPa, respectively, due to the strong perturbation of radiosonde profile at these heights. For this case, the magnitude of peak reaches 200%, a much greater value than the previous case. Above the 200 hPa, as the radiosonde water vapor drops to very low value, the relative residual of retrieval increase greatly, such that the relative residual is not shown in that section of profile.

The comparison of spectra for this case is shown in figure(5.11). Like the previous case, the difference between measurement and simulation are keep a magnitude of 1-2 K for most regions. Also, the residual of the radiance simulated from retrieval result is better than the radiance simulated from radiosonde, although the improvement is not very significant. And the two residual spectra keep almost same shape except for the 540-600 cm^{-1}region for downwelling radiance which is sensitive the water vapor. In 2010, the ASSIST was still immature, and there may be a calibration problem for that water vapor region. With the abundance of channels used in the retrieval, the effect of the errors for that spectral region are minimized.

5.2.3 ARM SGP facility at Lamont, OK

As decribed in the previous chapter, each day the overlapping time of Metop overpassing Lamont and the radiosonde launch time is at about 17:30 UTC or 11:30 local time, when the atmospheric structure is generally stable. On the day of October 17, 2010, the Metop overpassed Lamont at 17:17UTC while the balloon was launched at 17:30UTC. The AVHRR infrared image shown in figure(**??**) indicates that brightness temperature at the location of balloon launch and brightness temperature of the IASI

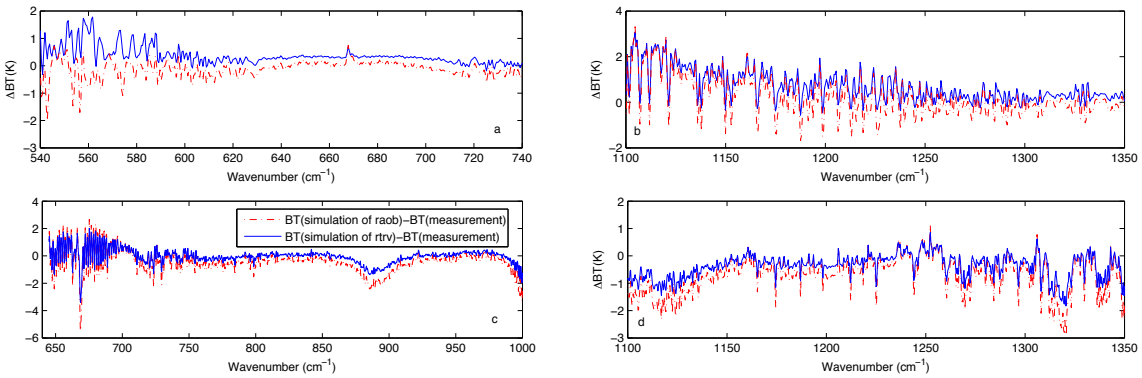

Figure 5.11 Brightness temperature spectra comparison of measurement and simulation on 2010-04-19. Plot (a) and (b) show the difference between ASSIST measurement and simulation from radiosonde / retrieval profiles within 540 - 720 cm^{-1}, 1100 - 1350 cm^{-1}. Plot (c) and (d) show the difference between IASI measurement and simulation from radiosonde / retrieval profiles within 645 - 1000 cm^{-1}, 1100 - 1350 cm^{-1}.

footprint nearest to the ARM SGP site are both 287 K, while AVHRR visible reflectivity of two locations are $\sim$ 15%. So we can assume that ground AERI measurement, radiosonde, and IASI measurement represent same atmospheric state. These AVHRR images and the Lidar measurement in the ARM SGP facility demonstrate that at the during the Metop overpass and balloon reaching tropopause, there was no significant cloud cover this region.

The retrieval result and corresponding radiosonde profiles are shown in the figure (5.13). For this case, the temperature profile of radiosonde is far away from the *a-priori* profile especially for lower troposphere where the difference between radiosonde and the *a-priori* is $\sim$5 K. Nevertheless, the plot of water vapor mixing ratio and the plot of relative humidity indicate that the radiosonde is much wetter than the *a-priori* for entire atmosphere. The radiosonde relative humidity is 10 - 20 percent lower than the relative humidity of the *a-priori*. It is noticeable that there is a dramatic perturbation below 900 hPa for both temperature and water vapor.

Below the 900 hPa, where the perturbation exists, all temperature retrievals fail to resolve structure. Differences between retrieval and radiosonde at that altitude

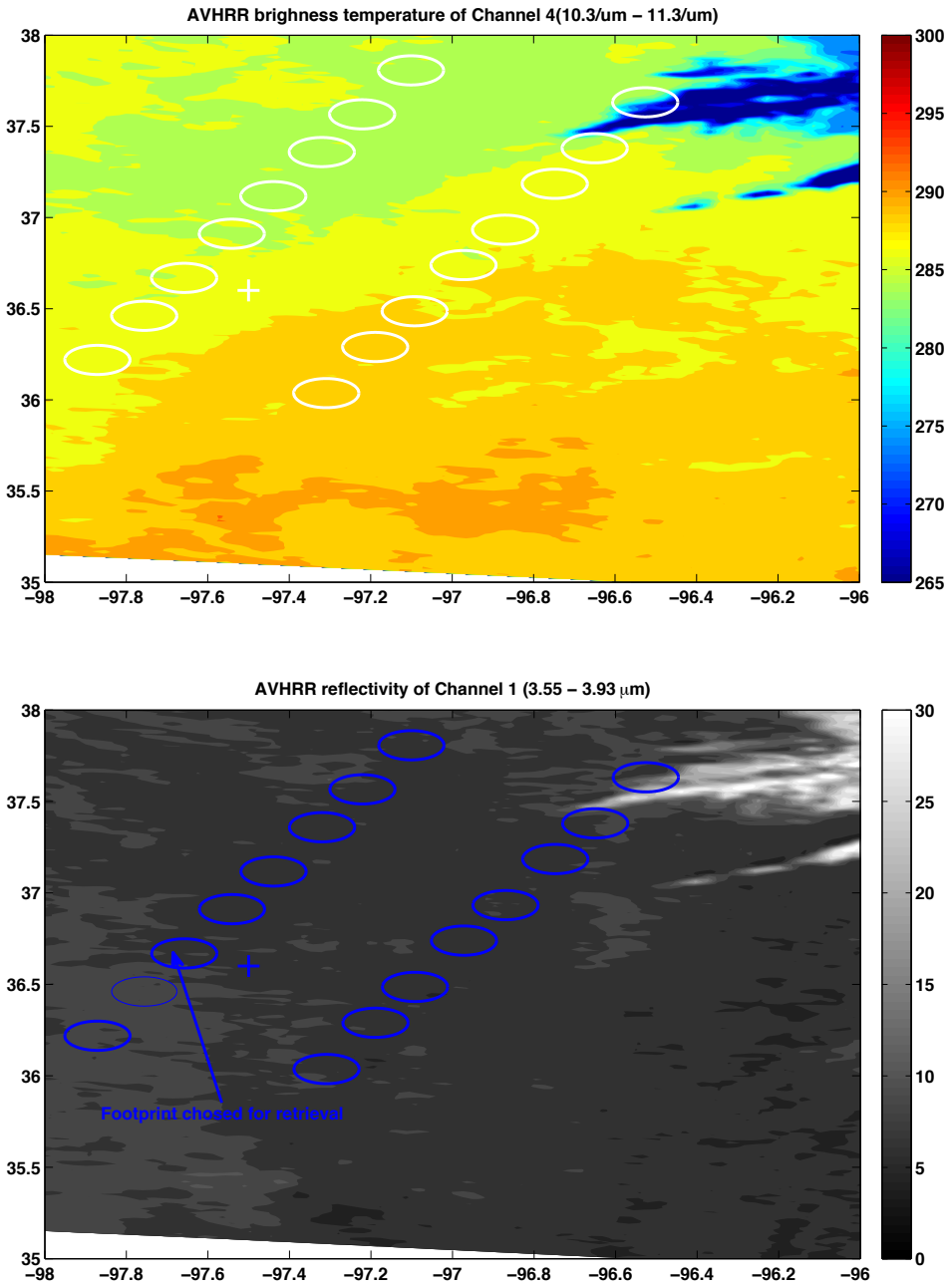

Figure 5.12 AVHRR images of case on 2010-10-17. Circles indicate the IASI footprint, cross indicates location of balloon launches

reach 1.5 K, 1.8 K, 2.5 K for the AERI retrieval, the combined retrieval, and the IASI retrieval, respectively. Above 900 hPa, the temperature difference between the IASI retrieval or the combined retrieval and radiosonde is oscillating with a magnitude of

1.5 K. Meanwhile, the temperature difference between the AERI retrieval and the radiosonde is oscillating with a larger magnitude (∼3 K), especially in the 250 hPa to 150 hPa layer, where this difference changes from 3 K to -2 K.

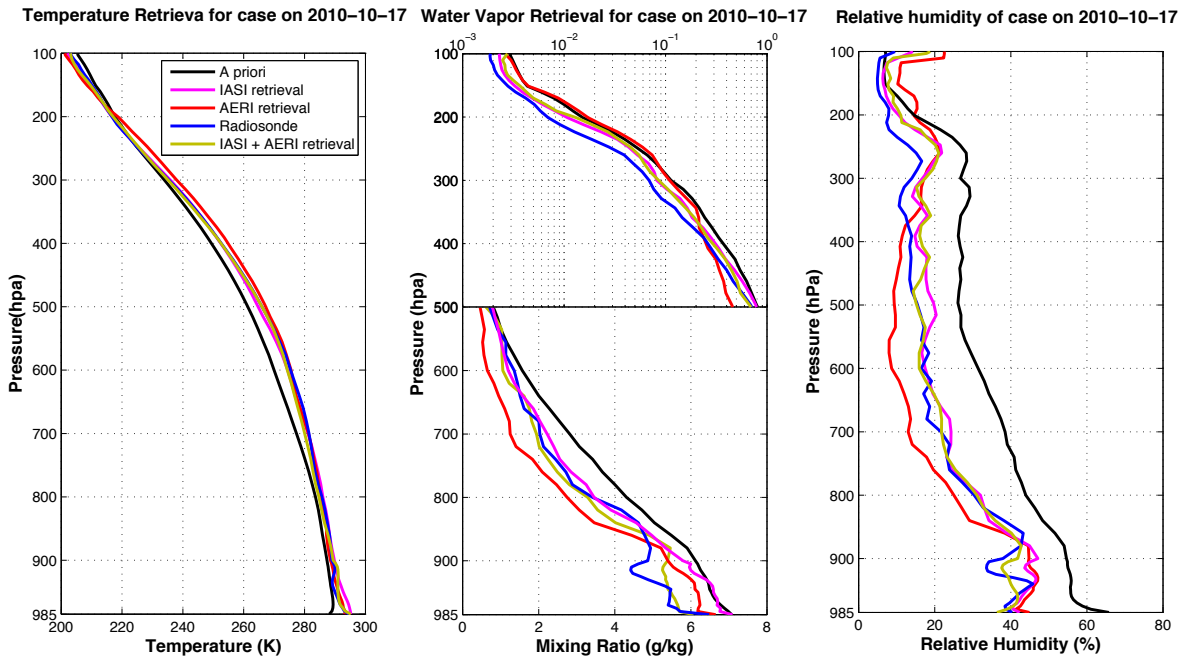

Figure 5.13 Retrieval profiles of the case on 2010-10-17, 17:25UTC, Lamont, OK. Black lines are the a-priori (statistical mean for 3-year radiosondes; Blue lines are the radiosonde profiles; Purple lines are the retrieval from IASI measurement; Red lines are the retrieval from ground AERI measurement; Dark yellow lines are the retrieval from IASI and AERI measurement combination.

The plot of water vapor mixing ratio shows that near the surface both the combined retrieval and the AERI retrieval match the radiosonde, then discreteness between these two retrievals and radiosonde increases as altitude increases. Meanwhile the IASI retrieval just follows the *a-priori*. All three retrievals do not catch the remarkable perturbation below 900 hPa, although from the aspect of relative humidity, the difference between retrievals and radiosonde are less than ten percent. Above 850 hPa, the combined retrieval and the IASI retrieval match the profile of radiosonde up to 400 hPa above which there is no significant perturbation on radiosonde pro-

file. The AERI retrieval is systematically lower than the other retrievals and the radiosonde in this region with an ∼10 percent difference of relative humidity. From 400 hPa, the AERI retrieval follows the *a-priori*, while the IASI retrieval and the combined retrieval follow the the radiosonde and then approach the *a-priori* gradually at higher altitude. These two retrieval maintain a relative humidity difference with the radiosonde that is below 5 percent.

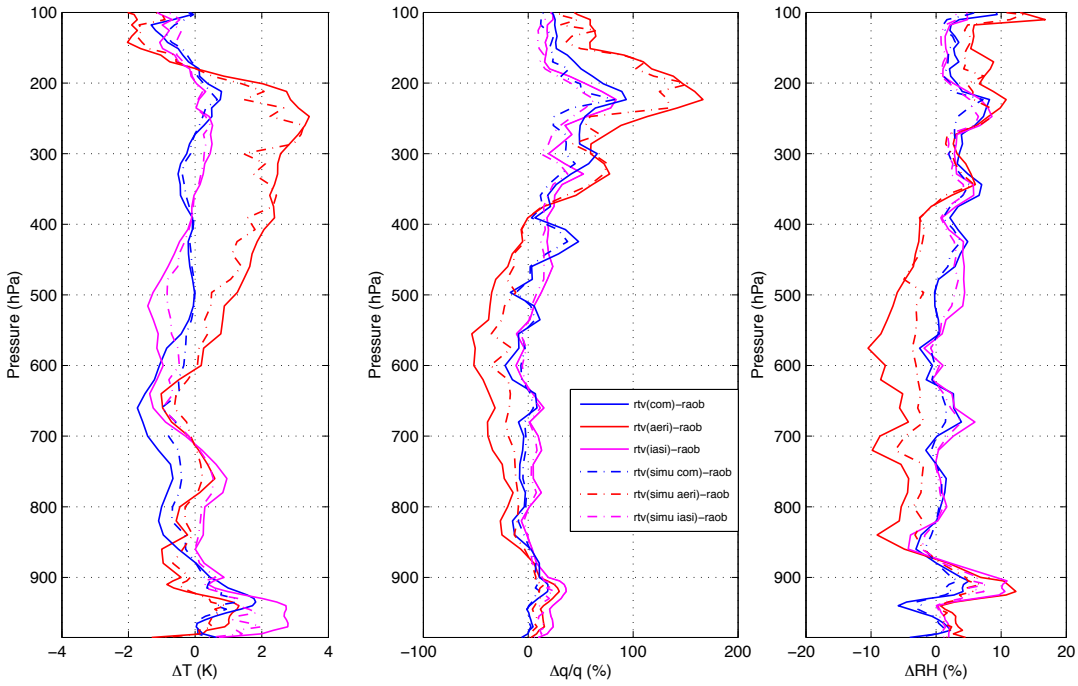

Figure 5.14 Difference between retrieval results and radiosonde of temperature(a), water vapor (b), and relative humidity (c). In (b) the relative difference for water vapor (($q_{retrieval}$-q_{raob})/q_{raob}) on 2010-10-17. Blue lines are the difference between combined retrieval and radiosonde; Purple lines are the difference between upwelling retrieval and radiosonde; Red lines are the difference between downwelling retrieval and radiosonde. Solid lines are the retrieval from real measurements, and dot-dashed lines are the retrieval from simulated radiance of radiosonde.

The detailed difference between retrievals and radiosonde for this case is shown in figure(5.14). The main different between this case with the other two cases discussed previously is that the strong temperature and water vapor features are both within

boundary layer, while within the higher troposhere the temperature and water vapor decrease gradually. The combined retrieval of temperature maintains a residual below 1 K throughout whole troposphere except at silent region we pointed at 860 hPa and 660 hPa. The downwelling retrieval possesses an equivalent, or better result than the combined retrieval below 500 hPa. Above 500 hPa, the residual of downwelling retrieval increases gradually and reaches peak of 3 K at 260 hPa. The performance of the upwelling retrieval is like that of the combined retrieval in most of the troposphere, except within the boundary layer where the residual of the upwelling retrieval is greater than 2 K. The improvement of all three retrievals using simulated radiance rather than real radiance are very obvious in the lower troposphere.

Since there is no significant perturbation within the upper troposphere for the water vapor profile of radiosonde, the residual of the upwelling retrieval and the combined retrieval for water vapor increases much more smoothly than for the Hampton and Nevada cases, and reach a the maximum of 60% at 330 hPa. On the other hand, within middle and upper troposphere, the residual of the downwelling retrieval for water vapor is oscillating sinusoidally from -50 % to 150%. Within the boundary layer, all three retrievals cannot capture that strong water vapor drop in at 920 hPa. The upwelling retrieval as usual executes worse than the other two retrievals within the boundary layer, and the residual reaches to 30% at the level of the abrupt drop in humidity. Both the performance of the downwelling retrieval and the performance of the combined retrieval are quite good except for the depletion structure. Considering the intensity of this depletion, the downwelling and the combined retrieval perform quite better than the downwelling retrieval and the combined retrieval perform for the depletion region in upper troposphere shown in the previous tow cases.

The comparison of spectra for this case is shown in figure(5.15). The plot(a) and (b) of this figure indicate that within the water vapor region (540-600 cm^{-1}, 1100-1300 cm^{-1}) and the part of CO_2 region (700-740 cm^{-1}) which represents the temperature

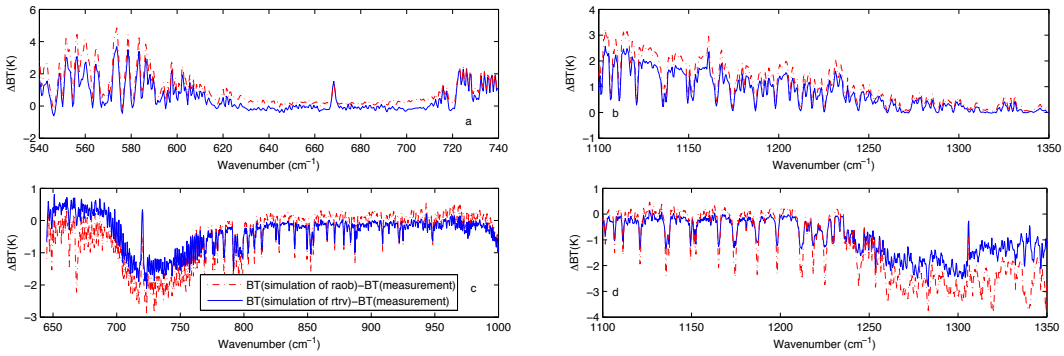

Figure 5.15 Brightness temperature spectra comparison of measurement and simulation. Plot (a) and (b) show the difference between AERI measurement and simulation from radiosonde / retrieval profiles within 540 - 720 cm^{-1}, 1100 - 1350 cm^{-1}. Plot (c) and (d) show the difference between IASI measurement and simulation from radiosonde / retrieval profiles within 645 - 1000 cm^{-1}, 1100 - 1350 cm^{-1}.

near top of boundary layer, the residual of downwelling spectra is twice than residual of the previous two cases. The Plot(c) and (d) show that the magnitude of residual for upwelling radiance is about 2K, also the improvement of retrieval for radiance simulation is quite significant.

5.2.4 AEROSE2008

May 17th 2008

On the May 17, 2000, the Metop overpassed the NOAA Ship *Ronald H. Brown* location at 00:57UTC, while the radiosonde was launched at 00:37UTC. The distance between the NOAA Ship *Ronald H. Brown* and the nearest footprint is about 21km. Thus, it can be assumed that the atmospheric state represented by radiosonde is the same as the state represented by the IASI radiance measurement. The AVHRR channel 4 image for the region of balloon launch site in shown in figure(5.16). For this case, the visible image for the night time is absent. The brightness temperature

at the vessel location is about 280 K, more than 10 degree lower than the surface temperature, thus there may be some single low clouds around the vicinity of vessel.

Figure (5.17) shows the temperature and water vapor profiles on 00:37UTC, May 17th, 2008. The temperature profile of radiosonde indicates that there was a isothermal layer within 900hPa-700hPa. Below 900hPa, the lapse rate of radiosonde is same as mean profile of tropical region except the 2K gap. Unfortunately, the retrieval procedure being used cannot deal with the cloudy scenario. Assuming that the vertical structure variation is small, the spatial and temporal variance can be ignored except cloud layer. The IASI spectrum of the footprint southeast of balloon launching site where the brightness temperature of AVHRR channel 4 is 290 K, was selected for the retrieval, although the distance between balloon launching site and the clear footprint selected for retrieval is about 200 km away. Also the M-AERI spectrum at 01:00UTC which is clearer than the spectrum at exact balloon launching time was selected for the ground retrieval.

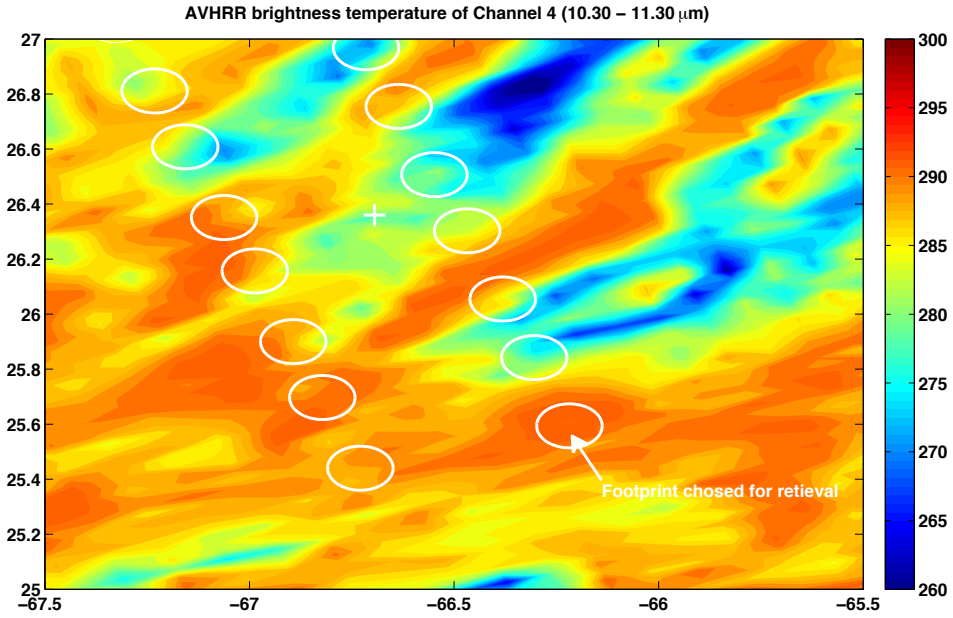

Figure 5.16 AVHRR channel 4 image of the case on 2008-05-17. Circles indicate the IASI footprint, cross indicates location of balloon launches

The retrieval results are shown in the figure (5.17) along with the radiosonde profiles. Between 200 hPa and 550 hPa, the temperature profile retrieved from IASI spectrum matches the radiosonde very well. Below 550 hPa, there is a significant temperature difference between IASI retrieval and radiosonde, especially within the 700 hPa and 900 hPa layer, the IASI retrieval profile has almost same lapse rate as radiosonde but with 2-3 K difference. Meanwhile, the temperature retrieval from M-AERI spectrum matches the radiosonde very well below the 700 hPa. Above 700 hPa, the M-AERI retrieval profile follows the mean GFS temperature profile used as the *a-priori*. As expected, the temperature profile retrieved from the combined IASI and M-AERI radiance spectra matches the radiosonde much better than the other retrievals throughout the entire troposphere.

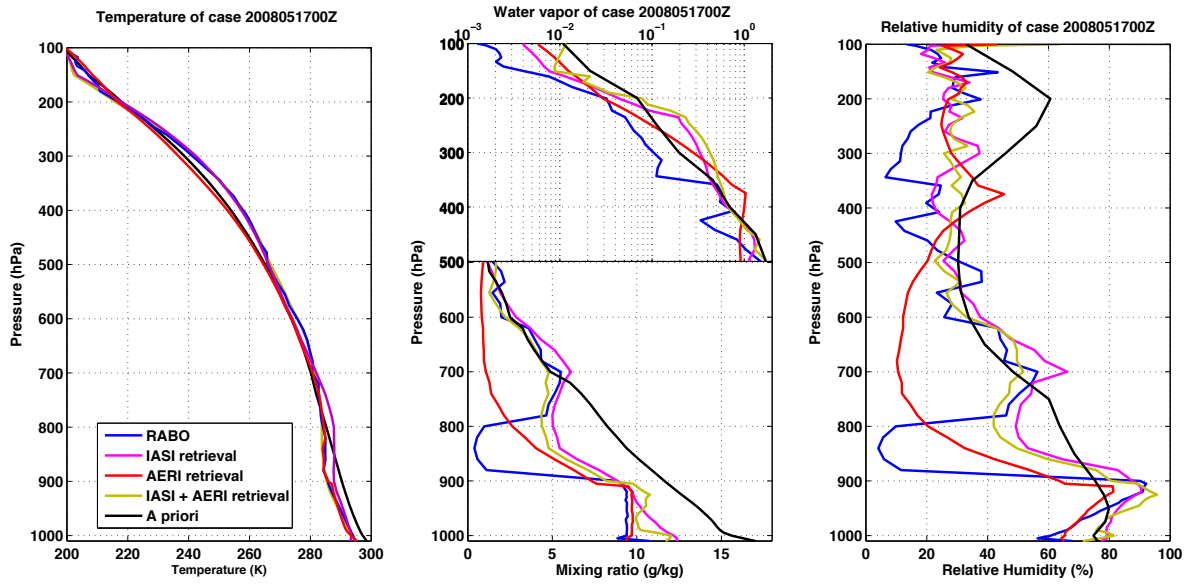

Figure 5.17 Retrieval profiles of the case on 2009-05-17, 00:57UTC, Atlantic. Black lines are the *a-priori* (statistical mean for GFS profiles; Blue lines are the radiosonde profiles; Purple lines are the retrieval from IASI measurement; Red lines are the retrieval from ground AERI measurement; Dark yellow lines are the retrieval from IASI and AERI measurement combination.

The middle plot of the figure (5.17) shows the water vapor mixing ratio profiles from the radiosonde and the retrievals. For the water vapor radiosonde profile, a very large humidity drop exists above 900 hPa. Below that level, the mixing ratio

value maintains a constant about 9.5 g/kg; Between 900 hPa and 800 hPa, the mixing ratio decreases about 0.5 g/kg, this dramatic drop may due to the error of radiosonde. Between the 800 hPa and 600 hPa, there is a wet layer where the value of mixing ratio reaches 6 g/kg. Above 600 hPa, the mixing ratio decreases with altitude exponentially. The water vapor profile retrieved from IASI spectrum resolve the wet layer structure of the radiosonde profile between 800 hPa and 600 hPa but does not resolve the very dry layer below nor the inversion near the surface. The profile retrieved from M-AERI match the the inversion structure below 900 hPa quite well except for a magnitude difference. But above 900 hPa, the water vapor decreases exponentially with altitude and does not reflect the dry layer within 900 hPa and 800 hPa nor the wet layer within 800 hPa and 600 hPa. Below 900 hPa, unlike either the constant structure of the profile retrieved from the M-AERI spectrum or exponentially decreasing structure of the profile retrieved from the IASI spectrum, the water vapor mixing ratio profile retrieved from the combined IASI and M-AERI radiance spectra is oscillating around 11 g/kg. This oscillation may be caused by the numerical instability. In any case, the combined retrieval resolves the surface structure shown by the radiosondes. Above 900 hPa, the profile of the combined retrieval has a shape similar to the IASI profile retrieval.

The retrieval comparison figure(5.18) show that the error of the combined retrieval for temperature is quite is less than 1 K throughout most troposphere except the cloud layer and region near tropopause. Above cloud layer,the downwelling retrieval is much lower than the radiosonde, and the maxima of residual reaches 6 K. On the contrary, below the cloud layer, the upperwelling retrieval is much higher than the radisosonde, and the maxima of residual reaches 4 K. Nevertheless, both the downwelling and upwelling retrieval from the radiances simulated from the radiosonde reduces the retrieval residual remarkably, the maxima residual for these two retrievals being about 2 K.

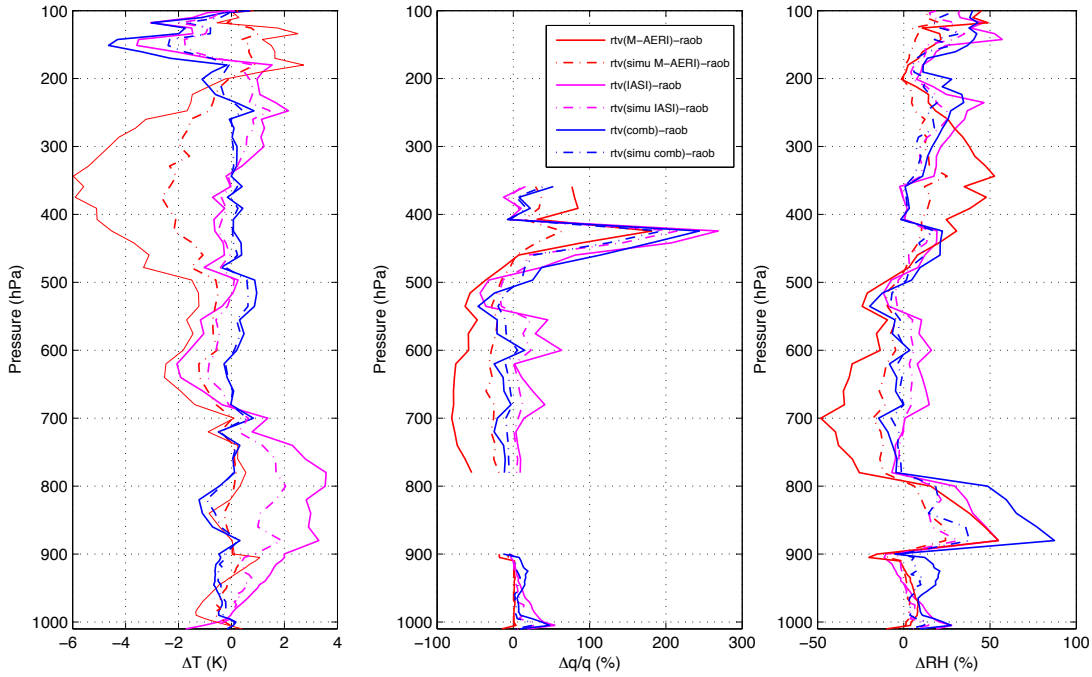

Figure 5.18 Difference between retrieval results and radiosonde of temperature(a), water vapor (b), and relative humidity (c). In (b) the relative difference for water vapor (($q_{retrieval}$-q_{raob})/q_{raob}) on 2008-05-17. Blue lines are the difference between combined retrieval and radiosonde; Purple lines are the difference between upwelling retrieval and radiosonde; Red lines are the difference between downwelling retrieval and radiosonde. Solid lines are the retrieval from real measurements, and dot-dashed lines are the retrieval from simulated radiance of radiosonde.

The residual of water vapor retrievals are shown in middle plot of this figure. Since the radiosonde of water vapor is too low in the section between 900 hPa and 800 hPa, and the section above 350 hPa, the residual in these two layers are not displayed. Both the upwelling retrieval and combined retrieval perform very well below 350 hPa except at 420 hPa where radiosonde water vapor drops sharply. Meanwhile the downwelling retrieval make the much drier result above the boundary layer, and the residual is about 60 % dryer than the radiosonde.

The spectra residual in figure(5.19) shows that the error caused by the radiosonde make the residual of downwelling radiance increase to a value about 10 K for the

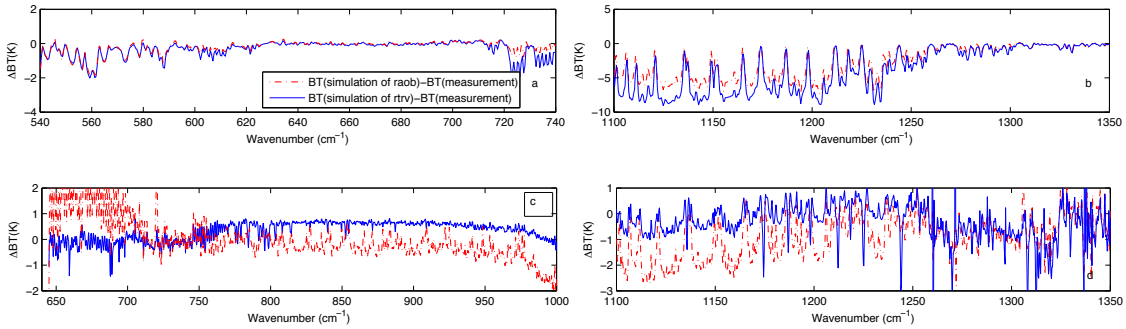

Figure 5.19 Brightness temperature spectra comparison of measurement and simulation. Plot (a) and (b) show the difference between M-AERI measurement and simulation from radiosonde / retrieval profiles within 540 - 720 cm^{-1}, 1100 - 1350 cm^{-1}. Plot (c) and (d) show the difference between IASI measurement and simulation from radiosonde / retrieval profiles within 645 - 1000 cm^{-1}, 1100 - 1350 cm^{-1}.

water vapor region. The residual of upwelling radiance are affected by the error of radiosonde and the 200-km mismatch of the IASI measurement. These two factors increase the residual to a value of 3 K.

Unlike previous clear cases, both the radiosonde profile of water vapor and the AVHRR infrared image for this case indicate that there was a thick cloud at the lower troposphere during the overpass of the Metop spacecraft and at the time of the balloon launches. Even in this extreme case, the water vapor retrieval from combined clear IASI and M-AERI spectra resolve get the structure characteristics below and above cloud while the retrieval from the upwelling or the downwelling radiance spectrum alone cannot resolve these profile characteristics. The cloud effects the temperature retrieval much less than it effects the water vapor retrieval.

5.3 Discussion

5.3.1 General

In the previous section, individual example cases for the four observation sites were presented. All four cases demonstrate same characteristic of the retrieval from simulated radiance we discussed in the first section of this chapter: The improvement of the combined retrieval over the other two retrieval methods is obvious. Errors for the temperature retrieval are much smaller than errors for the water vapor retrieval. Within the boundary layer, all three retrieval methods achieve better result than in the higher atmosphere.

All four cases indicate that once strong perturbations of the radiosonde profile of temperature or water vapor occur, the residual of all retrievals would increase substantially in those regions even for the simulation retrievals where the errors of measurement and the errors of the radiative transfer model are excluded. But it is noted that the intensity of the retrieval deterioration in those region would vary from one case to another. For the downwelling retrieval and the combined retrieval within the boundary layer (surface to 800 hPa for the Nevada case, surface to 900 hPa for the others), the deterioration was much milder than the other situations. The table(3.1) and table(3.5) in chapter three has stated that the pressure interval of the downwelling fast forward model is 5 hPa for the section of 1000-900 hPa, and 20 hPa for the middle troposphere. For the Nevada case, if the real pressure level is normalized to 1000 hPa, the interval for section of surface to 800 hPa is around 5 hPa. Meanwhile the pressure interval of upwelling fast forward model is about 20-25 hPa for lower and middle troposphere. The denser pressure interval for the downwelling model in boundary layer would make the shape of the weighting function of downwelling radiance in that region more narrow than the shape of the weighting function for other scenarios. The narrower of the weighting function the more representative is the retrieval at

the pressure where weighting function peaks. Thus, finer scale weighting functions makes the downwelling retrieval and the combined retrieval within the boundary layer capture the structure better than the satellite-only retrievals.

5.3.2 Statistics

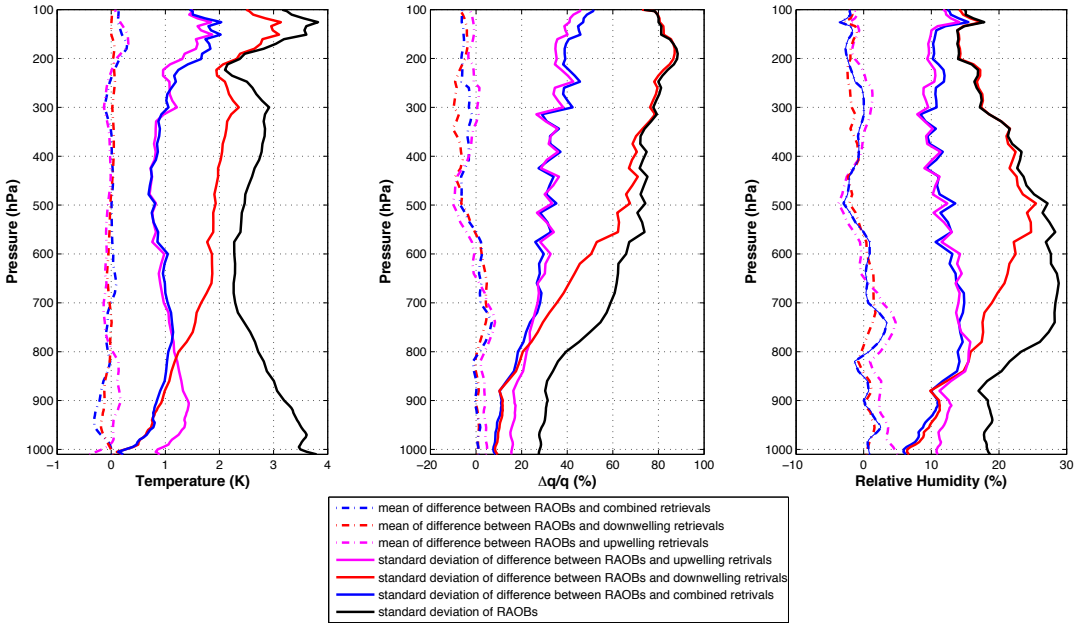

Figure 5.20 Brightness difference between simulated radiance from retrieval result and from radiosonde, Upper panel for upwelling radiance simulation, lower panel for downwelling radiance simulation, respectively.

In this section we will discuss the statistics of the all 90 retrieval cases. The statistical features of the errors associated with the simulation retrievals are shown in the figure (5.20). For the temperature retrieval, the mean difference between retrieval and radiosonde are no more than 0.3 K. Below 800 hpa, and the mean difference between combined retrievals and radiosondes has a shape similar to the mean difference between the downwelling retrievals and the radiosondes. The standard deviations for the combined retrieval and the downwelling retrieval are close to zero near ground, then increase slowly with the altitude and reach 1 K at 800 hPa. The standard deviation of the upwelling retrieval is near 1 K, then reaches the maxima of 1.3 K at 900

hPa, and turns back to 1 K at 800 hPa. From 800 hpa to 400 hpa, the mean difference between the results of all three retrievals and the radiosondes are very close to each other. Above 400 hPa, the mean difference between the combined retrieval and the radiosondes remains the shape of the mean difference between upwelling retrieval and radiosondes, which is oscillating about zero with magnitude of 0.3 K. Also, the standard deviation of combined retrieval has a shape almost identical to the standard deviation of upwelling retrieval and maintains a value less than 1 K from 800 hPa to 250 hPa. Above 250 hPa, both standard deviation of the combined retrievals and standard deviation of radiosondes increase to 2 K at tropopause, where the two profiles diverge slightly. This is caused by the sharp tropopause structure. Meanwhile, blow 800 hPa, the mean difference between the downwelling retrievals and the radiosondes is near zero. The standard deviation of the downwelling retrieval increases gradually up to an altitude of 230 hPa; above that level, the standard deviation jumps to 3 K. Comparing this profile with the upper portion of profile of the standard deviation of radiosondes, it can be seen that these two profiles have the same structure but are slightly different in magnitude. This phenomenon can be explained by the fact that the downwelling radiance is insensitive to the structure of upper atmosphere, so the downwelling retrieval structure is highly dependent on the mean profiles of the statistical ensemble to used to define the vertical structure of the retrieval.

The statistics of the water vapor retrieval which is shown in the right two plots in figure (5.20) display results similar to the temperature retrieval. Below 800 hPa, both mean difference between the downwelling retrievals and the radiosondes and the mean difference between the combined retrievals and the radiosondes are near zero, whereas the mean of the relative difference between the upwelling retrieval and the radiosonde is a systematic 5%. Near the ground, the standard deviation of difference between the downwelling retrievals and the radiosondes and the standard deviation of difference between the combined retrievals and the radiosondes are half of value of

standard deviation of difference between the upwelling retrievals and the radiosondes. All three standard deviation increase gradually and converge at 800 hPa with value of about 20%. Above that pressure level, the three mean differences oscillate about zero with a magnitude of 10%. As the altitude increase, the magnitude of oscillation for the profile of downwelling retrieval is significantly higher than for the other two profiles. Like the temperature, above the 800 hPa the standard deviation of combined retrievals coincides with the standard deviation of upwelling retrievals up to 300 hPa, above where the standard deviation of combined retrievals increases slightly faster than does the standard deviation of upwelling retrievals. Meanwhile, the standard deviation of the downwelling retrievals increases at twice the rate of the other two standard deviations, and meets the standard deviation of radiosondes at about 350 hPa. Thus, the water vapor retrievals below 300 hPa are more reliable than the retrieval above 300 hPa.

Figure(5.21) provides the means and standard deviations of the difference between radiosondes and corresponding retrievals from real measurements of all 90 cases. Compared with the figure(5.20) which shows the statistics of the retrieval from the simulated radiance, the standard deviation which can be considered as retrieval errors profiles of residual of the retrieval results from real radiance measurement have similar structure of the profiles in figure(5.20) but with higher magnitude, while the mean profiles are more different with the mean profiles in figure(5.20). Unlike the retrieval from simulated radiance which biases can be ignored (biases are lower than 0.3 K for temperature, biases are lowere than 10 % for water vapor). Biases of the retrieval from real radiance spectra reaches 1 K and 20% for temperature and water vapor respectively, especially the upwelling retrieval within boundary layer where the bias reaches to 1.5 K.

Like temperature retrieval errors for simulated radiance, the temperature errors of retrieval from real upwelling radiance reaches a maxima of 3 K within boundary,

then keeps a constant of 2.5 K from 900 hPa to 700 hPa. Above 700 hPa, the error decreases gradually and keep a minima of 1.5 K from 600 hPa to 250 hPa. Near the tropopause, the error increase dramatically. Meanwhile, the error of retrieval from real downwelling radiance increases from 0.3 K to 1.5 K sharply below 980 hPa, then increases gradually to 3.3 K at 800 hPa. Above 800 hPa, this error profile has almost same shape of the error profile of retrieval from simulated radiance, oscillating between 2-4 K smoothly. The error of retrieval from combined real radiance increases from 0.3 K at surface to 2.5 K at 700 hPa. Above 700 hPa, this error profile is following the error profile of upwelling retrieval.

For the water vapor retrieval, comparing the error profiles of retrieval from simulated radiance, except the values of error are larger, the profiles are oscillating much more roughly. Within the boundary layer, the error of upwelling retrieval keeps a constant of 50%. Above 800 hPa, this error profile is oscillating between 50% and 80% until the tropopause. The magnitude of this error profile iin this section is generally 20-30 percentage-points higher than the error profile of upwelling retrieval from simulated radiance. Also, this error profile has a tiny increasing trend. Near the surface, the error of downwelling retrieval is about 20%, then the error is increasing to 100% at 200 hPa steadily with zigzag structure. It should be noticeable that above 500 hPa, this error has almost same magnitude of retrieval error from simulated radiance. Below the 800 hPa, the error profile of combined retrieval has same shape of error profile of error profile of downwelling retrieval with the minima of 20%. Above the 800 hPa, this error profile transfers the to the shape of the error profile of upwelling retrieval.

The sources of retrieval errors include the error due to retrieval procedure, the error due to numerical fast forward model, the error due to the temporal and spacial mismatch between the radiosondes and satellite measurement, and even the error from radiosonde itself.

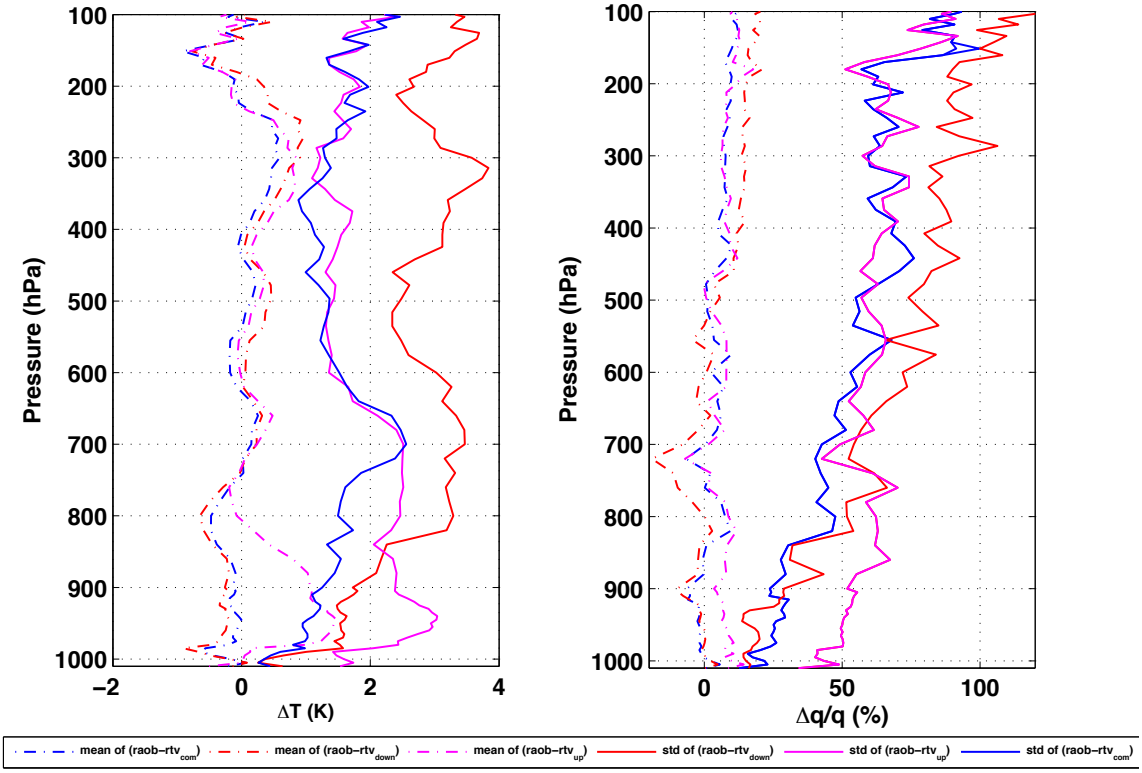

Figure 5.21 Statistics for total retrieval, left plot shows the mean and standard deviation of the difference between radiosonde and retrieval for temperature, right plot shows the mean and standard deviation of the relative difference between radiosonde and retrieval for water vapor

Assuming the error due to the retrieval procedure referred as the procedure error is independent on the other errors, we can get the other errors referred as the rest error by minus the residual standard deviation of retrievals from simulated radiance spectra from the residual standard deviation of retrievals from real measurements as following:

$$\begin{aligned} \sigma_{total}^2 &= \sigma_{retrieval}^2 + \sigma_{rest}^2, \\ \sigma_{rest} &= \sqrt{\sigma_{total}^2 - \sigma_{retrieval}^2} \end{aligned} \tag{5.3.1}$$

Figure(5.22) shows the profile of σ_{rest} of temperature and water vapor retrieval respectively. For the downwelling retrieval, below the 900 hPa, the rest error are lower than 0.8 K and 15% for temperature and water vapor respectively. From 900

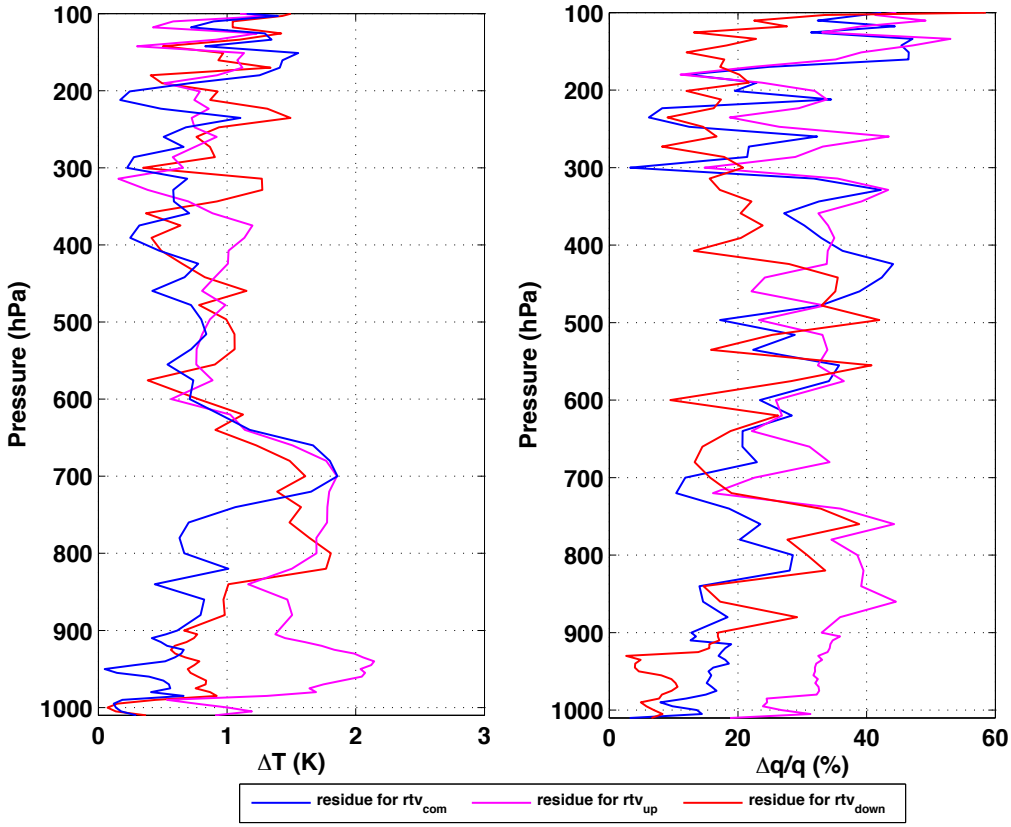

Figure 5.22 Standard deviation for the difference between radiosonde and retrieval due to the errors excluding the error of retrieval procedure.

hPa to 400 hPa, the magnitude of the rest error of downwelling retrieval increase to 1 - 2 K for temperature and 20 - 40% for water vapor. Above 400 hPa until tropopause, the magnitude of the rest of downwelling retrieval decrease to 1 K and 20%. For the retrieval from downwelling radiance measurement, there is no mismatch error, i.e., the radiosonde and downwelling radiance measurement represent the exact identical atmospheric status. The profiles of rest errors for downwelling retrieval indicate that near the surface, the rest error can be ignored while within the mid troposphere the rest errors would contribute a large part of total errors. As we know that the weighting functions of downwelling radiance near the surface have more two orders of magnitude than those of upper atmosphere, that means retrieval for lower levels is

very sensitive to the input radiance spectra, so even the only minor error of radiative transfer model may cause a significant error on the retrieval. On the other hand, the peak of most weighting functions of downwelling radiance are concentrated near the surface, this would overcome the error sensitivity of weighting function near surface. As the altitude increases, the weighting function of downwelling radiance decrease dramatically, the retrieval would not be sensitive to the difference between measured spectra and simulated spectra. So for the retrievals from downwelling radiance within upper troposphere, errors between radiosonde and retrieval results mostly due to the error of retrieval procedure itself. These would explain that at the lower levels the retrieval from simulated radiance are obviously better than the retrieval from real radiance measurement, while at higher levels these two types of retrieval got very close results.

For the upwelling retrieval, below 600 hPa, the rest errors for temperature is keeping $\sim$ 2K; above 600 hPa, this profile is oscillating between 0.5 - 1 K. Meanwhile the profile of water vapor rest error is is oscillating between 20% and 40% for the most of troposphere. The shape of the these profiles indicate that the contribution of the other error sources is homogenous for water vapor retrieval. This homogeneousness may due to the homogenous vertical distribution of peak of weighting function. while the contribution of the other error sources is more obvious for lower atmosphere where temperature is more sensitive to the variation of earth surface. Thus, the mismatch contribute more to total errors for temperature retrieval of lower atmosphere. As for the combined retrieval, the rest error distributes like the rest error of downwelling retrieval does below 600 hPa, and distributes like the rest error of upwelling retrieval does above 600 hPa.